Terahertz and Infrared Spectroscopy on Low-Dimensional Quantum Magnets

Dissertation

zur Erlangung des Grades eines
Doktors der Naturwissenschaften
(Dr. rer. nat.)

eingereicht an der
Mathematisch-Naturwissenschaftlich-Technischen Fakultät
der Universität Augsburg

von

Zhe Wang
aus Shandong, China

Augsburg, Februar 2015

Universität
Augsburg
University

Gutachter:	Prof. Dr. Alois Loidl Prof. Dr. Christine Kuntscher Prof. Dr. Peter Armitage
Tag der Prüfung:	15. Juli 2015

Contents

1 Introduction

Quantum magnets are magnetic materials where quantum fluctuations are important and should be considered as well as thermal fluctuations. Quantum effects are enhanced especially for the systems with low dimensionality, small spin, and strong frustrations. The focus of this dissertation is on low-dimensional quantum magnets with spin-1/2 and spin-1. The low-dimensional quantum magnets provide unique possibilities to study ground and exited states of quantum models, to explore new phases of matter, and to investigate the interplay of quantum and thermal fluctuations.

The field of low-dimensional magnetism dates back to the pioneering theoretical works by Wilhelm Lenz and Ernst Ising in 1920s, while real materials, in which the low-dimensional theoretical models were realized, were synthesized only around 1970. This field rapidly developed since then, especially after the discovery of high temperature cuprate superconductors in the mid-eighties, where superconductivity and magnetic fluctuations are intimately connected. The magnetic fluctuations in low dimension play an important role also in the recent discovered Fe-based superconductors. Today the field of low-dimensional magnetism has become one of the most active areas in condensed matter physics.

Despite the vast varieties existing in this field, the studies presented in this dissertation will concentrate on the following typical spin-dimer and spin-chain systems:

- **Spin-dimer systems**: The isostructural antiferromagnetic insulators $Sr_3Cr_2O_8$ and $Ba_3Cr_2O_8$ are spin-dimer systems based on the unusual Cr^{5+} ions with spin-1/2. The exchange interactions between Cr ions are geometrically frustrated at room temperature since the Cr ions form a bilayer hexagonal lattice. The frustration is lifted after a Jahn-Teller type structural phase transition into a monoclinic phase. Well below the structural transition, the intra-bilayer exchange interaction turns to be dominant and a weakly-coupled spin-dimer structure is established. Bose-Einstein condensation of magnons, the elementary magnetic excitations of the spin dimers, can be driven by applying magnetic fields at low temperature. The magnon condensation in $Sr_3Cr_2O_8$ bears the highest temperature record of 8 K in the reported spin-dimer systems.
  The Cu^{2+}-based antiferromagnetic spin-dimer system $CuTe_2O_5$ exhibits complex exchange paths between the Cu ions, which is a common interesting property of transitional metal oxides, especially with the presence of lone-pair Te^{4+} ions. The dominant exchange path is not that between the nearest-neighbor Cu ions

but rather an exchange path mediated via the Te ions.

- **Spin-chain systems**: The isostructural insulators $SrNi_2V_2O_8$ and $SrCo_2V_2O_8$ belong to two distinct categories of one-dimensional antiferromagnetic systems. Ni^{2+} ($3d^8$, $S = 1$) and Co^{2+} ($3d^7$, $S = 3/2$) are the only magnetic ions that form spin chains in the corresponding systems. At low temperature, $SrNi_2V_2O_8$ is in the Haldane phase that has a spin-singlet ground state and a gapped spin-triplet excited state, as expected for the Heisenberg spin-1 antiferromagnetic chain systems. Due to the single-ion anisotropy of Ni spins, $SrNi_2V_2O_8$ lies very close to the phase boundary between the Haldane phase and an Ising antiferromagnetic phase. Quantum phase transition to the Ising phase could be induced by applying magnetic field, when the Haldane gap is closed due to the Zeeman interaction. In contrast, $SrCo_2V_2O_8$ is a realization of pseudospin-1/2 Ising-like antiferromagnetic chain system. The elementary excitations above the ground state of $SrCo_2V_2O_8$ are gapped spinon-pair excitations. $SrCo_2V_2O_8$ can enter a gapless phase in an applied external magnetic field. The Ising-like exchange anisotropy of Co spins is induced by cooperative effects of spin-orbit coupling and crystal-field splitting. The exchange interactions are between the lower-lying spin-orbit Kramers doublets of Co ions that have a total angular momentum (pseudospin) of 1/2. Weak inter-chain couplings stabilize long-range antiferromagnetic order at low temperatures and play the role of a confinement potential for spinon-pair (domain-wall) excitations.

Studies of the magnetic, orbital, and phononic excitations by terahertz and infrared spectroscopy provide important information on the structural phase transition, quantum phase transition, magnetic exchange interaction and anisotropy in these low-dimensional quantum magnetic systems. The outline of this dissertation is following: Chapter 2 introduces the theoretical basis of the quantum spin-1/2 dimer antiferromagnetic systems and the antiferromagnetic spin-chain systems with spin-1/2 and spin-1. In the first part, basic models for describing specific heat, magnetic susceptibility, magnetic excitations and anisotropy will be introduced for the spin-dimer systems. The concepts of Bose-Einstein condensation of magnons and the Jahn-Teller effect are also briefly illustrated. The second part focuses on the low-temperature phase diagram and magnetic field induced quantum phase transitions of various one-dimensional quantum spin models. Spinon excitations and spinon confinement are particularly discussed. The experimental techniques, terahertz and infrared spectroscopy, are introduced in Chapter 3. Chapter 4 – Chapter 6 constitute the main body of experimental results and findings. Investigations on spin singlet-triplet excitations in the spin-dimer systems $CuTe_2O_5$, $Sr_3Cr_2O_8$, and $Ba_3Cr_2O_8$ are presented in Chapter 4. Exchange interactions and magnetic anisotropy parameters are determined by analyzing the observed features of magnetic excitations with microscopic models.

Orbital physics is the main topic in Chapter 5. Orbital fluctuations in $Sr_3Cr_2O_8$ while orbital ordering in $Ba_3Cr_2O_8$ are revealed by different temperature dependencies of magnetic and phononic excitations. Chapter 6 presents exotic magnetic excitations in the spin-chain systems $SrNi_2V_2O_8$ and $SrCo_2V_2O_8$ at low temperatures with and without magnetic fields. Magnetic excitations have been followed up to high fields of 30 T. The experimental results are summarized and perspectives are given in Chapter 7.

2 Introduction to Low-Dimensional Quantum Magnetism

2.1 Spin-1/2 dimer

Spin dimer systems can be realized in spin-1/2 Heisenberg antiferromagnets when the exchange interaction $J_0 > 0$ between two magnetic ions within a dimer is much larger than inter-dimer interactions, which can be described by

$$\hat{H} = \sum_i J_0 \mathbf{S}_{i1} \cdot \mathbf{S}_{i2} + \sum_{ijmn} J_{ijmn} \mathbf{S}_{im} \cdot \mathbf{S}_{jn} + g\mu_B H \sum_{im} S^z_{im} \tag{2.1}$$

with the intra-dimer interaction J_0 much larger than the inter-dimer interactions J_{mnij}, where i, j refer to different dimers and $m, n = 1, 2$ to their respective magnetic ions. The last term takes into account the Zeeman interaction in an external magnetic field H along z direction, where g is the effective g-factor and μ_B is the Bohr magneton.

2.1.1 Spin-singlet and spin-triplet states

For isolated spin-$\frac{1}{2}$ dimers, i.e., without inter-dimer interaction, in the presence of magnetic field, the effective spin Hamiltonian can be written as the sum of intra-dimer exchange interaction and Zeeman energy

$$\hat{H} = \hat{H}_{ex} + \hat{H}_{Zeeman} = J_0 \mathbf{S}_1 \cdot \mathbf{S}_2 + g\mu_B \mathbf{H} \cdot (\mathbf{S}_1 + \mathbf{S}_2), \tag{2.2}$$

where J_0 is the exchange-interaction constant between the spins $\mathbf{S}_1$ and $\mathbf{S}_2$. Since $\hat{H}_{ex}$ and $\hat{H}_{Zeeman}$ do not commute, Eq. (2.2) cannot be solved straightforward. If the magnetic field is set along $+z$ direction, the Hamiltonian can be written using $\mathbf{S}^2$, the square of the dimer spin-operator $\mathbf{S} = \mathbf{S}_1 + \mathbf{S}_2$, and its z-component S_z, which are commutative. The common eigenstates of $\mathbf{S}^2$ and S_z are the spin-singlet state

$$|S_0\rangle \equiv |0, 0\rangle = \frac{1}{\sqrt{2}}(|\uparrow\downarrow\rangle - |\downarrow\uparrow\rangle),$$

and the spin-triplet states

$$\begin{aligned} |T_1\rangle \equiv |1,1\rangle &= |\uparrow\uparrow\rangle, \\ |T_0\rangle \equiv |1,0\rangle &= \frac{1}{\sqrt{2}}(|\uparrow\downarrow\rangle + |\downarrow\uparrow\rangle), \\ |T_{-1}\rangle \equiv |1,-1\rangle &= |\downarrow\downarrow\rangle, \end{aligned}$$

where $|\uparrow\rangle$ stands for an up-spin, while $|\downarrow\rangle$ stands for a down-spin. The eigenvalue of $\mathbf{S}^2$ is $S(S+1)$ with $S=0$ for the singlet state and $S=1$ for the triplet states. The three-fold degenerated triplet states $|T_1\rangle$, $|T_0\rangle$, and $|T_{-1}\rangle$ are split in an external magnetic field with quantum number $S_z = 1, 0$, and -1, respectively. The good quantum numbers S and S_z are also used to label the eigenstates. In the space of eigenstates, the Hamiltonian in Eq. (2.2) can be written as

$$\begin{aligned} \hat{H}|S,S_z\rangle &= \left[\frac{1}{2}J_0(\mathbf{S}^2 - \mathbf{S}_1^2 - \mathbf{S}_2^2) + g\mu_B H_z S_z\right]|S,S_z\rangle, \\ &= \left[\frac{1}{2}J_0 S(S+1) + g\mu_B H_z S_z - \frac{3}{4}J_0\right]|S,S_z\rangle. \end{aligned}$$

2.1.2 Schottky-type specific heat

For a spin-dimer system, the thermal population of the spin-triplet states increases the entropy of the system that can be detected by specific heat measurements. The corresponding specific heat is given by

$$C_{mag} = \frac{E}{T} \tag{2.3}$$

with the internal energy

$$E = \frac{1}{Z}\sum_{i=1}^{4} g_i E_i e^{-\beta E_i}, \tag{2.4}$$

the partition function

$$Z = \sum_{i=1}^{4} g_i e^{-\beta E_i}, \tag{2.5}$$

and $\beta \equiv 1/k_B T$ with the Boltzmann constant k_B. Energies of the spin-dimer eigenstates E_i are listed in Table 2.1. In a magnetic field the spin degeneracy is lifted, thus the degeneracy factor $g_i = 1$ for $i = 1, 2, 3, 4$.

Without applying an external magnetic field, the higher energy level is triply degenerate and the Schottky-type specific heat is given by

$$C_{mag} = \frac{3\Delta^2}{k_B T^2} \frac{e^{\beta\Delta}}{(3+e^{\beta\Delta})^2} \tag{2.6}$$

$$= 3k_B \left(\frac{\delta T}{T}\right)^2 \frac{e^{\frac{\delta T}{T}}}{\left(3+e^{\frac{\delta T}{T}}\right)^2}, \tag{2.7}$$

where $\Delta = k_B \delta T$ is the spin gap between the single and triplet states. Compared to the non-degenerate two-level system, a factor of three appears as a multiplicative factor and in the nominator of the formula due to the degenerate triplet state. A theoretical specific heat is plotted in Fig. 2.1 as a function of $\delta T/T$ that is the ratio between the spin gap and thermal energy. For a given gap value, a maximum is reached at a corresponding temperature. A decrease or increase of the spin gap will shift the maximum to lower or higher temperature, respectively. In the low or high temperature limit, the Schottky-type specific heat vanishes. An applied magnetic field can reduce the spin gap due to Zeeman interaction, thus the maximum can be shifted to lower temperature and suppressed by increasing the magnetic field. This is observed experimentally and will be shown in Chapter 5.

Table 2.1: Eigenstates, magnetic moments (m_j) and eigenenergies (E_j) of a single spin-1/2 dimer

Eigenstate (j=1,2,3,4)	S_j	$S_{z,j}$	m_j	E_j
$\|0,0\rangle$	0	0	0	$-\frac{3}{4}J_0$
$\|1,+1\rangle$	1	1	$-g\mu_B$	$\frac{1}{4}J_0 + g\mu_B H_z$
$\|1,0\rangle$	1	0	0	$\frac{1}{4}J_0$
$\|1,-1\rangle$	1	-1	$g\mu_B$	$\frac{1}{4}J_0 - g\mu_B H_z$

2.1.3 Magnetic susceptibility

The magnetization of the isolated spin dimer system can be calculated as the ensemble average of magnetic moments in a unit volume according to Table 2.1

$$M = N\frac{\sum_{j=1}^{4} m_j e^{-E_j/k_B T}}{\sum_{j=1}^{4} e^{-E_j/k_B T}},$$

$$= N\frac{g\mu_B(-e^{-g\mu_B H_z/k_B T} + e^{g\mu_B H_z/k_B T})}{e^{J/k_b T} + e^{-g\mu_B H_z/k_B T} + 1 + e^{g\mu_B H_z/k_B T}},$$

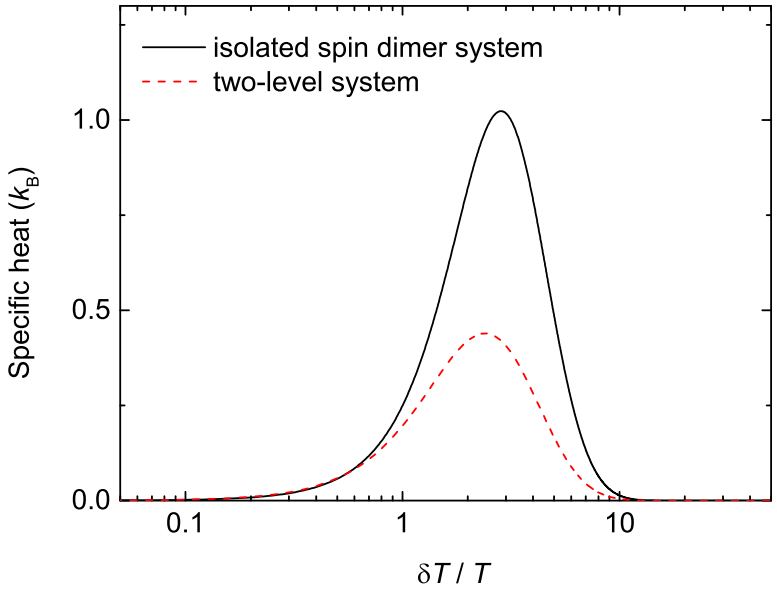

Figure 2.1: Schottky-type specific heat of a non-degenerate two-level system and of an isolated spin-dimer system as a function of the ratio between gap and thermal energy $\delta T/T$.

where N is the number of dimer per volume. In the high temperature (or low field) approximation, i.e. $g\mu_B H_z \ll k_B T$, $e^{\pm g\mu_B H_z/k_B T} \approx 1 \pm g\mu_B H_z/k_B T$, the Bleaney-Bowers spin dimer susceptibility can be obtained [14]

$$\chi_{dimer} = \frac{M}{H_z} = \frac{2Ng^2\mu_B^2}{k_B T}[3 + \exp(J_0/k_B T)]^{-1}. \tag{2.8}$$

In real materials, the dimers are usually not isolated, so the inter-dimer interaction should be considered to renormalize the susceptibility. By treating the inter-dimer interaction as an effective field, the mean field approximation gives [50]

$$\chi_{interacting\ dimer} = \frac{\chi_{dimer}}{1 + \alpha\chi_{dimer}} = \frac{C'}{T}[3 + \exp(J_0/k_B T) + J'/k_B T]^{-1}, \tag{2.9}$$

where $C' = 2Ng^2\mu_B^2/k_B$ is a constant, and $\alpha = J'/k_B C'$ is the molecular-field constant, with J' being the sum of inter-dimer exchange interactions. Also a Van Vleck paramagnetic susceptibility and the possible contribution of impurities should be considered to give the overall susceptibility [7]

$$\chi = \chi_0 + \chi_{imp} + \chi_{interacting\ dimer} = \chi_0 + C_{imp}/(T-\theta) + \frac{C'/T}{3 + e^{J_0/k_B T} + J'/k_B T}. \tag{2.10}$$

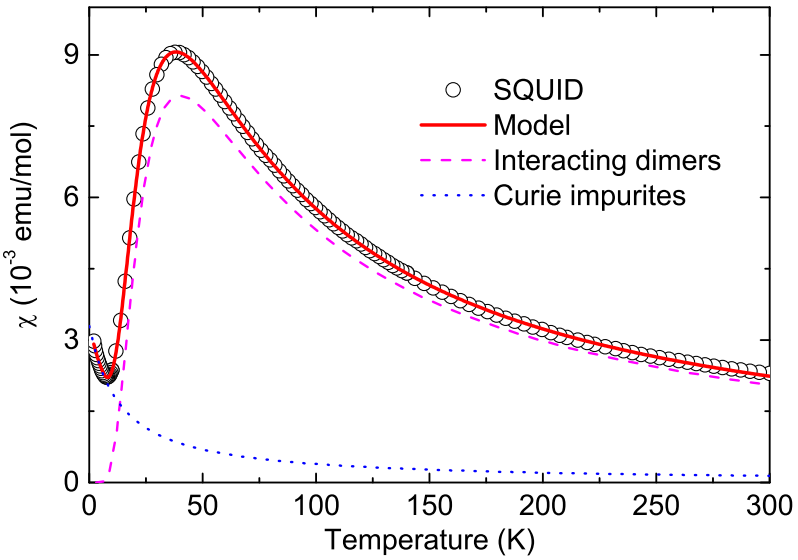

Figure 2.2: The magnetic susceptibility χ versus temperature for $Sr_3Cr_2O_8$.[99] The open circles are the measured susceptibility by a superconducting quantum interference device (SQUID). The solid curve is a model fit by taking into account contribution from the interacting dimers (dashed line), from the impurities following a Curie-Weiss law (dotted line), and from the constant Van Vleck paramagnetic susceptibility (not shown), as given in Eq. (2.10).

where the Van Vleck paramagnetic susceptibility χ_0 is a temperature independent term, χ_{imp} is the contribution from paramagnetic impurities with C_{imp} being the Curie constant of the impurities, and θ the Weiss temperature of the impurities.

Figure 2.2 shows the magnetic susceptibility of a weakly-coupled spin dimer system $Sr_3Cr_2O_8$ as a function of temperature. With decreasing temperature the magnetic susceptibility increases and exhibits a broad maximum at about 30 K. The downturn of this curve indicates the formation of spin dimers. The temperature dependence of the magnetic susceptibility can be well modeled by Eq. (2.10), as shown by the solid line. The contributions from the interacting dimers and from the magnetic impurities are also plotted for comparison. The main temperature-dependent feature has been well captured by the spin-dimer term, except the small residual value at very low temperature where contributions from magnetic impurities are more significant and the Curie-Weiss term has been taken into account.

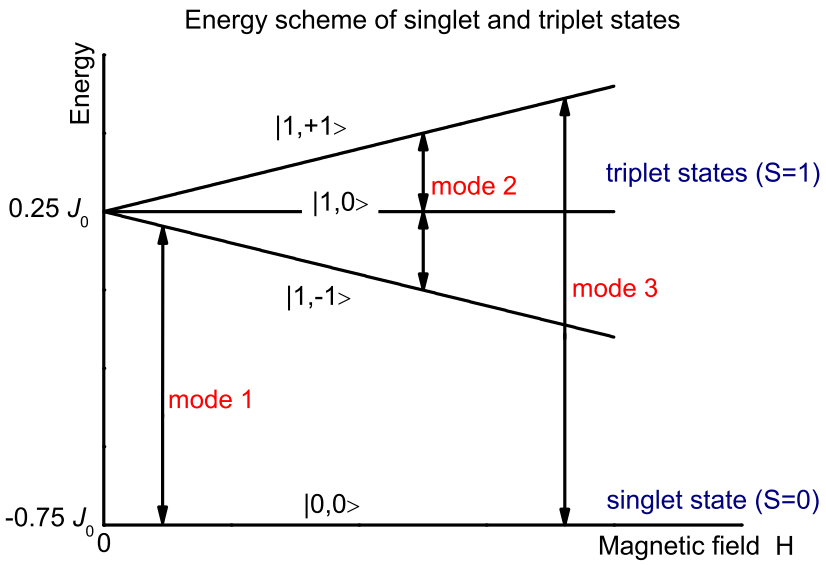

Figure 2.3: Energy scheme of spin-singlet and spin-triplet states of an isolated spin dimer in the presence of a magnetic field. $J_0 > 0$ is the intra-dimer exchange interaction. The spin-triplet states are split in the finite magnetic field due to Zeeman interaction. Modes 1, 3 are the spin singlet-triplet excitations, mode 2 is the intra-triplet excitations.

2.1.4 Electron paramagnetic resonance

A single magnetic ion with electronic spin $S = \frac{1}{2}$ has degenerate spin states, i.e. the spin up and spin down states. In the conventional electron spin resonance measurements, an external static magnetic field $\mathbf{H}$ is applied to split the spin up and spin down states due to the Zeeman energy. The electron can be excited by electromagnetic wave from the lower-lying spin state to the higher-lying spin state. The Hamiltonian of the Zeeman interaction is

$$\hat{H}_{Zeeman} = -\mu \cdot (\mathbf{H} + \mathbf{h}^{\omega}) = g\mu_B \mathbf{S} \cdot \mathbf{H} + g\mu_B \mathbf{S} \cdot \mathbf{h}^{\omega}, \tag{2.11}$$

where $\mathbf{h}^{\omega}$ denotes magnetic field of the electromagnetic wave, μ is the magnetic moment of the ion, g is the Landé g-factor, and μ_B is the Bohr magneton. The electron spin resonance can occur when the radiation magnetic field is perpendicular to the static magnetic field. Such resonance transition is a magnetic-dipole transition with the selection rule $\Delta S_z = \pm 1$.

For an isolated spin dimer based on $S = \frac{1}{2}$ magnetic ions, the spin Hamiltonian can be written as a sum of the exchange term $\hat{H}_{ex}$, a Zeeman term $\hat{H}_{sta}$ due to the applied

static magnetic field, and a Zeeman term $\hat{H}_{osc}$ due to the oscillating magnetic field of the electromagnetic wave

$$\begin{aligned}\hat{H} &= \hat{H}_{ex} + \hat{H}_{sta} + \hat{H}_{osc} \\ &= J_0 \mathbf{S}_1 \cdot \mathbf{S}_2 + g\mu_B \mathbf{H} \cdot (\mathbf{S}_1 + \mathbf{S}_2) + g\mu_B \mathbf{h}^{\omega} \cdot (\mathbf{S}_1 + \mathbf{S}_2). \end{aligned} \tag{2.12}$$

For an antiferromagnetic exchange interaction $J_0 > 0$, the spin-triplet excited states can be completely split in the external static magnetic field. $\hat{H}_{osc}$ can be treated as a time-dependent perturbation, since it is much smaller than the first two terms $\hat{H}_{ex}$ and $\hat{H}_{sta}$.

If $\mathbf{h}^{\omega} \parallel \mathbf{H} \parallel z$, the spin-singlet and spin-triplet states are also the eigenstates of $\hat{H}_{osc}$, thus the electromagnetic wave cannot induce any excitations. The transition within the split triplet state is possible only if the oscillating magnetic field and the applied magnetic field are perpendicular to each other and the photon energy is equal to the energy splitting, i.e.

$$\mathbf{h}^{\omega} \perp \mathbf{H}, \tag{2.13}$$

$$\hbar\omega = g\mu_B H. \tag{2.14}$$

Since the exchange term and the Zeeman term are commutative, S is a good quantum number and the selection rules of the electron paramagnetic resonance transition in a spin dimer are

$$\Delta S = 0, \tag{2.15}$$

$$\Delta S_z = \pm 1. \tag{2.16}$$

Therefore, the excitation from the spin-singlet state ($S = 0$) to the spin-triplet state ($S = 1$) is not magnetic-dipole active. Nevertheless, such excitations with $\Delta S = 1$ are possible if the singlet and triplet states are mixed, e.g. by an asymmetric exchange interaction.

2.1.5 Antisymmetric exchange interaction: Dzyaloshinskii-Moriya interaction

The Dzyaloshinskii-Moriya interaction, named after Dzyaloshinskii[29] and Moriya[69], is a dominant asymmetric exchange interaction arising from spin-orbit coupling and superexchange interactions. The antisymmetric Dzyaloshinskii-Moriya term is expressed as

$$\mathbf{D} \cdot (\mathbf{S_1} \times \mathbf{S_2}) \tag{2.17}$$

with the Dzyaloshinskii-Moriya vector $\mathbf{D}$ and $\mathbf{S_1}$ and $\mathbf{S_2}$ being the spin operators of the two involved ions. Since the Dzyaloshinskii-Moriya interaction should be invariant

under the symmetry operations of the system, the Dzyaloshinskii-Moriya vector must follow the rules imposed by the symmetries. For example, the Dzyaloshinskii-Moriya interaction is not allowed in presence of inversion symmetry, because a factor of -1 is gained by exchanging the two spins. The rules corresponding to single symmetry operations, such as inversion, reflection, and rotation, have been given by Moriya [69] and are summarized in the following.

The two ions 1 and 2 are located at the points A and B, respectively, and the point bisecting the straight line AB is denoted by C.

(i) When an inversion center is located at C,

$$\mathbf{D} = 0.$$

(ii) When a mirror plane perpendicular to AB passes through C,

$$\mathbf{D} \parallel \text{mirror plane or } \mathbf{D} \perp AB.$$

(iii) When there is a mirror plane including A and B,

$$\mathbf{D} \perp \text{mirror plane.}$$

(iv) When a two-fold rotation axis perpendicular to AB passes through C,

$$\mathbf{D} \perp \text{two-fold axis.}$$

(v) When there is an n-fold axis ($n \geq 2$) along AB,

$$\mathbf{D} \parallel AB.$$

For a given crystal structure, all the symmetry elements and the combination of them should be fully considered, in order to determine the properties of the Dzyaloshinskii-Moriya vector. This will be illustrated in Section 4.2 for $Ba_3Cr_2O_8$ and $Sr_3Cr_2O_8$ in detail.

As an antisymmetric exchange interaction, the Dzyaloshinskii-Moriya term is not commutative with the symmetric exchange interaction. Thus the quantum number S is not a good number and the transition from the spin-singlet to spin-triplet state will be allowed. The corresponding selection rules are more complicated and will be discussed in Section 2.1.6 in detail.

2.1.6 Static Dzyaloshinskii-Moriya interaction: Single-dimer model

In the following, we will focus on the single dimer picture and deduce the selection rules in presence of an intra-dimer Dzyaloshinskii-Moriya interaction. The unperturbed

Hamiltonian is given by

$$\begin{aligned} \hat{H} &= \hat{H}_{ex} + \hat{H}_{sta} + \hat{H}_{sdm} && (2.18) \\ &= J_0 \mathbf{S}_1 \cdot \mathbf{S}_2 + g\mu_B \mathbf{H} \cdot (\mathbf{S}_1 + \mathbf{S}_2) + \mathbf{D} \cdot (\mathbf{S}_1 \times \mathbf{S}_2). && (2.19) \end{aligned}$$

Based on the spin-singlet and three spin-triplet states, this Hamiltomian can be represented as a 4×4 matrix. The Dzyaloshinskii-Moriya term will contribute nonzero off-diagonal elements. Depending on the direction of the Dzyaloshinskii-Moriya vector with respect to the applied magnetic field, the singlet state will be mixed with the $S_z = 0$ triplet state or the $S_z = \pm 1$ triplet states.

The applied magnetic field is always set to along the z axis in the following discussions. When the Dzyaloshinskii-Moriya vector is parallel to the applied magnetic field, i.e., $\mathbf{D} \parallel \mathbf{H} \parallel z$, the Hamiltonian in the matrix representation is

$$\hat{H} = \begin{pmatrix} \frac{1}{4}J_0 + g\mu_B H_z & 0 & 0 & 0 \\ 0 & \frac{1}{4}J_0 & 0 & \frac{1}{2}iD \\ 0 & 0 & \frac{1}{4}J_0 - g\mu_B H_z & 0 \\ 0 & -\frac{1}{2}iD & 0 & -\frac{3}{4}J_0 \end{pmatrix}. \qquad (2.20)$$

The eigenenergies and eigenstates can be obtained by diagonalizing this matrix. It reveals that the Dzyaloshinskii-Moriya term mixes the singlet state with the $S_z = 0$ triplet state with a factor of $D/2iJ_0$. In first-order approximation, the hybridized singlet state turns to be

$$|s_0\rangle = |0,0\rangle + \frac{D}{2iJ_0}|1,0\rangle \qquad (2.21)$$

The energies of the singlet state and $S_z = 0$ triplet state will be increased and decreased by a factor of $D^2/4J_0$ at zero field. This means that the degeneracy of the triplet states is partially released with an energy splitting $D^2/4J_0$.

Now we consider the perturbation of $\hat{H}_{osc}$, the Zeeman interaction with the oscillating magnetic field of the electromagnetic wave as given in Eq. (2.12). In general, the excitations from the singlet state to the triplet states are determined by the nonzero matrix elements $\langle t_{+,0,-}|\hat{H}_{osc}|s_0\rangle$, where $|t_{+,0,-}\rangle$ denote the spin-triplet states. It turns out that only the excitations to the $S_z = \pm 1$ are allowed, when the oscillating magnetic field is perpendicular to the direction of Dzyaloshinskii-Moriya vector, i.e. $\mathbf{h}^{\omega} \perp \mathbf{D}$.

When the Dzyaloshinskii-Moriya vector is perpendicular to the applied magnetic field, i.e., $\mathbf{D} \parallel x \perp \mathbf{H} \parallel z$, the Hamiltonian in the matrix representation is

$$\hat{H} = \begin{pmatrix} \frac{1}{4}J_0 + g\mu_B H_z & 0 & 0 & \frac{1}{2\sqrt{2}}iD \\ 0 & \frac{1}{4}J_0 & 0 & 0 \\ 0 & 0 & \frac{1}{4}J_0 - g\mu_B H_z & -\frac{1}{2\sqrt{2}}iD \\ \frac{1}{2\sqrt{2}}iD & 0 & -\frac{1}{2\sqrt{2}}iD & -\frac{3}{4}J_0 \end{pmatrix}. \qquad (2.22)$$

One can readily see that the $S_z = 0$ triplet state is unaffected, while the $S_z = \pm 1$ triplet states are mixed with the singlet state. The mixture has a prefactor of the order of D/J_0. The triplet states are split with energy on the order of D^2/J_0, similar to the case of $\mathbf{D} \parallel \mathbf{H}$.

The selection rules of the singlet-triplet excitations can be similarly obtained by calculating the matrix element $\langle t_{+,0,-}|\hat{H}_{osc}|s_0\rangle$. Since the singlet state is mixed with both the $S_z = -1$ and the $S_z = +1$ triplet states, an oscillating magnetic field along the z direction can induce the transition to these triplet states. Transitions to the $S_z = 0$ triplet state are allowed when the oscillating magnetic field is parallel to the x or the y direction. It is worth to note that the transition to the $S_z = 0$ triplet state is not allowed for $\mathbf{h}^\omega \parallel \mathbf{D}$ at zero field. The selection rules are summarized in Table 2.2.

Table 2.2: Selection rules of the spin singlet-triplet excitations in a singlet spin dimer with Dzyaloshinskii-Moriya interaction. I^+, I^0, I^- denote the nonzero transition probability to the $S_z = +1, 0, -1$ spin-triplet states, respectively.

	$H = 0$			$H \parallel z$		
	D_x	D_y	D_z	D_x	D_y	D_z
h_x^ω	0	I^0	$I^\pm$	I^0	I^0	$I^\pm$
h_y^ω	I^0	0	$I^\pm$	I^0	I^0	$I^\pm$
h_z^ω	$I^\pm$	$I^\pm$	0	$I^\pm$	$I^\pm$	0

At zero magnetic field, the singlet-triplet excitations are allowed when $\mathbf{h}^\omega \perp \mathbf{D}$. The transition to $S_z = 0$ triplet state can be further induced by a finite magnetic field for $\mathbf{h}^\omega \parallel \mathbf{D} \perp \mathbf{H}$.

2.1.7 Dynamical Dzyaloshinskii-Moriya interaction: More-dimer model

The *static* Dzyaloshinskii-Moriya interaction is not allowed in the spin dimer with a center of inversion. In fact, the inversion center can be *instantaneously* broken by an optical phonons on the time scale of phononic excitations, thus a *dynamical* Dzyaloshinskii-Moriya interaction is allowed instantaneously. The electronic excitations can occur on shorter time scales.[22]

The perturbation of the electromagnetic wave on the spin degrees of freedom via phonons is given by

$$\sum_{i,a,\beta,\gamma} e^\beta(t) A_{\beta\gamma}(a)(\mathbf{S}_i \times \mathbf{S}_{i+a})^\gamma, \tag{2.23}$$

where $e^\beta(t)$ is the β component of the *ac* electric field of the electromagnetic wave as a function of time t. The indices i and a refers to the interacting magnetic ions. The

coupling between the electric field β component and the γ component of the spin cross product is noted by the constants $A_{\beta\gamma}(a)$.

The dynamical Dzyaloshinskii-Moriya interaction is still an antisymmetric exchange interaction. Moriya's rules should be applied based on the symmetries of the spin-dimer complex in the instantaneous configuration. In a structure with more than one dimer in a unit cell, all the symmetries in the unit cell should be considered to determine the constraints on the Dzyaloshinskii-Moriya interaction. In the dynamical mechanism, the spin excitation is essentially electric-dipole active, while it is induced by the magnetic-dipole interaction in the static mechanism. Optical phonons play a key role in the dynamical mechanism. The transition intensity is thus determined by the strength of the electric-dipole interaction and the coupling of the phonon to the magnetic exchange interaction. This mechanism can be adapted to explain the observations in the spin-dimer systems $Sr_3Cr_2O_8$ and $Ba_3Cr_2O_8$, as will be discussed in Sec. 4.2.

2.1.8 Dispersion relation of magnons

The elementary magnetic excitation in an isolated spin dimer is the excitation from the spin-singlet ground state to the spin-triplet excited state. In a real material the weak inter-dimer exchange interactions allow magnon to propagate from one dimer to neighboring dimers, thus the magnon acquires a finite bandwidth in the reciprocal space. In a square lattice model with intra-dimer exchange J_0 and inter-dimer exchange J', the dispersion relation of the magnon band to first order in J' is well approximated by [33]

$$E(\mathbf{k}) = J_0 + J'[\cos(k_x a) + \cos(k_y a)] + g\mu_B H_z S_z, \tag{2.24}$$

where the last term is the Zeeman term, (k_x, k_y) denotes a reciprocal vector, and a is the lattice constant. This simple model clearly illustrates that the bandwidth $4|J'|$ is determined by the inter-dimer interaction. For an antiferromagnetic inter-dimer interaction, i.e. $J' > 0$, the bottom of the energy band is achieved at the Brillouin-zone boundary $k_x = k_y = \pm\pi/a$, while the band top is located at the Brillouin-zone center $k_x = k_y = 0$, the so-called Γ point.

Most of the real spin dimerized systems have more complicated dispersion relations. Figure 2.4 shows the magnon dispersion relation in $Sr_3Cr_2O_8$ determined from inelastic neutron scattering experiments by Quintero-Castro et al.[76] The real situation is further complicated by the existence of crystallographic twins. From this figure, one can see three different dispersion branches, which is ascribed to the coexistence of three monoclinic twins at low temperatures.[76] Although the dispersion relation looks different from twin to twin, the extrema in general are located at the zone boundaries or at the zone center. The bandwidth is indeed determined by the inter-dimer interactions. The dispersion relation is degenerate at the Γ point.

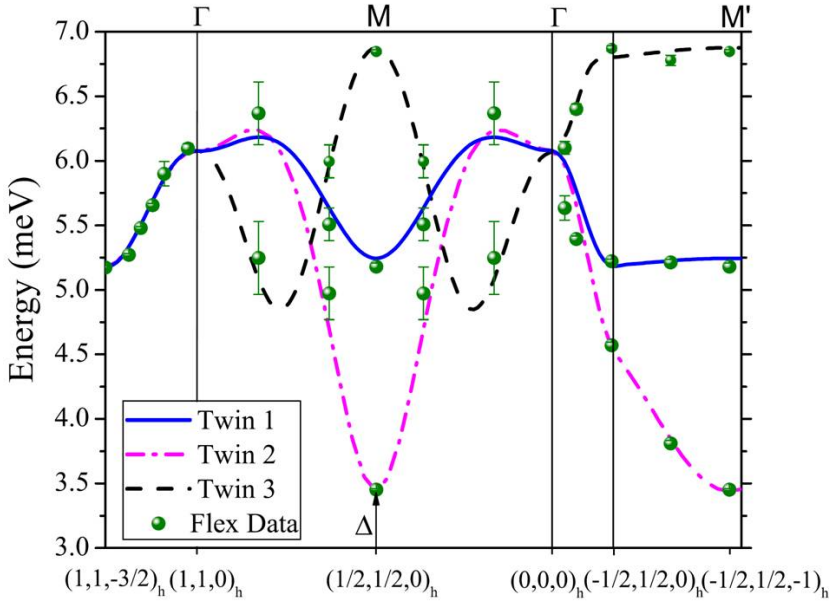

Figure 2.4: Dispersion relation of the singlet-triplet excitation (magnon, $S = 1$) in $Sr_3Cr_2O_8$ determined from inelastic neutron scattering experiments by Quintero-Castro et al. Taken from Ref. [76]

2.1.9 Bose-Einstein condensation of magnons

The spin gap between the spin-singlet and the spin-triplet states can be reduced by applying an external magnetic field, since the Zeeman term can lower the energy of the lower-lying triplet state. Figure 2.5 illustrates the Zeeman effect based on the square lattice model in Eq. (2.24). When the applied magnetic field is large enough, the gap will be closed at a lower critical field H_{c1}, which corresponds to the triplet band bottom touching zero as illustrated in the inset of Fig. 2.5 along the k_x direction. Since the lower-lying triplet state with $S_z = -1$ is magnetic, a finite magnetization appears at H_{c1} (see the inset of Fig. 2.6). Bose-Einstein condensation of magnons can be achieved even at zero temperature when the spin gap is closed. This is a typical example of a quantum phase transition, where the phase transition occurs at zero temperature. The transition point is called quantum critical point.[79]

The applied external magnetic field plays the role of a chemical potential. Introducing a critical field $H_{c1} = \Delta/(g\mu_B)$ with Δ being the magnetic excitation gap, the chemical potential of the magnons can be associated with the external magnetic field by a linear relation $\mu = g\mu_B(H - H_{c1})$. The total magnetization is $M = g\mu_B N$ with N being the total number of magnons.[73, 33] At a higher critical field H_{c2}, the magneti-

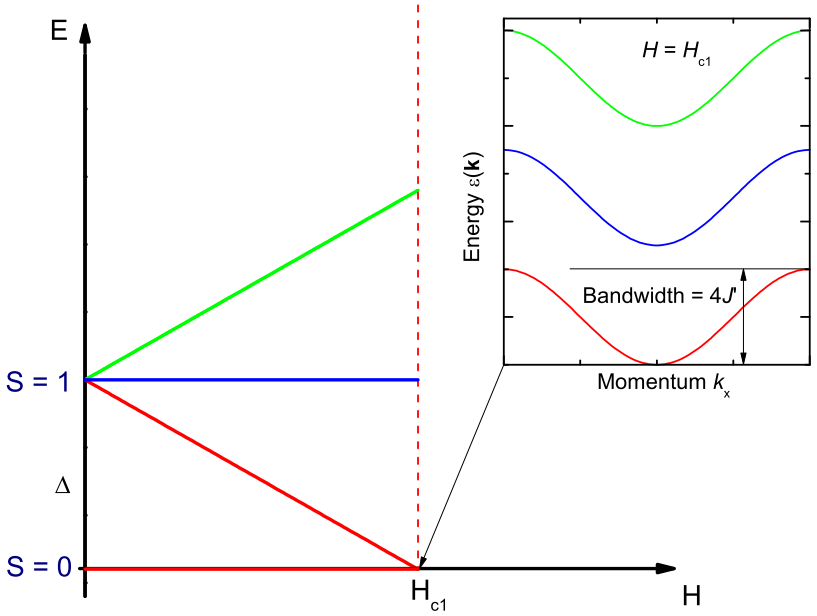

Figure 2.5: Bose-Einstein condensation of magnons can occur when the energy of a dispersive lower-lying triplet state reaches zero at H_{c1}. The inset shows the dispersion relation of the lower-lying triplet state at the critical field H_{c1}. Each triplet branch has a bandwidth $4J'$, see Eq. (2.24). Adapted from Ref. [33]

zation saturates and all the dimers are fully occupied by magnons. Thus, the magnon condensation occurs between H_{c1} and H_{c2}. The magnon condensation can also survive at finite temperature. In the temperature-field diagram, the phase of Bose-Einstein condensation looks like a dome, see Fig. 2.6.[33] Close to zero temperature, the temperature dependence of the critical magnetic field obeys a power low

$$H_c(T) - H_{c1} \propto T^{3/2}. \tag{2.25}$$

At zero temperature $H_c(0) = H_{c1}$. The critical exponent 3/2 corresponds to the so-called XY universality class of three-dimensional Bose-Einstein condensation of magnons. The condensation phase is an XY-antiferromagnetic phase with transverse magnetic order. The spins in the XY plane can point any direction, thus this magnetic order has U(1) symmetry.

The magnons in the quantum magnetic system are not free bosons, because each dimer can host at most one magnon. Magnon interaction results from the longitudinal components of the exchange interaction, while the transverse components give rise to

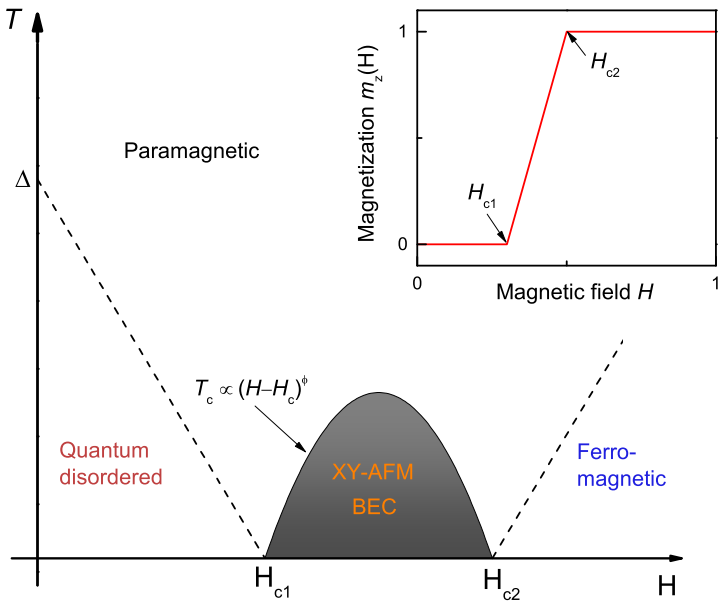

Figure 2.6: Phase diagram with paramagnetic, quantum disordered, field-aligned ferromagentic phases, and canted-antiferromagnetic (XY-AFM) phase where Bose-Einstein condensation of magnons occurs. At the phase boundary close to H_{c1} and H_{c2}, critical temperature T_c follows a power law $(H-H_c)^{\phi}$ with a universal exponent $\phi = 2/3$ for the XY universality class of magnon Bose-Einstein condensation. The inset shows the magnetization curve $m_z(H)$ for a three-dimensional dimer spin system with plateaus at $m_z = 0$ and 1. Adapted from Ref. [33]

hopping of magnons. In the low-density and low-temperature limit, magnon-magnon interaction can be approximated by a non-dispersive two-particle interaction.[73, 28] Model calculations demonstrated that the power law given by Eq. (2.25) is still followed in close vicinity of the critical field.[73, 28] Dispersive two-particle interactions were also investigated theoretically to provide a better quantitative agreement with experimental results.[90]

The XY universality class of magnon condensation is not easily realized experimentally. A small anisotropy will be important and break the U(1) symmetry when the system approaches zero temperature. Reported specific heat experiments indicate that $Sr_3Cr_2O_8$ has a critical exponent of the XY universality class, while $Ba_3Cr_2O_8$ does not. By state-of-the-art high-field neutron experiments it was determined that $Ba_3Cr_2O_8$ has a commensurate and collinear transverse spin component

for $H_{c1} < H < H_{c2}$.[58] Such experiments are not yet available in high fields up to $H_{c1} \sim 30$ T for $Sr_3Cr_2O_8$.

2.1.10 Jahn-Teller effect: The $E \otimes e$ problem

In solids, the motions of nuclei and electrons are determined by solving the Schrödinger equation of a full wavefunction $\Psi(r, Q)$,

$$(H - E)\Psi(r, Q) = 0, \tag{2.26}$$

where r and Q denote the whole set of coordinates of the electrons r_i, $i = 1, 2, ...$ and nuclei Q_j, $j = 1, 2, ...$ The total Hamiltonian consists of three parts[13]

$$H = H_r + H_Q + V(r, Q), \tag{2.27}$$

where H_r is the electronic part including the kinetic energy of electrons and the inter-electronic electrostatic interaction, H_Q is the kinetic energy of the nuclei, and $V(r, Q)$ takes into account the interaction of the electrons with the nuclei and internuclear repulsion. $V(r, Q)$ can be expanded as a series of small displacements of the nuclei about the origin point $Q_j = Q_{j0} = 0$. Taking $V(r, 0)$ as the potential energy of the electrons in the field of nuclei fixed at $Q_{j0} = 0$, one can solve the electronic part of the Schrödinger equation

$$[H_r + V(r, 0) - \varepsilon'_k]\varphi_k(r) = 0 \tag{2.28}$$

and obtain a set of energies ε'_k and wavefunctions $\varphi_k(r)$ for the given nuclear configuration corresponding to the point $Q_{j0} = 0$. Here, the adiabatic approximation has been used, where the nuclei are assumed to be fixed at the equilibrium positions.

In order to consider the effect of the changes in the electron structure on nuclear dynamics, the total wavefunction $\Psi(r, Q)$ must be calculated, which can be expanded in terms of $\varphi_k(r)$,

$$\Psi(r, Q) = \sum_k \chi_k(Q)\varphi_k(r), \tag{2.29}$$

where the expansion coefficients $\chi_k(Q)$ as functions of the nuclear coordinates should fulfill

$$[H_Q + \varepsilon_k(Q) - E]\chi_k(Q) + \sum_{m \neq k} W_{km}(Q)\chi_m(Q) = 0 \tag{2.30}$$

where $W_{km}(Q) = \langle \varphi_k(r)|W(r, Q)|\varphi_m(r)\rangle$ denotes the electronic matrix element of vibronic interactions with

$$\begin{aligned} W(r, Q) &= V(r, Q) - V(r, 0) \\ &= \sum_\alpha (\partial V/\partial Q_\alpha)_0 Q_\alpha + \frac{1}{2}\sum_{\alpha,\beta} (\partial^2 V/\partial Q_\alpha \partial Q_\beta)_0 Q_\alpha Q_\beta + ... \end{aligned}$$

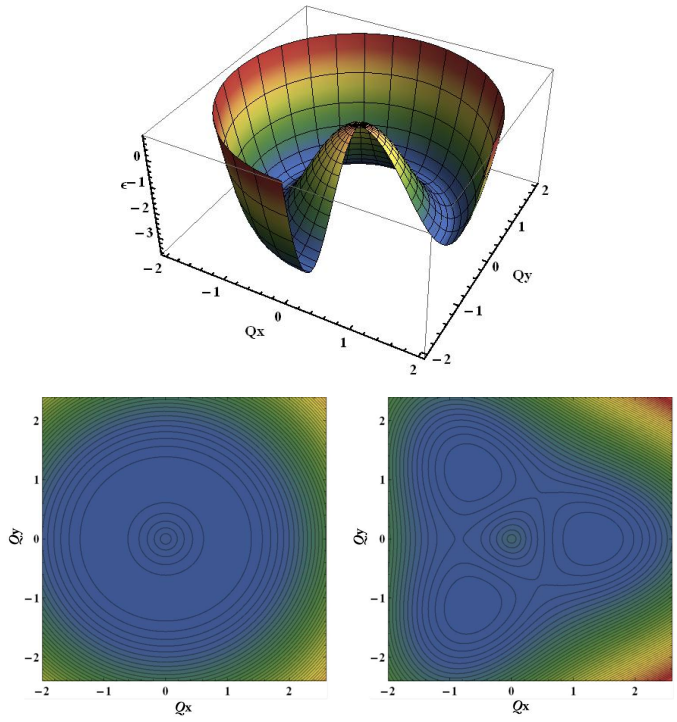

Figure 2.7: Upper panel: The adiabatic potential energy surface of the $E \otimes e$ problem with linear vibronic coupling, illustrated with azimuthal angle up to 1.5π. Lower panel: Contour plot of the adiabatic potential energy surface with linear vibronic coupling (left), and with linear and quadratic vibronic coupling (right).

and

$$\varepsilon_k(Q) = \varepsilon'_k + W_{kk}(Q) \tag{2.31}$$

is the potential energy of the nuclei in the mean field of the electrons in the state $\varphi_k(r)$. If vibronic mixing of different electronic states can be ignored, i.e., $W_{km}(Q) = 0$ for $k \neq m$, coupling between these states vanishes, and the system of equations decomposes into a set of simple equations.

The $E \otimes e$ problem

In a tetrahedral crystal field the central ions have lower-lying doubly degenerated E orbitals ($\vartheta \sim d_{z^2}$ and $\epsilon \sim d_{x^2-y^2}$) and higher-lying triply degenerate T orbitals

(d_{xy}, d_{yz} and d_{xz}). The two component of the normal E-type displacements are $Q_\vartheta = (X_1 - X_2 - X_3 + X_4)/2$ and $Q_\epsilon = (Y_1 - Y_2 - Y_3 + Y_4)/2$.

We consider the expansion of $W(r, Q)$ to the second order in Q. Except the terms of Q_ϑ and Q_ϵ, the other terms contribute to $\varepsilon_k(Q)$ in a simple parabolic form with respect to $Q_\Gamma = 0$.

$$\varepsilon_k(Q) = \frac{1}{2}\sum_{\Gamma\neq\vartheta,\epsilon} K_\Gamma Q_\Gamma^2 + \frac{1}{2}K_E(Q_\vartheta^2 + Q_\epsilon^2) + \varepsilon_k^\nu(Q_\vartheta, Q_\epsilon), \quad k = 1, 2 \tag{2.32}$$

where ε^ν are the roots of the secular equation

$$\begin{vmatrix} W_{11} - \varepsilon^\nu & W_{12} \\ W_{21} & W_{22} - \varepsilon^\nu \end{vmatrix} = 0. \tag{2.33}$$

The four matrix elements of the vibronic interaction W can be evaluated as[13]

$$\begin{pmatrix} F_E Q_\vartheta + G_E(Q_\vartheta^2 - Q_\epsilon^2) & -F_E Q_\vartheta + 2G_E Q_\vartheta Q_\epsilon^2 \\ -F_E Q_\vartheta + 2G_E Q_\vartheta Q_\epsilon^2 & -F_E Q_\vartheta - G_E(Q_\vartheta^2 - Q_\epsilon^2) \end{pmatrix} \tag{2.34}$$

by introducing one linear and one quadratic constant, respectively,

$$F_E = \langle\vartheta| \left(\frac{\partial V}{\partial Q_\vartheta}\right) |\vartheta\rangle, G_E = \langle\vartheta| \left(\frac{\partial^2 V}{\partial Q_\vartheta \partial Q_\epsilon}\right) |\epsilon\rangle. \tag{2.35}$$

We use the polar coordinates $Q_\vartheta = \rho\cos\phi$ and $Q_\epsilon = \rho\sin\phi$, thus the solution of the secular equation Eq. (2.33) gives

$$\varepsilon_\pm(\rho, \phi) = \frac{1}{2}K_E\rho^2 + \varepsilon_\pm^\nu \tag{2.36}$$

$$= \frac{1}{2}K_E\rho^2 \pm \rho[F_E^2 + G_E^2\rho^2 + 2F_E G_E \rho\cos(3\phi)]^{\frac{1}{2}}. \tag{2.37}$$

In the linear coupling case, i.e., neglecting the quadratic terms ($G_E = 0$), the adiabatic potential energy surface simplifies to

$$\varepsilon_\pm(\rho, \phi) = \frac{1}{2}K_E\rho^2 \pm |F_E|\rho \tag{2.38}$$

with minima at $\rho_0 = |F_E|/K_E$. The adiabatic potentials with and without the quadratic term are illustrated in Figure 2.7.

Jahn-Teller stabilization energy E_{JT}^E is the energy difference between the minimum value and the value at $\rho = 0$. In the linear coupling case, it is

$$E_{JT}^E = F_E^2/2K_E. \tag{2.39}$$

2.2 Spin chain

2.2.1 Spin-1 Heisenberg chain

The model of one-dimensional Heisenberg antiferromagnet can be described by

$$\hat{H} = \sum_{i=1}^{N} J_i (S_i^x S_{i+1}^x + S_i^y S_{i+1}^y + S_i^z S_{i+1}^z) \tag{2.40}$$

with nearest-neighbour exchange interaction $J_i > 0$. F.D.M. Haldane has distinguished two variants of this model with integral or half-integral spins in 1980s.[40, 41] Depending on whether the spin S is integral or half-integral, this model exhibits a gapped or gapless elementary magnetic excitations. For the integral spin case, the ground state is a disordered nonmagnetic singlet ground state $S = 0$ and the excited state is a gapped spin-triplet state with $S = 1$, similar to the characteristic states of the spin-dimer systems. The magnetic susceptibility indeed exhibits similar temperature dependence as that of the spin-dimer systems [see Fig. 2.2 and Fig. 6.1(c)]. The Haldane gap of a spin-1 Heisenberg chain is $0.41J$ as evaluated with a numerical density matrix renormalization group technique by S.R. White and coauthors.[100] T. Sakai and M. Takahashi considered further the inter-chain interaction and single-ion anisotropy and adopted the mean field theory to investigate the following Hamiltonian [82]

$$\hat{H} = \sum_{<i,j>_\parallel} \mathbf{S}_i \mathbf{S}_j + J \sum_{<i,j>_\perp} \mathbf{S}_i \mathbf{S}_j + D \sum_i (S_i^z)^2, \tag{2.41}$$

where $< i, j >_\parallel$ and $< i, j >_\perp$ refer to the intra-chain and inter-chain nearest-neighbor spin pairs, respectively. The intra-chain exchange interaction is set as energy unit, thus D and J are the reduced single-ion anisotropy and inter-chain exchange interaction with respect to the intra-chain interaction. Based on this Hamiltonian, they established a phase diagram in the $D - J$ plane for the ground state, which is also confirmed recently by K. Wierschem and P. Sengupta using quantum Monte Carlo simulations.[101], as shown in Fig. 2.8.

Without the single-ion anisotropy ($D = 0$), the Heisenberg model does not exhibit the long-range magnetic order for a small finite inter-chain coupling even at zero temperature, in contrast to the Ising model discussed in Sec. 2.2.2. Ising or XY antiferromagnetic ordering can be achieved for sufficiently large easy-axis or easy-plane single-ion isotropy, respectively.

2.2.2 Spin-1/2 Ising chain

The Hamiltonian of a one-dimensional ferromagnetic Ising model can be written as

$$\hat{H} = -\sum_{i=1}^{N} J_i S_i^z S_{i+1}^z + g\mu_B H_z \sum_{i=1}^{N} S_i^z, \tag{2.42}$$

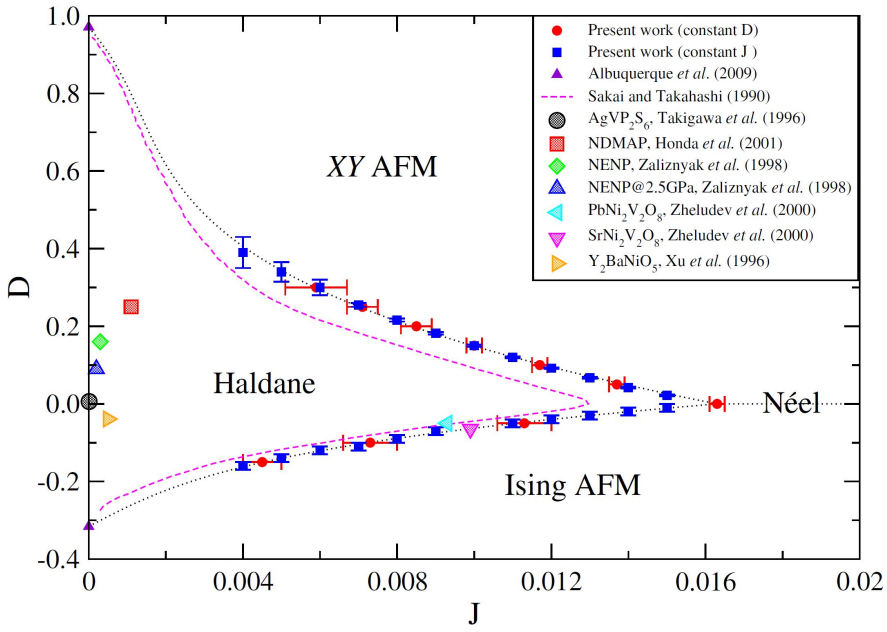

Figure 2.8: Phase diagram in the D – J plane for the ground state of a quasi-one-dimensional system. D and J are the single-ion anisotropy and inter-chain exchange interaction reduced by the intra-chain interaction, see Eq. (2.41). Taken from Ref. [101]

where the first term takes into account the nearest-neighbor exchange interactions, the second term is the Zeeman interaction term in an applied magnetic field H_z, i refers to the sites of magnetic ions, $J_i = J > 0$ denotes the nearest-neighbor ferromagnetic exchange interaction, g and μ_B are the effective g-factor and the Bohr magneton, respectively. The magnetization for an infinite spin chain ($N \to \infty$) can be obtained by solving this model analytically

$$M(H_z, T) = \lim_{N\to\infty} \frac{m(H_z, T)}{N} = g\mu_B S \frac{\sinh(\beta g \mu_B H_z S)}{\sqrt{\sinh(\beta g \mu_B H_z S)^2 + e^{-4\beta J S^2}}}, \tag{2.43}$$

where S is the spin of each magnetic ion and $\beta = 1/k_B T$ with the Boltzmann constant k_B and temperature T. Equation (2.43) means that the magnetization should be zero at finite temperature when there is no applied magnetic field, so the one-dimensional Ising chain cannot sustain long range order at finite temperature without external magnetic field.

The spin chains are not isolated in solids. The weak interactions between the chains are important at low temperature. The Hamiltonian for a two-dimensional model with

weakly-coupled Ising chains in an external magnetic field can be written as [84]

$$\hat{H} = -\sum_{ij}(J_{\parallel}S^z_{i+1,j}S^z_{ij} + J_{\perp}S^z_{i,j+1}S^z_{ij}) + g\mu_B H_z \sum_{ij} S^z_{ij}, \tag{2.44}$$

with $J_{\parallel}$ the intra-chain exchange interaction, $J_{\perp}$ the nearest-neighbor inter-chain exchange interaction, i the site index in a chain, and j the chain index. In the weak coupling regime $J_{\parallel} \gg J_{\perp}$, the inter-chain coupling can be treated as an effective internal magnetic field. For the simplest ferromagnetic case, the two-dimensional model can be reduced to one-dimensional with the mean-field approximation

$$\hat{H} = -\sum_{i} J_{\parallel}S^z_i S^z_{i+1} + g\mu_B H_{eff} \sum_i S^z_i, \tag{2.45}$$

where the effective field

$$H_{eff} = H_z - 2J_{\perp}\langle S^z \rangle. \tag{2.46}$$

Substituting this into the Eq. (2.43), one can readily see that magnetic ordering with finite magnetization can be stabilized at low temperatures by the internal field even without applied magnetic field.

Spinon excitations

The ground state of an ideal Ising chain corresponds to the parallel or antiparallel alignment of neighboring spins for the ferromagnetic or antiferromagnetic nearest-neighbor exchange interactions, respectively. Figure 2.9(a) illustrates the elementary magnetic excitations of an Ising ferromagnetic spin-1/2 chain. A single spin flip creates two domain walls and frustrates the exchange interactions with its neighbors, so it costs energy J. Subsequent spin flips cost no energy because the exchange interactions are frustrated only at the domain walls. Thus, the two domain walls or spinons can propagate independently along the chain with subsequent spin flips, as illustrated in Fig. 2.9(b). The first excited state with energy J has a large number of degeneracy.

For the Ising antiferromagnetic chain, the elementary magnetic excitations can be described in a similar way. Two domain walls or spinons are created by a spin flip and allowed to propagate by subsequent spin flips without energy cost, see Fig. 2.9(c)(d). Since a spin flip changes the total spin by 1, each spinon carries spin 1/2. Depending on whether odd or even number of spin flips, the total spin is either one or zero, respectively.

2.2.3 Spin-1/2 Ising-like XXZ antiferromagnetic chain

The Ising-like XXZ Hamiltonian of a one-dimensional antiferromagnet is written as

$$\hat{H} = J\sum_{i=1}^{N}\left[S^z_i S^z_{i+1} + \epsilon(S^x_i S^x_{i+1} + S^y_i S^y_{i+1})\right] + g\mu_B \sum_{i=1}^{N} \mathbf{H}\cdot\mathbf{S}_i, \tag{2.47}$$

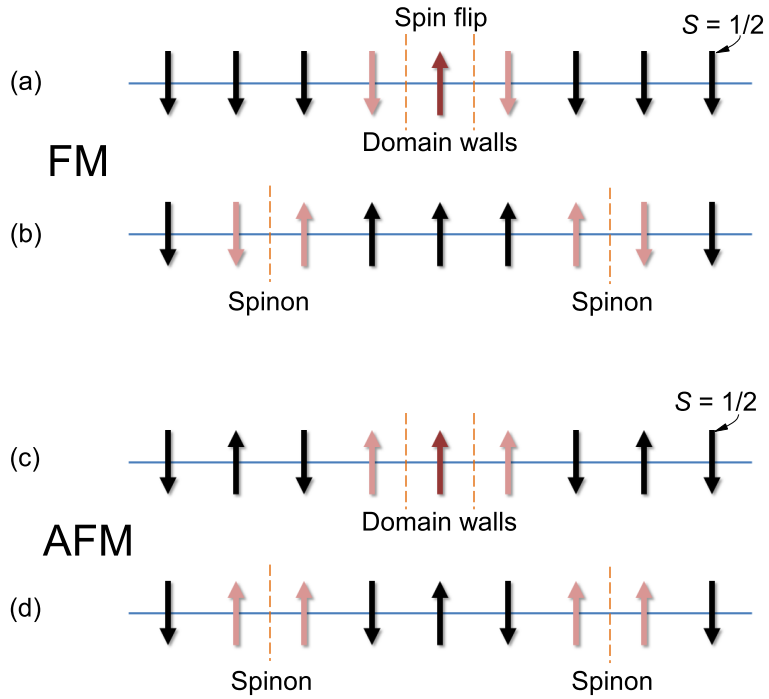

Figure 2.9: (a)(b) Ising ferromagnetic (FM) and (c)(d) antiferromagnetic (AFM) chains constituted by $S = 1/2$ spins. (a)(c) Two domain walls (spions) are created by a single spin-flip (dark red). (b)(d) The two domain walls or spinons (light red) propagate independently by spin flips.

where $\epsilon(S_i^x S_{i+1}^x + S_i^y S_{i+1}^y)$ is the finite transverse (XY) term with $0 < \epsilon < 1$, and $\mathbf{H}$ is the applied external magnetic field. This Hamiltonian corresponds to the Ising model when $\epsilon = 0$, the Heisenberg model when $\epsilon = 1$, and the XY-like XXZ model when $\epsilon > 1$.

The degeneracy of the two-spinon excitation state for the Ising model is removed by the finite transverse term. This will lead to an energy continuum of the two-spinon excitations for an infinite chain. In the limit of small ϵ, N. Ishimura and H. Shiba calculated the continuum to the first order of ϵ.[46] The upper and lower energy boundaries of the excitation continuum can be described by cosine functions

$$\omega(Q_z) = J(1 \pm 2\epsilon \cos Q_z). \tag{2.48}$$

The threshold energy of the two-spinon excitation $J(1 - 2\epsilon)$ increases with decreasing ϵ and reduces to J in the pure Ising limit. The energy boundaries deviate from the cosine function for larger ϵ. The exact calculations were performed by Bougourizi,

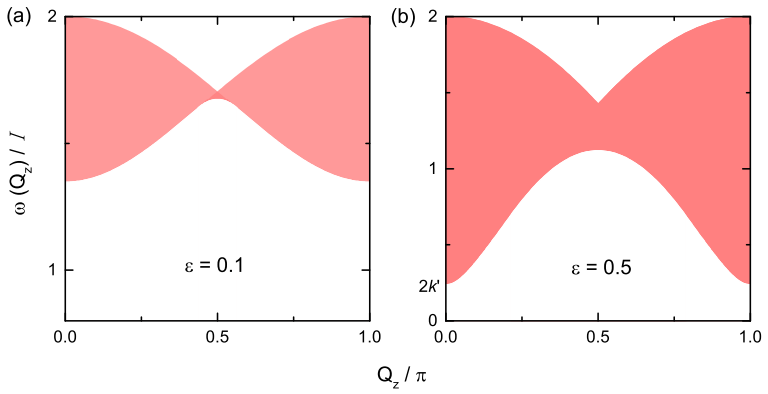

Figure 2.10: Two-spinon excitation spectrum (a) for $\epsilon = 0.1$ and (b) for $\epsilon = 0.5$ following the work by Bougourzi et al.[18]

Karbach, and Müller.[18] Following their work, the lower boundary of the continuum is given by

$$\omega_l(Q_z) = \begin{cases} \dfrac{2I}{1+\kappa}\sqrt{1+\kappa^2-2\kappa\cos Q_z}, & 0 \le Q_z \le Q_k \\ \dfrac{2I}{1+\kappa}\sin Q_z, & Q_k \le Q_z \le \pi - Q_k \\ \dfrac{2I}{1+\kappa}\sqrt{1+\kappa^2+2\kappa\cos Q_z}, & \pi - Q_k \le Q_z \le \pi \end{cases}$$

and the upper boundary is

$$\omega_u(Q_z) = \begin{cases} \dfrac{2I}{1+\kappa}\sqrt{1+\kappa^2+2\kappa\cos Q_z}, & 0 \le Q_z \le \pi/2 \\ \dfrac{2I}{1+\kappa}\sqrt{1+\kappa^2-2\kappa\cos Q_z}, & \pi/2 \le Q_z \le \pi \end{cases}$$

where $\kappa \equiv \cos Q_\kappa = \frac{1-k'}{1+k'}$. The parameters k' and $k \equiv \sqrt{1-k^2}$ are moduli of elliptic integrals $K' \equiv K'(k')$ and $K \equiv K(k)$, which are related to ϵ and J via

$$\frac{1}{\epsilon} = \cosh\frac{\pi K'}{K}, \tag{2.49}$$

$$J = \frac{I\pi}{K}\coth\frac{\pi K'}{K}. \tag{2.50}$$

The continuum is illustrated in Fig. 2.10 (a) for $\epsilon = 0.1$ and in Fig. 2.10 (b) for $\epsilon = 0.5$. For $\epsilon = 0.5$ the energy bounds cannot be described by the cosine functions.

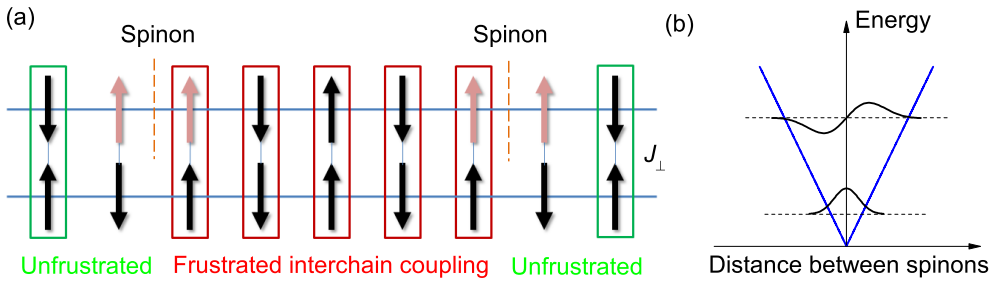

Figure 2.11: (a) inter-chain exchange interactions $J_\perp$ are frustrated between the two spinons. (b) The interaction energy increases linearly with increasing distance between the two spinons.[35]

Close to the Γ point ($Q_z \to 0$), the lower bound can be written as

$$\omega_l(Q_z \to 0) = 2Ik' \left[1 + \frac{\kappa}{2(1-\kappa)^2} Q_z^2\right], \tag{2.51}$$

which is a quadratic function of the reciprocal vector Q_z.

Spinon confinement

In a solid, the small inter-chain exchange interaction can stabilize long-range magnetic order at very low temperature, as illustrated in Sec. 2.2.2. We will see in this section that spinon confinement can be realized below the magnetic ordering temperature. We restrict the discussion to the antiferromagnetic chain that is realized in $SrCo_2V_2O_8$, the main topic of Sec. 6.3. It is very similar for the ferromagnetic case.

Figure 2.11(a) shows two antiferromagnetic Ising chains coupled by a small antiferromagnetic interaction $J_\perp$. A spin flip will frustrate not only the intra-chain exchange interaction J but also the inter-chain interaction. Subsequent spin flips will cost more energy since more inter-chain interactions are frustrated. The propagation of the spinons is thus not independent, but a two-spinon bound state is formed.

Figure 2.11(b) illustrates the linear increase of the inter-chain interaction as function of the distance between two spinons. The excitation spectrum is not the characteristic continuum for free spinons, but composed of quantized levels of spinon bound states.

The spinon bound states can be described by the one-dimensional Schrödinger equation

$$-\frac{\hbar^2}{\mu}\frac{d^2\varphi}{dz^2} + \lambda|z|\varphi = (E - 2E_0)\varphi, \tag{2.52}$$

with a potential $-\lambda|z|$ linear in the spinon-spinon distance z. The potential energy depends on the inter-chain antiferromagnetic exchange interaction $J_\perp$. Thus λ, with

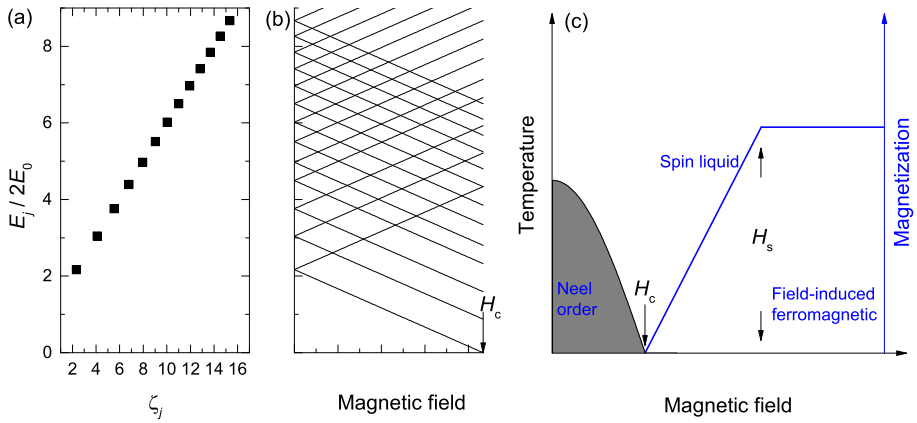

Figure 2.12: (a) Eigenenergies of spinon-pair bound states $E_j/2E_0$ versus ζ_j for $\left(\lambda^2\hbar^2/\mu\right)^{1/3}/(2E_0) = 0.5$. (b) Zeeman split of spinon-pair excitations in a longitudinal magnetic field. (c) Long-range antiferromagnetic order is stabilized at finite temperature due to inter-chain coupling. An order-disorder transition is induced at H_c, where the lower-lying spinons soften and the magnetization onsets. Above H_s ferromagnetic order is induced together with the magnetization saturation.

a dimension of energy density, can be defined via

$$\lambda = \sum_{<jj'>} J_\perp S_j S_{j'}/c \tag{2.53}$$

with $< jj' >$ referring to all the frustrated inter-chain spin pairs in the unit cell along the z direction. A quadratic dispersion relation has been assumed in Eq. (2.52), which is valid close to the Γ point ($Q_z \simeq 0$) in the reciprocal space. The solution of Eq. (2.52) gives the eigenenergies of the spinon-pair bound states[68]

$$E_j = 2E_0 + \zeta_j \lambda^{2/3} \left(\frac{\hbar^2}{\mu}\right)^{1/3} \qquad j = 1, 2, 3, ... \tag{2.54}$$

The sequence of the bound states is specified by the prefactors ζ_j that are the negative zeros of the Airy function $Ai(-\zeta_j) = 0$, $\zeta_j = 2.338, 4.088, 5.520, ...$ ($j = 1, 2, 3, ...$). $2E_0$ is the energy threshold for creating a free spinon pair. Energy hierarchy of the spinon bound-states are illustrated in Fig. 2.12(a) for $\left(\lambda^2\hbar^2/\mu\right)^{1/3}/(2E_0) = 0.5$.

2.2.4 Magnetic field induced quantum phase transitions

Spin-1 Heisenberg antiferromagnetic chain. A field-induced Bose-Einstein condensation of magnons can also occur in the Spin-1 Heisenberg chain systems.[103] It is a

disorder-to-order quantum phase transition and very similar to the situation in the spin dimer systems: the ground state is spin-singlet state and the elementary excitations are the spin-one magnons; the spin gap can be reduced and closed by applying an external magnetic field. The condensation phase is also dome-like in the temperature-field plot as shown in Fig. 2.6. Other types of disorder-to-order quantum phase transitions, such as from the Haldane phase to the Ising or XY antiferromagnetic phases depending on the systems, can be also induced by the magnetic fields.[38, 77] Quantum phase transition in a typical spin-1 antiferromagnetic chain system $SrNi_2V_2O_8$ will be discussed in Sec. 6.2.

Spin-1/2 Ising XXZ antiferromagnetic chain. Quantum phase transitions can be also induced by applying magnetic fields in the quasi-one-dimensional Ising chain systems.[39, 15] At zero field, long-range antiferromagnetic order is stabilized at finite temperature due to inter-chain coupling [Fig. 2.12(c)]. A longitudinal external magnetic field can suppress the inter-chain coupling and reduce the ordering temperature. When the inter-chain coupling is completely suppressed at H_c, the spinon excitation gap is closed [Fig. 2.12(b)] and an *order-to-disorder* phase transition is induced. Magnetization onsets at H_c and saturates at H_s. Between H_c and H_s the system is in a spin-liquid phase. These field-dependent properties will be illustrated in $SrCo_2V_2O_8$ in Sec. 6.4.

3 Low Energy Optical Spectroscopy

3.1 Optical response functions

The dynamics of electromagnetic waves is governed by Maxwell equations. In vacuum, the Maxwell equations are:

$$\nabla \cdot \mathbf{E} = 4\pi\rho, \tag{3.1}$$
$$\nabla \cdot \mathbf{B} = 0, \tag{3.2}$$
$$\nabla \times \mathbf{E} = -\frac{1}{c}\frac{\partial \mathbf{B}}{\partial t}, \tag{3.3}$$
$$\nabla \times \mathbf{B} = \frac{4\pi}{c}\mathbf{J} + \frac{1}{c}\frac{\partial \mathbf{E}}{\partial t}. \tag{3.4}$$

$\mathbf{E}$ and $\mathbf{B}$ are electric field and magnetic induction, respectively. $\mathbf{J}$ and ρ are total current density and total charge density.

Response of matter to electromagnetic waves is characterized by the induced polarization $\mathbf{P}$ and magnetization $\mathbf{M}$. The polarization and magnetization can be generally expanded as a function of electric and magnetic fields of the electromagnetic wave, respectively.

$$P_i = \sum_j \chi^e_{ij} E_j + \sum_{jk} \gamma^e_{ijk} E_j E_k + ..., \tag{3.5}$$
$$M_i = \sum_j \chi^m_{ij} H_j + \sum_{jk} \gamma^m_{ijk} H_j H_k + ..., \tag{3.6}$$

where $i, j, k, ... = 1, 2, 3$ specify the electric or magnetic components. χ^e_{ij}, χ^m_{ij} are the linear dielectric and magnetic susceptibility, respectively. γ^e_{ij}, γ^m_{ij} are the quadratic susceptibilities, and so on.

Using the constitution relations in a medium

$$\mathbf{D} = \mathbf{E} + 4\pi\mathbf{P} = \epsilon\mathbf{E}, \tag{3.7}$$
$$\mathbf{B} = \mathbf{M} + 4\pi\mathbf{M} = \mu\mathbf{H}, \tag{3.8}$$

with the dielectric permittivity $\mathbf{D}$, the magnetic induction $\mathbf{B}$, the dielectric permittivity ϵ, and the magnetic permeability μ, the Maxwell equations can be rewritten

as

$$\nabla \cdot \mathbf{D} = 4\pi\rho_{ext}, \tag{3.9}$$

$$\nabla \cdot \mathbf{B} = 0, \tag{3.10}$$

$$\nabla \times \mathbf{E} = -\frac{1}{c}\frac{\partial \mathbf{B}}{\partial t}, \tag{3.11}$$

$$\nabla \times \mathbf{H} = \frac{4\pi}{c}\mathbf{J}_{cond} + \frac{1}{c}\frac{\partial \mathbf{D}}{\partial t}, \tag{3.12}$$

where ρ_{ext} denotes the external charge density outside the medium and $\mathbf{J}_{cond}$ denotes the current density of conduction electrons in the medium. Electrodynamic properties of a matter can be obtained by solving these equations.

3.1.1 The Lorentz oscillator

The response of phonons to electromagnetic waves can be described by the Lorentz model. This model can be derived by classical consideration: for a pair of positive and negative ions with equal amount of charge q, mass m_1 and m_2, displacement vectors $\mathbf{u}$ and $\mathbf{v}$, respectively. The relative movement can induce an electric dipole $\mathbf{p} = q(\mathbf{u}-\mathbf{v})$. As approximated as a damped harmonic oscillator, the equation of motion about the dipole in an oscillating electric field $\mathbf{E}$ is

$$\frac{d^2\mathbf{P}}{dt^2} + \gamma\frac{d\mathbf{P}}{dt} + \omega_{TO}^2\mathbf{P} = \frac{Nq^2}{mV}\mathbf{E}, \tag{3.13}$$

where there are N dipoles within a volume V, the polarization $\mathbf{P} = \frac{N\mathbf{p}}{V}$, γ is the damping coefficient, $\omega_{TO} = \frac{k}{m}$ is the characteristic frequency of the lattice vibration with the spring constant k, and $m = \frac{m_1 m_2}{m_1+m_2}$ is the effective mass. The oscillating electric field with frequency ω can be written as $\mathbf{E} = \mathbf{E_0}\exp(i\omega t)$, thus the dielectric constant can be solved as

$$\epsilon(\omega) = \epsilon_\infty + \frac{\Omega_p^2}{\omega_{TO}^2 + i\gamma\omega - \omega^2}, \tag{3.14}$$

where ϵ_∞ is the dielectric constant when $\omega \to \infty$, and $\Omega_p^2 \equiv q^2N/\epsilon_0 mV$. When there are n oscillators, the dielectric constant is

$$\epsilon(\omega) = \epsilon_\infty + \sum_{j=1}^{n}\frac{\Omega_{p,j}^2}{\omega_{TO,j}^2 + i\gamma_j\omega - \omega^2}. \tag{3.15}$$

3.1.2 Fresnel equations

The incident electromagnetic wave from one medium to another can be refracted and reflected at the boundary, see Figure 3.1. By solving the Maxwell equations, the refracted and reflected waves can be calculated in terms of electric permittivities and magnetic permeabilities of the two materials, which are the Fresnel equations. When the electric field of incident wave is perpendicular to the plane of incidence [s-polarized, Figure 3.1 (a)], the relative amplitude of reflected wave and incident wave is [49]

$$\frac{E_s''}{E_s} = \frac{n\mu' \cos\alpha - \mu\sqrt{n'^2 - n^2\sin^2\alpha}}{n\mu' \cos\alpha + \mu\sqrt{n'^2 - n^2\sin^2\alpha}}. \tag{3.16}$$

If the electric field of the incident wave is parallel to the plane of incidence [p-polarized, Figure 3.1 (b)], the intensity ratio is

$$\frac{E_p''}{E_p} = \frac{n'^2\mu \cos\alpha - n\mu'\sqrt{n'^2 - n^2\sin^2\alpha}}{n'^2\mu \cos\alpha + n\mu'\sqrt{n'^2 - n^2\sin^2\alpha}}, \tag{3.17}$$

where n and n' are the indices of refraction of incident material and the refractive material, μ and μ' are the magnetic permeabilities, respectively, and α is the incident angle. The Snell's relation

$$n\sin\alpha = n'\sin\beta \tag{3.18}$$

has been used to give the above relations.

If the magnetic permeability is close to each other in both materials, *i.e.* $\mu' \approx \mu$, Eq. (3.16) and Eq. (3.17) reduce to

$$\frac{E_s''}{E_s} = \frac{n\cos\alpha - \sqrt{n'^2 - n^2\sin^2\alpha}}{n\cos\alpha + \sqrt{n'^2 - n^2\sin^2\alpha}}, \tag{3.19}$$

$$\frac{E_p''}{E_p} = \frac{n'^2\cos\alpha - n\sqrt{n'^2 - n^2\sin^2\alpha}}{n'^2\cos\alpha + n\sqrt{n'^2 - n^2\sin^2\alpha}}. \tag{3.20}$$

For normal incidence, i.e. $\alpha = 0$, the reflectivity for the s-polarized and the p-polarized waves are the same according to Eqs. (3.16) and (3.17),

$$R_s = R_p = \left(\frac{E''}{E}\right)^2 = \left(\frac{n'\mu - n\mu'}{n'\mu + n\mu'}\right)^2. \tag{3.21}$$

If the electromagnetic wave is incident from vacuum to a nonmagnetic material, so $n = 1$ and $\mu = \mu' = 1$. In general, the index of refraction is complex, i.e. $n' = n_0 + ik$, which could account for the dielectric loss in the materials. Consequently, the complex reflective coefficient can be written as

$$\tilde{r} = \sqrt{R}\exp(i\phi), \tag{3.22}$$

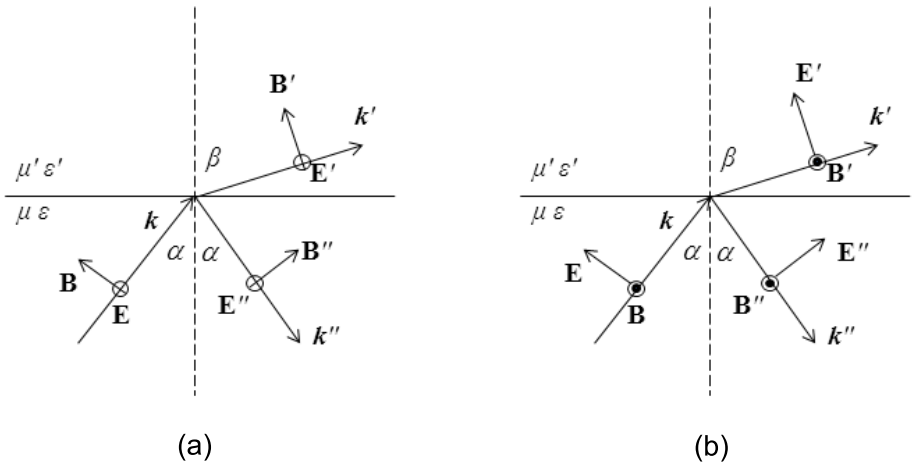

Figure 3.1: Reflection and refraction of electromagnetic wave at the interface between two media for (a) s-polarized and (b) p-polarized waves. The electric field **E**, magnetic field **B**, and propagation vector **k** of the reflected and refractive waves are denoted with prime and two primes, respectively. α and β are the incident and refractive angles.[49]

where the amplitude corresponds to the square root of the intensity ratio between the refractive and incident waves

$$R = \frac{(1-n_0)^2 + k^2}{(1+n_0)^2 + k^2}, \tag{3.23}$$

and the phase satisfies

$$\phi = \arctan\left(\frac{-2k}{1-n_0^2-k^2}\right). \tag{3.24}$$

In general, the reflective coefficient is a function of frequency. The real and imaginary parts of $\ln \tilde{r}(\omega)$ obey the Kramers-Kronig relation

$$\ln\sqrt{R(\omega)} = \frac{2}{\pi} P \int_0^\infty \frac{\omega' \phi(\omega')}{\omega'^2 - \omega^2} d\omega', \tag{3.25}$$

$$\phi(\omega) = -\frac{2\omega}{\pi} P \int_0^\infty \frac{\ln\sqrt{R(\omega')}}{\omega'^2 - \omega^2} d\omega', \tag{3.26}$$

where P is the Cauchy principle value of the integral. The Kramers-Kronig relation indicates that the amplitude and phase of the refractive coefficient are not independent, so according to Eqs. (3.23) and (3.24), the complex refractive index can be determined by measuring only the reflection in a broad frequency range.

3.2 Spectrometers

3.2.1 Sub-millimeter magneto-optic spectrometer

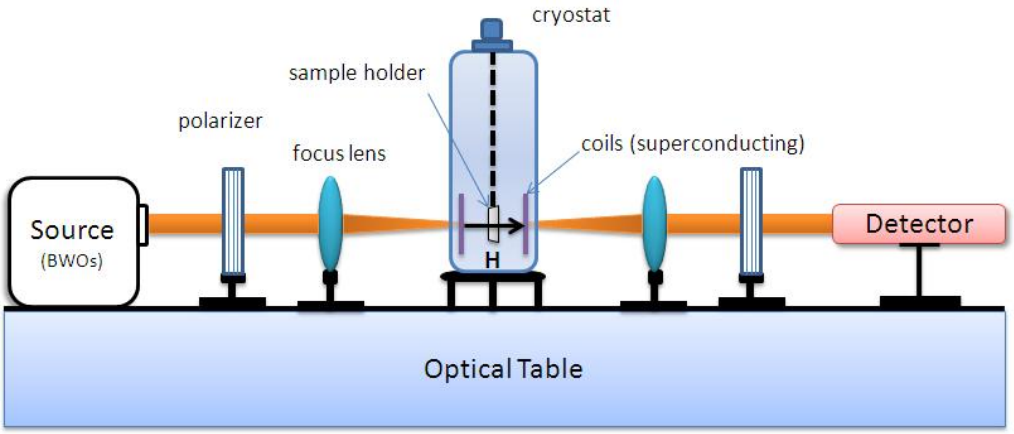

Figure 3.2: Sketch of submillimeter spectrometer. Transmission measurements with applied magnetic field along the propagation direction of terahertz electromagnetic wave (Faraday configuration) are illustrated.

Figure 3.2 schematically shows the setup of the submillimeter spectrometer that is used to perform the high-field electron-spin-resonance transmission measurements. Coherent submillimeter electromagnetic waves are generated by backward wave oscillators (BWOs). Each BWO covers a small specified frequency range. A total spectral range 0.060 - 1.400 terahertz can be covered by eight different BWOs.

The adopted cryostat is a commercial magneto-optic cryostat made by Oxford Instruments. A temperature range from room temperature down to 1.5 K can be reached. A superconducting coil cooled by liquid helium can generate a static magnetic field up to 7 T. Terahertz electromagnetic radiation can be detected by a Golay cell working at room temperature or by a highly sensitive Bolometer working at 4.2 K.

3.2.2 Terahertz time-domain spectrometer

Terahertz (THz) time-domain spectroscopy measurements are performed using a TPS-Spetra-3000 spectrometer from TeraView Ltd. The setup of the spectrometer is sketched in Figure 3.3. An optical cryostat covering the temperature range 4 - 300 K is equipped at the sample chamber for temperature dependent measurements, which is

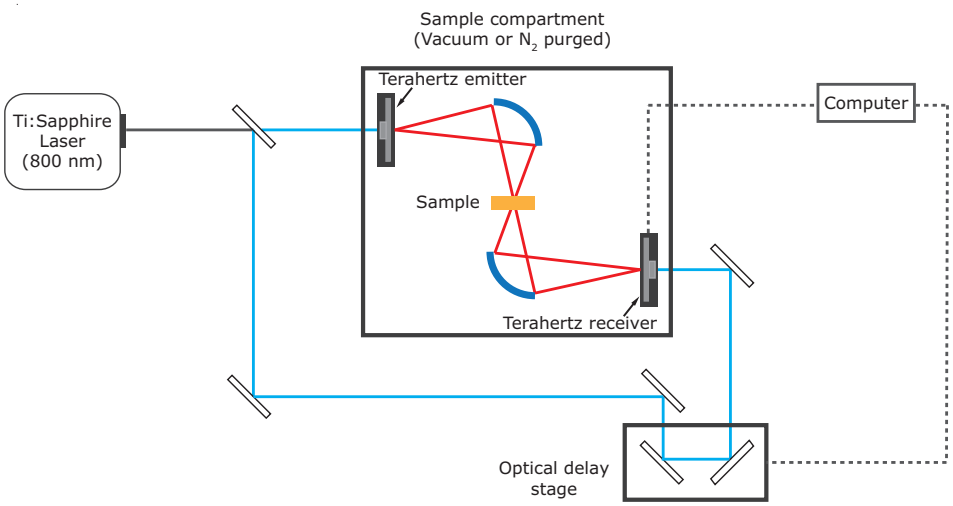

Figure 3.3: Sketch of the terahertz time-domain spectrometer TPS-Spectra 3000 from TeraView Ltd.

not included in this sketch. A Ti:Sapphire laser is used to provide near-infrared (NIR) pulse radiation with a wavelength of 800 nm. The beam is split into two beams by a semi-transparent lens. One of the beams is guided to a THz emitter, which generates a THz pulse due to the photoelectric effect. The THz pulse propagates through a sample and reaches a THz receiver. The receiver can only detect the THz pulse when the other NIR beam also reaches the receiver (gate detector). An optical delay on the NIR beam path can be introduced and adjusted by an optical delay stage. The measured quantity is the transmitted THz electric field strength as a function of time delay. Through Fourier transformation one can obtain the frequency dependence of the electric field strength and phase. By measuring the transmission of sample and reference, the dielectric functions can be calculated by solving Fresnel equations.

3.2.3 Fourier Transform Infrared Spectrometer

In this work, the Fourier Transform infrared (FTIR) spectrometers Bruker IFS 113V and IFS 66V/S spectrometers have been used. The spectrometers are mainly composed of a Michelson interferometer, the source, the beam splitter, the sample chamber and the detector, as illustrated in Figure 3.4 for the Bruker IFS 66V/S spectrometer. The whole infrared frequency range was covered from about 50 cm^{-1} to 18 000 cm^{-1} by changing sources and detectors.

The intensity of the infrared light from the source is a function of frequency ν, denoted as $I(\nu)$. After the modulation at the Michelson interferometer, the intensity

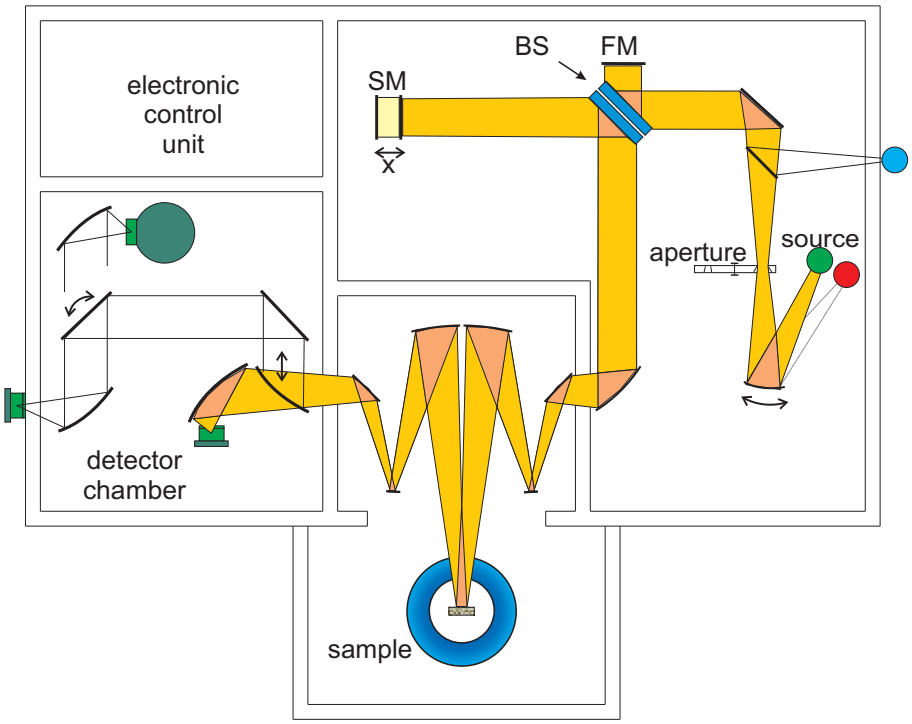

Figure 3.4: Scheme of Bruker IFS 66V/S FTIR spectrometer. The beam from the source is split into two beams by the beam splitter (BS). One beam propagates to the fix mirror (FM), the other propagates to the sliding mirror (SM).

of the outcoming light then is also a function of the difference in the optical path x, termed as $I(\nu, x)$, which satisfies $I(\nu, x) = I(\nu)[1 + \cos(2\pi\nu x)]$. The overall detected intensity corresponds to

$$I(x) = \int_0^\infty I(\nu)[1 + \cos(2\pi\nu x)]d\nu. \tag{3.27}$$

The first term on the right hand side is independent on x, while the second term purely results from interference. By performing a Fourier transformation, $I(\nu)$ can be obtained. Reflection is measured with normal incident configuration. A gold mirror is used as a reference to determine the reflectivity of the sample.

4 Magnetic Excitation and Magnetic Anisotropy in Spin Dimer Systems

Spin singlet-triplet excitations are usually not allowed through Zeeman coupling of the spins to the ac magnetic field of the electromagnetic wave, because the total spin angular momentum is conserved for Heisenberg interactions. Magnetic anisotropy can violate the total spin conservation, thus spin singlet-triplet excitations can be induced by Zeeman coupling. Such excitations may also result from indirect processes, where spin-phonon coupling plays a key role.[30, 85] High-field electron spin resonance studies on magnetic excitations and magnetic anisotropy in the spin-dimer systems will be presented in this chapter.

4.1 Static Dzyaloshinskii-Moriya interaction in $CuTe_2O_5$

4.1.1 Crystalline and magnetic structure

As shown in Fig. 4.1, $CuTe_2O_5$ exhibits a monoclinic structure with space group $P2_1/c$ and lattice parameters $a = 6.817$ Å, $b = 9.322$ Å, $c = 7.602$ Å, and $\beta = 109.08°$.[43] There are four Cu ions in the unit cell. Each Cu ion is surrounded by six oxygen atoms forming a strongly distorted octahedron. Two edge-sharing neighboring octahedra along the c axis form a structural dimer unit Cu_2O_{10}. The dimer units are separated by Te-O bridging ligands.

The high-temperature magnetic susceptibility of $CuTe_2O_5$ can be fitted by a Curie-Weiss law with a Curie-Weiss temperature of $\Theta = -41$ K.[64] At $T = 56.6$ K the susceptibility shows a maximum followed by a strong decrease to lower temperatures,[64] which is typical for magnetic dimer systems, see Sec. 2.1.3.[14] However, the magnetic susceptibility cannot be well fitted by a model of isolated magnetic dimers.[27] Moreover, the isolated dimer model also faces difficulties in explaining the results of electron spin resonance.

The extended Hückel tight-binding (EHTB) method has been used to investigate the possible exchange paths, see Table 4.1.[27] It has been shown that the exchange interaction between the sixth-nearest-neighboring Cu ions by a single O-Te-O bridge (J_6) is strongest and the nearest-neighboring interaction within the structural dimer (J_1) is the second strongest, while other exchange paths lead to much smaller exchange interactions between the Cu ions (see Fig. 4.1 for exchange paths). In contrast

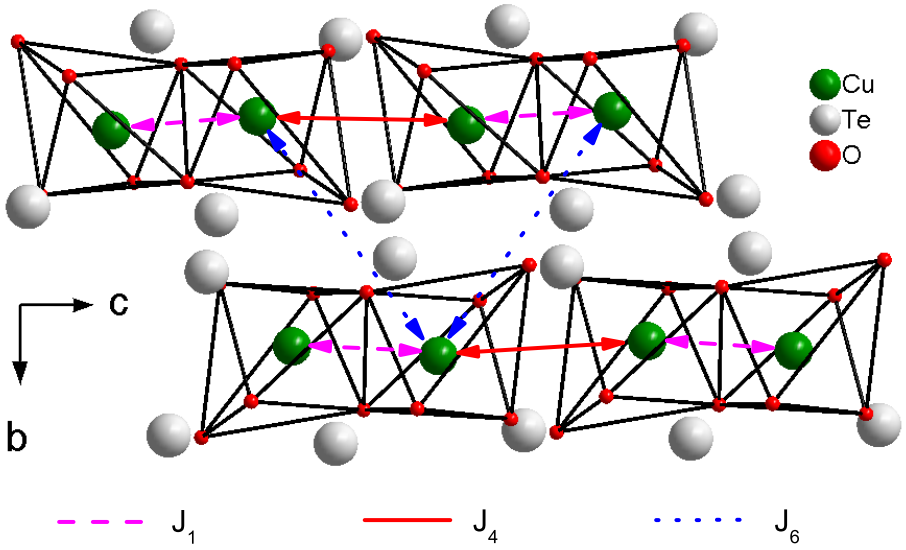

Figure 4.1: Crystal structure of $CuTe_2O_5$ with space group $P2_1/c$. Structural dimers consisting of edge-sharing octahedra Cu_2O_{10} are separated by Te ions. J_1, J_4, and J_6 are the exchange interactions between the first-, fourth-, and sixth-nearest-neighboring Cu ions, respectively.[97]

to the results of EHTB, *ab initio* density-functional theory (DFT) calculations within the local-density approximation (LDA) claimed that the strongest exchange interaction is between the fourth-nearest-neighboring Cu ions by two O-Te-O bridges (J_4, see Fig. 4.1) with the second and third strongest being J_6 and J_1, respectively,[26] indicating that $CuTe_2O_5$ is a two-dimensional coupled spin-dimer system. Direct computation of exchange constants by an LDA+U approach qualitatively showed a similar result (see Table 4.1),[93] but determined a smaller value of the leading exchange constant $J_4 = 5.5$ meV ($\sim$ 64 K) than the value of $J_4 = 7.96$ meV ($\sim$ 92.4 K) obtained by quantum Monte Carlo (QMC) simulations of the magnetic susceptibility.[26]

In the following, we will present the results of high-field electron spin resonance transmission spectroscopy up to 1.4 THz in $CuTe_2O_5$. A spin singlet-to-triplet excitation of 4.94 meV has been resolved, which is considerably smaller than the strongest exchange interaction obtained by mean-field approximation[27] or QMC.[26]

Table 4.1: Exchange interactions J_1, J_4, and J_6 obtained from the extended Hückel tight-binding (EHTB) electronic structure calculations [27], *ab initio* density-functional theory calculations within the local-density approximation (LDA) [26], and LDA+U calculations [93]. The largest exchange constant is set as unity for EHTB and LDA results and the ratios of exchange constants are presented. See Fig. 4.1 for the exchange paths.

Exchange constants J_i	Cu-Cu distances Å	EHTB J_i/J_6	LDA J_i/J_4	LDA+U $U = 8eV$ meV (J_i/J_4)	LDA+U $U = 10eV$ meV (J_i/J_4)
J_1	3.187	0.59	0.12	0.43 (0.08)	0.26 (0.08)
J_4	5.585	0.11	1.00	5.50 (1.00)	3.70 (1.00)
J_6	6.202	1.00	0.28	1.63 (0.30)	1.12 (0.31)

4.1.2 Spin dimer excitation spectra

Figures 4.2(a)-(f) show electron spin resonance transmission spectra of $CuTe_2O_5$ as a function of magnetic field measured at different frequencies with $\mathbf{H} \parallel a^*$ or $\mathbf{H} \perp a^*$, where a^* denotes the direction perpendicular to the bc-plane. Absorptions can be clearly observed in these spectra as marked by the arrows. The following features can be directly extracted from the data:

(i) *Energy scale.* The absorptions shown in Fig. 4.2(a)-(d) are obtained at the high-frequency range ($f > 1$ THz) with relatively small fields ($H < 5.2$ T). In contrast, the absorptions in Figs 4.2(e) and (f) have much lower frequencies ($f \leq 200$ GHz) and high fields ($H > 5.6$ T). As suggested by the magnetic susceptibility and LDA+U calculations,[64, 27, 26, 93] the leading antiferromagnetic interaction J_4 should not be smaller than 3.7 meV (~ 0.9 THz), while the Zeeman energy at 7 T is about 0.85 meV (~ 206 GHz) assuming a g-factor of 2.1.[27] The Zeeman energy is comparable with that of the absorption modes in Figs 4.2(e) and (f). Therefore, we can distinguish the intra-triplet mode 2 in Figs 4.2(e) and (f) from the singlet-triplet modes 1 and 3 in Figs 4.2(a)-(d).

(ii) *Field dependence.* The resonance fields in Figs 4.2(e) and (f) shift to larger values with higher photon frequency confirming the assignment of mode 2. A similar frequency dependence found in Figs 4.2(c) and (d) enables us to assign mode 3, while the reverse situation in Figs 4.2(a) and (b) represents a feature of mode 1.

(iii) *Orientation dependence.* The resonance field obtained at 200 GHz with $\mathbf{H} \perp a^*$ [Fig. 4.2(e)] significantly differs from that measured at 199.84 GHz with $\mathbf{H} \parallel a^*$ [Fig. 4.2(f)]. Since the frequencies are almost the same, the large shift of resonance field with the variation of field orientation can be ascribed to the anisotropy of the

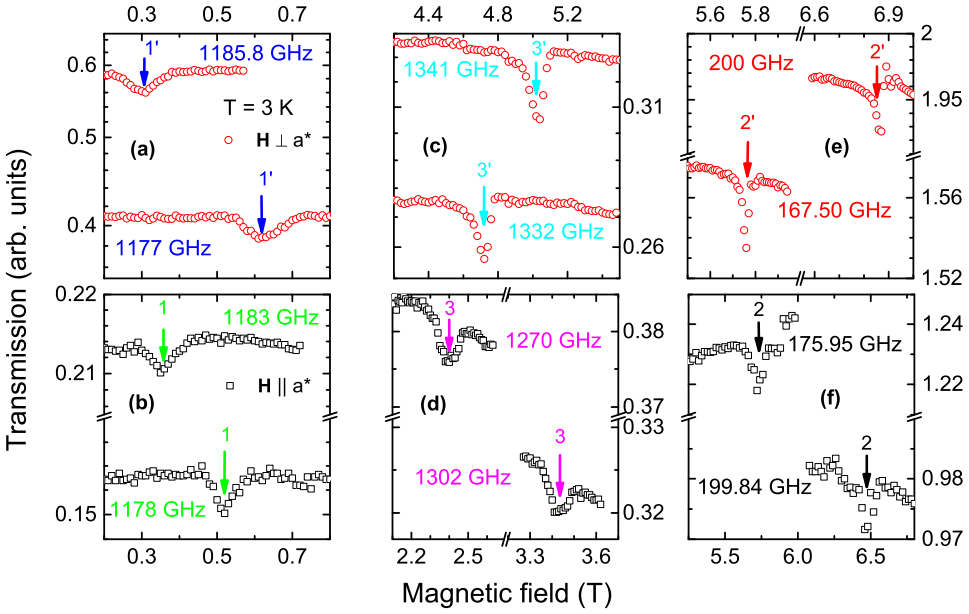

Figure 4.2: Transmission spectra measured at 3 K as a function of **H** at various frequencies corresponding to modes 1, 3, and 2 for **H** $\parallel$ a^*, and mode 1', 3', and 2' for **H** $\perp$ a^*.[97] Modes 1(1') and 3(3') are spin singlet-triplet excitations; Modes 2(2') are intra-triplet excitations; see Fig. 2.3 for the energy scheme of a spin-dimer system.

g-factor as explained in the following. A similar feature can be observed by comparing absorption lines measured with different orientations of applied field in Figs 4.2(a) and (b).

According to these features, the ESR modes can be unambiguously identified as mode 1, 2, or 3 for **H** $\parallel$ a^*, and mode 1', 2', or 3' for **H** $\perp$ a^*, as marked by arrows in Figs 4.2(a)-(f).

4.1.3 Discussion

The photon frequencies, at which absorption lines were observed, are summarized as a function of the corresponding resonance fields in Fig. 4.3 for **H** $\parallel$ a^* and **H** $\perp$ a^*. The observed modes differ for the two orientations of magnetic field. The intra-triplet excitations, modes 2 and 2', are fitted by lines through the origin, resulting in the effective g-factors $g_{a^*} = 2.19(1)$ and $g_{bc} = 2.08(1)$ for **H** $\parallel$ a^* and **H** $\perp$ a^*, respectively. The g-factors are consistent with the values $g_{a^*} = 2.27(2)$, and $g_{bc} = 2.11(3)$ obtained from X- and Q-band ESR, from which a nearly constant g-factor in the bc-plane was

also demonstrated.[27] Modes 1(1') and 3(3') can be described in terms of a linear Zeeman splitting following $h\nu = h\nu_0 \mp g\mu_B H$ with $g_{a^*} = 2.16 \pm 0.03$ ($g_{bc} = 2.11 \pm 0.01$) and $g_{a^*} = 2.21 \pm 0.01$ ($g_{bc} = 2.08 \pm 0.01$), respectively, and a coincident zero-field value of $\nu_0 = 1.194(2)$ THz (~ 4.94 meV). These g-factors, slightly larger than the spin-only value of $g \sim 2$, are typical for the $3d^9$ electron configuration of Cu^{2+} in distorted oxygen octahedra, where the orbital momentum is nearly quenched by the crystal field.[2]

Both LDA and EHTB calculations have revealed that the important exchange paths in $CuTe_2O_5$ are lying in the layers parallel to the *bc*-plane, and the inter-layer exchange interactions between the Cu ions are much smaller and can be neglected. Therefore, we consider a Hamiltonian following the work by Leuenberger *et al.*[65]

$$\mathcal{H} = \sum_i J_4 \vec{S}_{i1} \cdot \vec{S}_{i2} + \sum_{(i,j')} J_6 \vec{S}_{i1} \cdot \vec{S}_{j'2} + \sum_{[i,j]} J_1 \vec{S}_{i1} \cdot \vec{S}_{j2}, \tag{4.1}$$

by taking into account only the three leading intra-layer interactions J_4, J_6, and J_1, where i numerates the magnetic dimers (the subscripts *1* and *2* designate the two Cu ions in one dimer), (i, j') denotes the pairs of neighboring magnetic dimers correlated by J_6, and $[i, j]$ counts the pairs of magnetic dimers correlated by J_1 (see Fig. 4.1).

Using the standard-basis operator method within the random phase approximation, [42] which has been applied to study the dispersion relation in several coupled magnetic dimer systems, such as $Cs_3Cr_2Br_9$,[65] $BaCuSi_2O_6$,[83] $Ba_3Cr_2O_8$,[57] and $Sr_3Cr_2O_8$,[99, 76] the energy corresponding to the singlet-to-triplet excitation at the Γ point ($\mathbf{Q} \simeq \mathbf{0}$) can be approximated by $h\nu_0 \simeq \sqrt{J_4^2 + J_4\gamma}$, where $\gamma = -2J_1 + 4J_6$. According to the LDA+U calculations,[93] the value of $h\nu_0$ =5.32 meV determined for $U = 10$ eV is close to the experimental result of 4.94 meV, while $h\nu_0$ =7.83 meV, which has been determined for $U = 8$ eV, would underestimate the on-site Coulomb repulsion in $CuTe_2O_5$. It is worth noting that only the first-order perturbation of γ/J_4 is considered here, although the ratio $J_6/J_4 \sim 0.3$ given by the LDA+U calculation is not much smaller than 1.

Extrapolation of the linear field dependence of the mode 1 and 1' to high magnetic field is shown on the left coordinate in Fig. 4.4. The singlet-triplet gaps are expected to be closed in the magnetic field of 38.9(4) T and 40.7(4) T determined by $H_{c1} = h\nu_0/g\mu_B$ from mode 1 and 1' with g_{a^*} and g_{bc}, respectively. For comparison, the high-field magnetization measured in the Dresden High Magnetic Field Laboratory up to 60 T is shown on the right coordinate in Fig. 4.4. A clear increase of magnetization can be observed at $H_{c1}^{a^*} = 37.6$ T for $\mathbf{H} \parallel a^*$ and at $H_{c1}^{bc} = 40.6$ T for $\mathbf{H} \perp a^*$. The onset of finite magnetization occurs when the gap minimum is closed by the external magnetic field. The gap minimum is in general not necessarily located at the Brillouin zone center Γ point, but the agreement between optical and magnetization measurements indicates that the spin gap at the Γ point is close to the minimum gap.

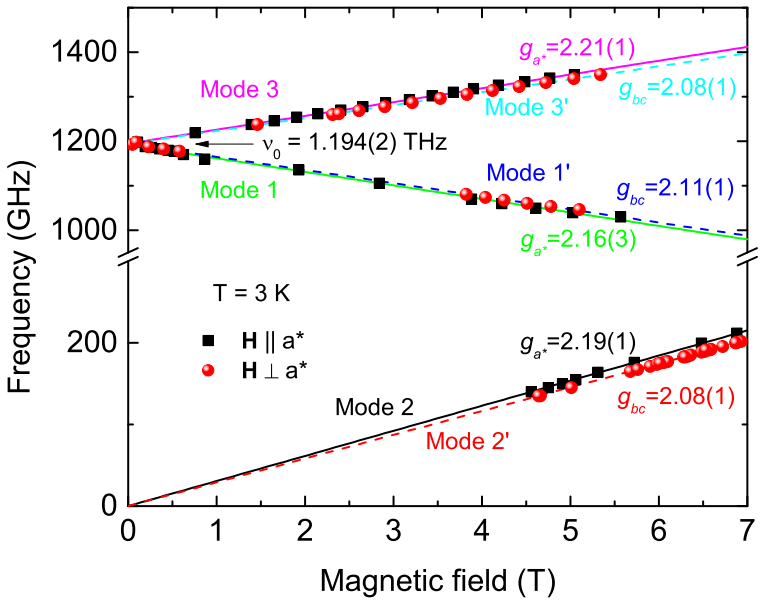

Figure 4.3: Resonance frequencies of the observed absorption lines at 3 K as a function of applied magnetic field, for the field parallel and perpendicular to a^*.[97] The lines are calculated with g values indicated. Different modes are shown by different colors.

If there is only an isotropic intra-dimer exchange, the singlet-triplet excitations in a magnetic dimer cannot be observed in ESR spectra (see Sec. 2.1.4). When a magnetic anisotropy via Dzyaloshinskii-Moriya interaction $\vec{D} \cdot (\vec{S}_i \times \vec{S}_j)$ is present, the spin-triplet states are split even in zero field. Moreover, the local triplet and singlet state will mix and allow to detect singlet-triplet transitions.[78] The singlet-triplet excitation modes 1 and 3 observed in the Faraday configuration ($\mathbf{H} \parallel a^*$) indicate a mixing of the singlet $|0,0\rangle$ and the triplet state $|1,0\rangle$ due to a Dzyaloshinskii-Moriya vector $\vec{D}$ $\parallel \mathbf{H} \parallel a^*$ (see Sec. 2.1.6). For the Voigt configuration ($\mathbf{H} \perp a^*$), the Dzyaloshinskii-Moriya interaction with $\vec{D} \parallel a^* \perp \mathbf{H}$ would mix $|0,0\rangle$ with $|1,\pm1\rangle$, thus the singlet-triplet excitations are also possible in this configuration, which complies with the observation of mode 1' and 3'.[78, 67] Therefore, we conclude that the Dzyaloshinskii-Moriya vector is perpendicular to the crystalline bc-plane. Based on the reported $P2_1/c$ monoclinic structure, the exchange path of the dominant exchange J_4 possesses an inversion symmetry at the bond center. Therefore, a lower structure symmetry

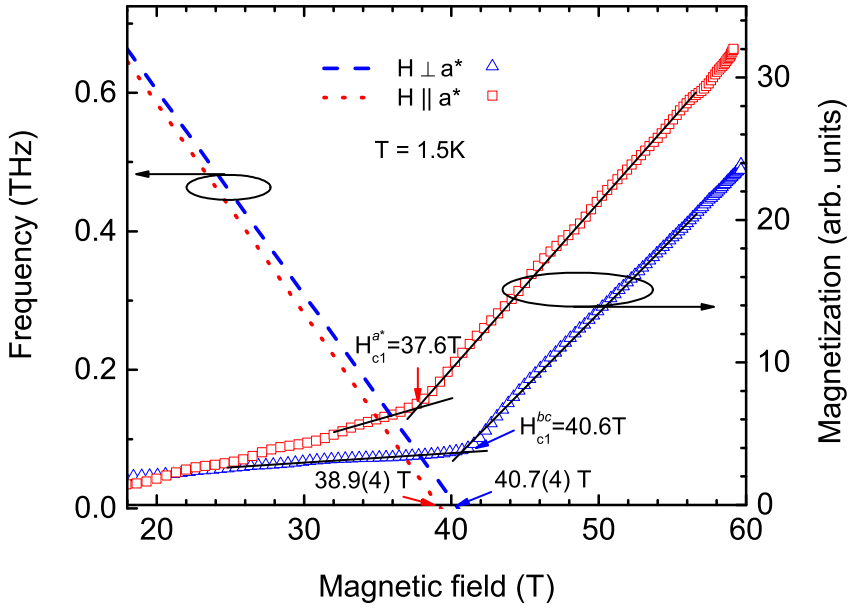

Figure 4.4: Left coordinate: Extrapolation of mode 1 ($\mathbf{H} \parallel a^*$, dotted line) and mode 1' ($\mathbf{H} \perp a^*$, dashed line) to the high magnetic field region. Right coordinate: Magnetization measured in a 60 T pulsed magnet at 1.5 K as a function of magnetic field for $\mathbf{H} \parallel a^*$ and for $\mathbf{H} \perp a^*$. Solid lines are guides for the eyes.[97] High-field magnetization was measured in the Dresden High Magnetic Field Laboratory by Yurii Skourski.

without inversion center, e.g. $P2_1$, is expected in $CuTe_2O_5$ in the scenario of a static Dzyaloshinskii-Moriya mechanism.

4.2 Dynamical Dzyaloshinskii-Moriya interaction in $Sr_3Cr_2O_8$ and $Ba_3Cr_2O_8$

4.2.1 Crystalline and magnetic structure

At room temperature the isostructural compounds $Sr_3Cr_2O_8$ and $Ba_3Cr_2O_8$ crystalize in an hexagonal structure with space group $R\bar{3}m$, shown in Fig. 4.5(a).[25] In the unit cell, each Cr^{5+} ion with a single $3d$ electron and spin 1/2 is surrounded by an oxygen tetrahedron. Along the c direction, two adjacent Cr-O tetrahedra form a structural

dimer. The *ABCABC* type stacking of structural dimers are illustrated in Fig. 4.5(b). The tetrahedral crystal field splits the $3d$ levels into lower-lying doubly-degenerated e and higher-lying triply-degenerated t orbitals. Thus, in this environment the Cr^{5+} ion is Jahn-Teller active and a Jahn-Teller transition to a monoclinic structure with space group $C2/c$ has been reported by neutron powder diffraction to occur at 275 K and 70 K for $Sr_3Cr_2O_8$ and $Ba_3Cr_2O_8$, respectively.[23, 57]

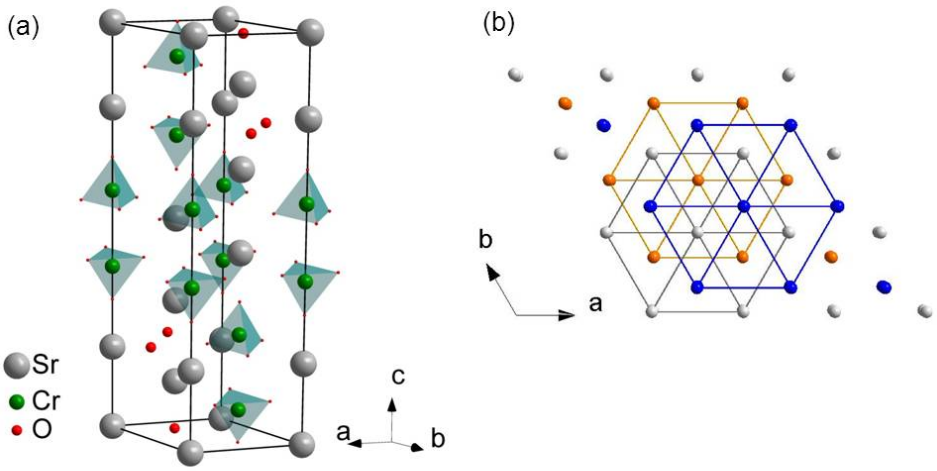

Figure 4.5: (a) Unit cell of $Sr_3Cr_2O_8$ in the high-temperature hexagonal structure with the space group $R\bar{3}m$. (b) Three-layer *ABCABC* structure of Cr dimers. Cr dimers from the layers A, B, and C are distinguished by colors of white, blue, and orange, respectively.

The structural transition is accompanied by an antiferro-distortive displacement of the apical oxygens from the two tetrahedra of the dimer. The local symmetry C_{3v} at the Cr site is reduced to C_s. An antiferro-orbital ordering is formed due to the splitting of the e doublet into the lower-lying $d_{3z^2-r^2}$ and excited $d_{x^2-y^2}$ orbital, see Fig. 4.6.[23, 57] Figure 4.7(a) shows the unit cell of the low-temperature monoclinic structure. In the unit cell there are only two layers of Cr dimers stacked in an *ABAB* manner. The structural phase transition changes the magnetic exchange paths and leads to spatially anisotropic exchange couplings, shown in Fig. 4.7(b).[23, 76]

The exchange interaction within the structural dimer is the largest, so the structural dimer is also a spin dimer. Spin dimerization occurs below $T_{dim} = 70$ K in $Sr_3Cr_2O_8$ and 16 K in $Ba_3Cr_2O_8$, which is reflected by temperature dependent magnetic susceptibilities showing broad maxima at the corresponding temperatures (see Fig. 2.2).[87, 4] The decrease of the magnetic susceptibility at low temperatures reflects the fact that the magnetic ground state is a spin-singlet, while the excited state

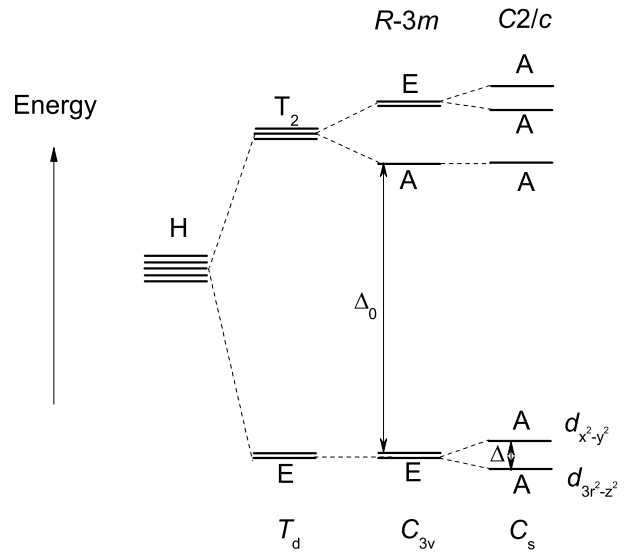

Figure 4.6: Crystal-field splitting of the Cr $3d$ orbitals. Five-fold degenerate $3d$ atomic orbitals are split into a T_2 orbital triplet and an E orbital doublet in a regular tetragonal crystal field (T_d). The triplet is split into a higher-lying E doublet and an A singlet, corresponding to the local symmetry C_{3v} at the Cr site in the high temperature $R\bar{3}m$ phase. The orbital degeneracy is completely removed in the low temperature $C2/c$ phase stabilizing the $d_{3z^2-r^2}$ orbital.[23]

is a gapped spin-triplet. The intra-dimer exchange interaction is of antiferromagnetic type.[47, 4] A Bose-Einstein condensate of magnons can be reached in high magnetic field in a temperature range up to 8 K in $Sr_3Cr_2O_8$ and 2.7 K in $Ba_3Cr_2O_8$.[6, 5]

The lattice constants and exchange interactions of both compounds are summarized in Table 4.2. Since Ba ion is larger than Sr ion, $Ba_3Cr_2O_8$ has larger lattice constants than $Sr_3Cr_2O_8$ both in the high- and low-temperature phase. Thus the exchange paths in $Sr_3Cr_2O_8$ are shorter than in $Ba_3Cr_2O_8$, and the exchange interactions are stronger in $Sr_3Cr_2O_8$ as expected. Consequently, the critical magnetic fields for magnon condensation are larger in $Sr_3Cr_2O_8$.

Spin singlet-triplet transitions have been investigated by the inelastic neutron scattering experiments in $Sr_3Cr_2O_8$ [76] and in $Ba_3Cr_2O_8$ [57]. As shown in Fig. 2.4, three different dispersion relations of the spin singlet-triplet excitations have been observed in $Sr_3Cr_2O_8$.[76] The different dispersions are ascribed to the existence of three monoclinic crystallographic twins. Each dispersion has a finite bandwidth, indicating that the magnons can propagate from one dimer to the neighboring dimers due to

Table 4.2: Characteristic parameters of structural properties, magnetic properties, and magnon condensation in $Sr_3Cr_2O_8$ and $Ba_3Cr_2O_8$. Some of the available parameters in $CuTe_2O_5$ are summarized for comparison. The exchange interactions of $Sr_3Cr_2O_8$ and $Ba_3Cr_2O_8$ are obtained from experiments[76, 57] with exchange paths shown in Fig. 4.7. The values in $CuTe_2O_5$ have been determined by LDA+U calculation for $U = 10$ meV,[93] which is consistent with experimental results.[99] J_0 is the intra-dimer exchange interaction, and J' is effective interdimer exchange interaction.

	$Sr_3Cr_2O_8$	$Ba_3Cr_2O_8$	$CuTe_2O_5$
Structural transition			
T_{JT}	285 K	70 K	
Hexagonal lattice constant (Å)	[76]	[57]	[43]
a_h	5.57	5.72	
c_h	20.17	21.38	
Monoclinic lattice constant (Å)	$C2/c$	$C2/c$	$P2_1c$
a_m	9.66	9.90	6.87
b_m	5.54	5.72	9.32
c_m	13.79	14.63	7.60
β	103.66°	103.12°	109.08°
Exchange interactions (meV)			
J_0	5.55	2.38	3.7
J'_1	-0.04	-0.15	
J''_1	0.25	0.09(1)	
$J'_2 - J'_3$	0.75	0.10	
$J''_2 - J''_3$	-0.54	-0.52	
$J'''_2 - J'''_3$	-0.12	0.07	
J'_4	0.06	0.09(1)	
J''_4	-0.05	0.04	
J'/J_0	0.64	0.82	0.3
Magnon condensation			
T_{max}	8 K	2.7 K	
H_{c1}	30.4 T	12.5 T	40(1) T
H_{c2}	62 T	23.6 T	

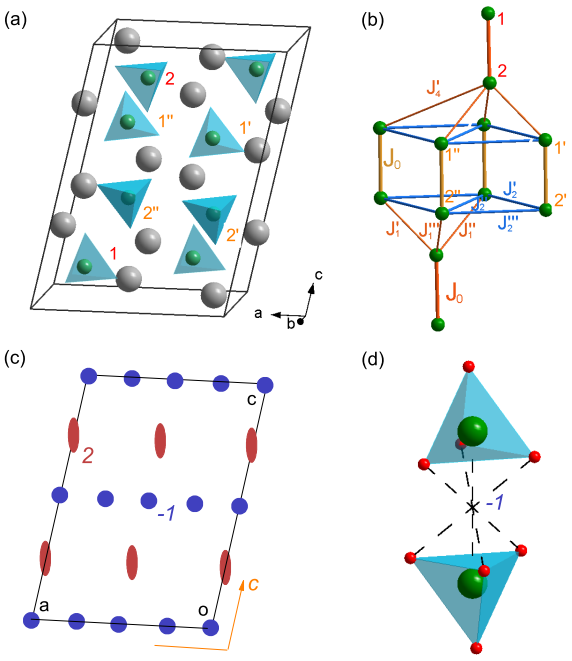

Figure 4.7: (a) Unit cell of $Sr_3Cr_2O_8$ in the low-temperature monoclinic phase with space group *C2/c*. (b) Spin-dimer structure with anisotropic exchange interactions following Ref. [76]. J_0 is the intra-dimer exchange interaction. (c) Symmetry elements of the space group *C2/c*: inversion center -1, two-fold rotation *2*, and glide plane *c* marked in the crystalline *ac*-plane.[1] (d) The Cr^{5+} spin dimer composed of two Cr-O tetrahedra with local inversion center -1 in $Sr_3Cr_2O_8$. Green, red, and gray spheres denote Cr, O, and Sr ions, respectively.[94]

interdimer exchange interaction. These features are also observed in $Ba_3Cr_2O_8$.[57] The geometrical relations between the monoclinic and the hexagonal lattice vectors are given in Table 4.3 and are illustrated in Fig. 4.8.

4.2.2 Spin dimer excitation spectra

Figure 4.9(a) shows the ESR transmission spectra of unpolarized monochromatic THz electromagnetic waves at various frequencies in $Sr_3Cr_2O_8$. Resonance absorptions can be observed at certain magnetic fields. The frequencies and corresponding fields are shown in the frequency-field diagram in Fig. 4.9(b). One can clearly recognize four modes: three gapped modes 1, 1', and 3' and one gapless mode 2. The linear field

Table 4.3: Geometrical relations between the hexagonal (h) and the monoclinic (m) lattice vectors of three crystallographic twins, see also Fig. 4.8.[76]

	Twin1	Twin2	Twin3
$a_h =$	$(a_{m1} + b_{m1})/2$	$(a_{m2} - b_{m2})/2$	$-b_{m3}$
$b_h =$	$(-a_{m1} + b_{m1})/2$	b_{m2}	$(a_{m3} + b_{m3})/2$
$c_h =$	$(-a_{m1} + 3c_{m1})/2$	$(-a_{m2} + 3c_{m2})/2$	$(-a_{m3} + 3c_{m3})/2$

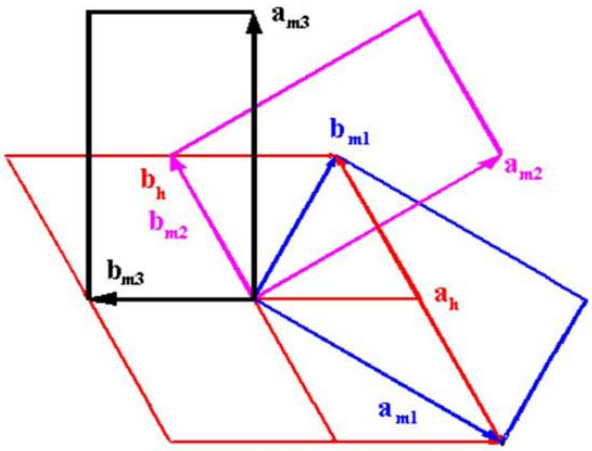

Figure 4.8: Illustration of geometrical relations between the hexagonal lattice vectors a_h and b_h and the monoclinic lattice vectors $a_{m1,m2,m3}$ and $b_{m1,m2,m3}$, see also Table 4.3. Taken from Ref. [76]

dependence of these modes can be described by $h\nu = h\nu_0 + g\mu_B H$ for modes 2 and 3' and $h\nu = h\nu_0 - g\mu_B H$ for modes 1' and 3 with $\nu_0^{opt} = 1.24$ THz $\cong 5.13$ meV for mode 1' and 3', $\nu_0^{aco} = 1.47$ THz$\cong 6.08$ meV for mode 3, $\nu_0 = 0$ for mode 2, and an effective g-factor of about 1.92(3). The linear fits are shown by solid lines in Fig. 4.9(b). The gapless mode 2 corresponds to the intra-triplet excitations, while the three gapped modes corresponds to the singlet-triplet excitations.

Due to the existence of three monoclinic twins in the low temperature phase, it is impossible to measure the polarized spectra with respect to the monoclinic axes. Since the hexagonal axes a_h and b_h both have the monoclinic a_m and b_m components, it is equivalent to apply the electric (or magnetic) field along the a_h or along the b_h in polarization measurements at low temperatures. Polarized ESR transmission spectra of $Sr_3Cr_2O_8$ are measured with respect to the hexagonal axes systematically

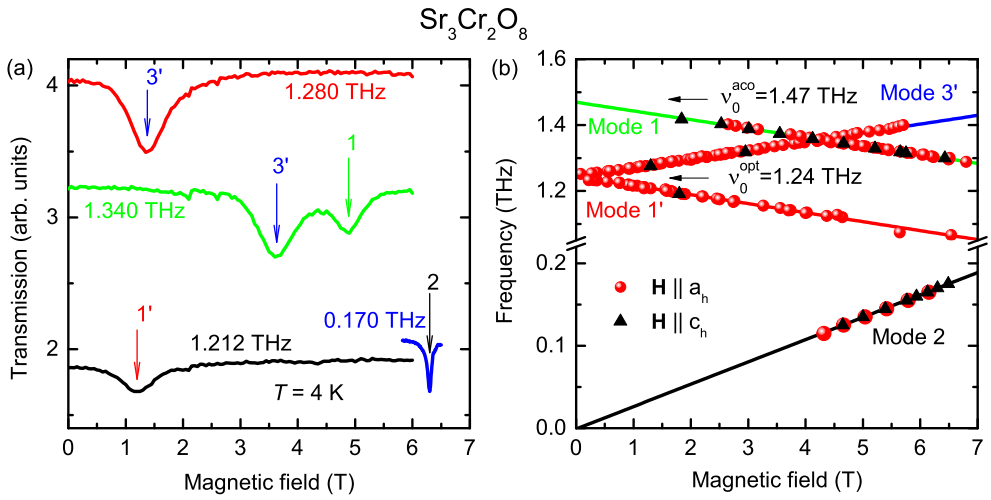

Figure 4.9: (a) Transmission spectra measured in an applied magnetic field H at different frequencies at $T = 4$ K in $Sr_3Cr_2O_8$. The spectrum at 0.170 THz is obtained with $H \parallel a_h$, the other spectra are measured with $H \parallel c_h$. Mode 2 is the intra-triplet mode. Modes 1, 1', and 3 are singlet-triplet modes. (b) Magnetic-field dependence of the observed absorption frequencies at 4 K for $H \parallel c_h$ and $H \parallel a_h$.[94]

and are shown in Figs 4.10(a)-(d). In accord with the results from the unpolarized measurements shown in Fig. 4.9(b), the gapped modes 1 and 3' can be determined in Figs 4.10(a)-(c), while only the mode 1 can be observed in in Fig. 4.10(d). These observations are summarized in Table 4.4.

4.2.3 Discussion

Acoustic and optical singlet-triplet excitations

Due to the double-layer structure of the Cr spin dimers, the triplet excitations have two branches, *i.e.*, an acoustic (in-phase) mode ω^+ and an optical (anti-phase) mode ω^-, corresponding to the "$q = 0$" and "$q = \pi$" phase difference between spin dimers of adjacent layers, respectively.[42, 65] The excitation energies at the zone center are given by a random phase approximation[57, 76]

$$\omega^{\pm} = \sqrt{J_0^2 + J_0\gamma^{\pm}} \tag{4.2}$$

where $\gamma^{\pm} = 2(J_2' + J_2'' + J_2''') \pm [(J_1' + J_1'' + J_1''') + (J_4' + J_4'' + J_4''')]$. The different exchange constants J_is denote intra- and inter-layer interactions as illustrated in Fig. 4.7(b).

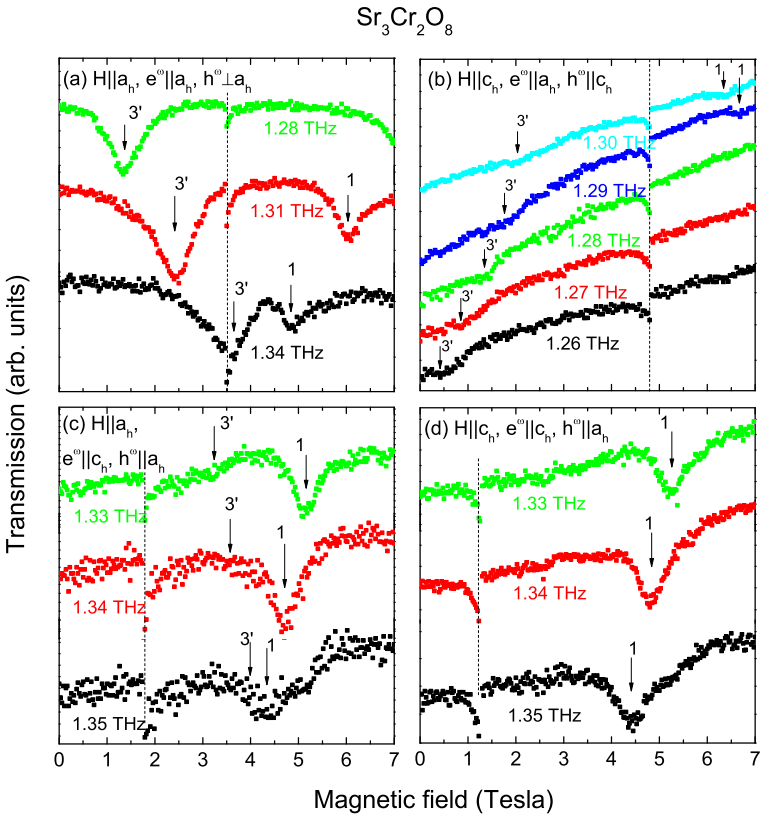

Figure 4.10: The ESR spectra of singlet-triplet excitations in $Sr_3Cr_2O_8$, measured with different polarizations (e^ω, h^ω) for different orientations of the applied magnetic field H with respect to the hexagonal axes at 2 K. The vertical dashed lines indicate artifacts due to spark lines from the BWOs.[94]

Based on the J_is determined from the inelastic neutron scattering experiments [76], the acoustic and optical modes can be estimated as $h\nu_0^{opt} = 5.14$ meV and $h\nu_0^{aco} = 5.92$ meV in good agreement with the ESR results in $Sr_3Cr_2O_8$. ESR transmission spectra have also been measured in $Ba_3Cr_2O_8$ by D. Kamenskyi et al. in the Dresden High Magnetic Field Laboratory.[51] Their results are summarized in Fig. 4.11(a), (c) and (d). The acoustic and optical modes are observed at $\omega^+ = 563$ GHz (2.3 meV) and $\omega^- = 399$ GHz (1.6 meV) in zero field for $Ba_3Cr_2O_8$ with $g = 1.94(3)$, also consistent with the neutron results 2.2, and 1.8 meV, respectively.[57, 58] The results of polarization measurements in $Ba_3Cr_2O_8$ is also summarized in Table 4.4.

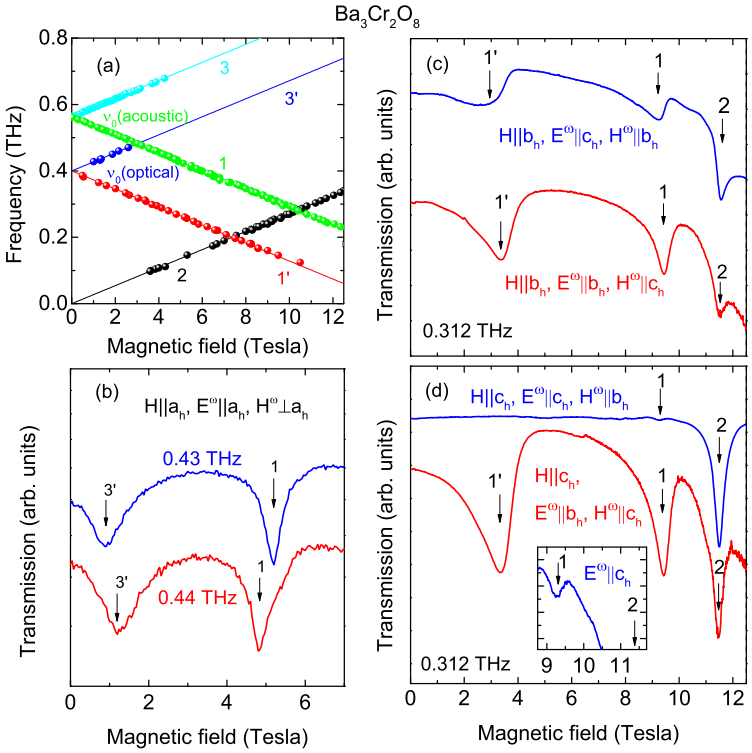

Figure 4.11: (a) Frequency-field diagram of the singlet-triplet excitations in $Ba_3Cr_2O_8$.[51] (b)-(d) Polarized ESR transmission spectra of singlet-triplet excitations in $Ba_3Cr_2O_8$ measured at 2 K. Inset: enlarged view of the spectrum for $H\|c_h$, $e^\omega\|c_h$, and $h^\omega\|b_h$.[94] (a)(c)(d) were measured by D. Kamenskyi et al. in the Dresden High Magnetic Field Laboratory.[51]

Polarization analysis

In Table 4.4 the acoustic and optical modes are denoted by '0' and 'π', respectively, . $Sr_3Cr_2O_8$ and $Ba_3Cr_2O_8$ exhibit the same selection rules, since the a_h and b_h axes are equivalent. The most important observation is that the optical mode is absent only for $e^\omega\|c_h$, $H\|c_h$, while acoustic modes are observed for all the polarizations.

A magnetic dipole singlet-triplet excitation in a single dimer can be observed when there is an intra-dimer static Dzyaloshinskii-Moriya interaction. This is forbidden in $Sr_3Cr_2O_8$ and $Ba_3Cr_2O_8$ due to the inversion center in the middle of the bonds in the Cr_2O_8 dimers [Fig. 4.7(d)]. If we restrict to a magnetic dipole mechanism, the weaker dimer-dimer interactions should be considered additionally to explain the observations. Static inter-dimer Dzyaloshinskii-Moriya interactions along the superexchange

Table 4.4: *Experimentally* observed spin singlet-triplet excitations in the polarized ESR spectra in the *hexagonal* notations for $Sr_3Cr_2O_8$ (Fig. 4.10) and for $Ba_3Cr_2O_8$ (Fig. 4.11). The acoustic mode 1 and optical mode $1'$, $3'$ are noted as '0' and 'π', respectively, for short. e^ω denotes the ac electric field and H denotes the applied magnetic field.

$e^\omega \backslash H$	a_h	b_h	c_h
a_h	$0+\pi$		$0+\pi$
	[Fig. 4.10(c), 4.11(b)]		[Fig. 4.10(d)]
b_h		$0+\pi$	$0+\pi$
		[Fig. 4.11(c)]	[Fig. 4.11(d)]
c_h	$0+\pi$	$0+\pi$	0
	[Fig. 4.10(e)]	[Fig. 4.11(c)]	[Fig. 4.10(f), 4.11(d)]

paths of J_1, J_2, and J_4 (but not J_3 which has an inversion center, see Fig. 4.7(b) for exchange paths) can mix the singlet and triplet states, and allow for magnetic-dipole transitions.[81] However, it is more likely that an electric-dipole dynamical Dzyaloshinskii-Moriya mechanism (Sec. 2.1.7) dominates the excitation intensities according to the following estimates.

The ratio of matrix elements of both mechanisms is determined by two factors that can be roughly calculated following the approach by O. Cépas and T. Ziman.[22]. The first factor involves the ratio of dipolar energies and is large, $\frac{\vec{D}\cdot\vec{e}^\omega}{g\mu_B|\vec{h}^\omega|} \sim 200$, where $|\vec{D}| \sim 10e \times 0.1$ Å, for a displacement of 0.1 Å of the charge $10e$ of the two Cr ions and $|\vec{e}^\omega| = c|\vec{h}^\omega|$ (c the speed of light). The second factor is the ratio of the phonon-modulation superexchange δJ_0 over the phonon frequency Ω. The lower-lying phonon was observed at $\Omega = 10$ meV,[99, 98] while δJ_0 is unknown and could be as small as $\sim 0.1 - 1$ meV. In $CuGeO_3$ for instance, small static distortions of ~ 0.01 Å [20] below the spin-Peierls transition led to a superexchange modulation of ± 0.8meV on successive bonds,[19] giving a much larger estimate of δJ_0 of a few meV for a phonon displacement. Here, we note another enhancement factor of $J_0/J_i' \sim 5$ because the dynamical Dzyaloshinskii-Moriya interaction occurs along the strong bonds and the static one along the weak bonds. Therefore even with the low figure of $\delta J_0 \sim 0.1$ meV, we arrive at a ratio of intensities of $\left(\frac{\vec{D}\cdot\vec{e}^\omega}{g\mu_B|\vec{h}^\omega|} \times \frac{\delta J_0}{\Omega} \times \frac{J_0}{J_i'}\right)^2 \approx 100$, suggesting that the electric dipole mechanism dominates. Note that a static Dzyaloshinskii-Moriya is expected to be of order $\delta g J_i'/g \sim 0.02$ meV (where $i = 1, 2$ or 4). It generally leads to finite magnetization of the ground state, which is not observed in the present compounds[6, 58], and results in a finite zero-field splitting. The fact these fingerprints are not observed here at an experimental resolution of ~ 10 GHz confirms that the

above estimate is an upper bound.

In the following, it will be shown that the observations can be explained in the scenario of dynamical Dzyaloshinskii-Moriya mechanism. We consider an electric-dipole coupling between radiation and spins,

$$W = \sum_{i,\alpha,\beta} e^{\omega}_{\alpha} A_{\alpha\beta} (\mathbf{S}_{i1} \times \mathbf{S}_{i2})_{\beta} \tag{4.3}$$

where i refers to the spin dimers, and $A_{\alpha\beta}$ is a coupling constant that couples the electric field of the radiation along the α direction with the vector product of spins along the β direction, that has the Dzyaloshinskii-Moriya symmetry. This is the simplest spin operator for $s = 1/2$ systems that breaks spin rotation symmetry (but not the time-reversal symmetry), and allows for a non-zero matrix element for singlet-triplet transitions.

Operators of the same form have been used to explain double magnon excitations in several antiferromagnetic systems,[31, 37] and similar processes in dimer systems,[21, 22] but the microscopic mechanism remains unclear. In the latter case, it is assumed that an *optical* phonon breaks the inversion symmetry within the dimer instantaneously. Since the electronic hopping is much faster than lattice vibrations, superexchange takes place in a dimer with no inversion center. The Dzyaloshinskii-Moriya interaction is therefore generated via the spin-orbit coupling, and is linear in the ionic displacements to first order. Typically $A_{\alpha\beta} = D^{\alpha} d^{\beta}$ where d^{β} is the instantaneous Dzyaloshinskii-Moriya vector and D^{α} the electric dipole of the unit cell created by the virtual phonon (see an example in Fig. 4.12).

Symmetry arguments. The coupling constant $A_{\alpha\beta}$ must be constrained by the crystal symmetries of the lattice in the presence of the radiation electric field. In particular, they should be identical from unit cell to unit cell but may vary within the unit cell. The space group $C2/c$ has four symmetry elements, namely, identity *1*, inversion center *-1*, two-fold rotation axis *2*, and *ac*-glide plane *c* with glide vector $(0, 0, 1/2)$, as shown in Fig. 4.7(c).[1] The last two symmetry operations always transform the pseudo-vector $\mathbf{T}_{12} \equiv \mathbf{S}_1 \times \mathbf{S}_2$ of the two dimerized spins in one layer onto one in the next layer, labeled with primes, as in Fig. 4.7(b). By using these symmetries, we constrain the coupling constants:

- $e^{\omega} \| a, c$: the *ac* glide plane leaves e^{ω} invariant, transforms T^{b}_{12} onto $T^{b}_{1''2''}$, and $T^{a,c}_{12}$ onto $-T^{a,c}_{1''2''}$ (Fig. 4.7). The coupling constants $A_{\alpha\beta}$ within the unit cell are therefore not independent but only the $\pm$ phases appear: the operator W in Eq. (4.3) will generate excitations to the acoustic and optical branches, respectively.

- $e^{\omega} \| b$: the two-fold rotation axis is along the b axis. It leaves e^{ω} invariant and transforms T^{b}_{12} onto $-T^{b}_{1'2'}$, and $T^{a,c}_{12}$ onto $T^{a,c}_{1'2'}$: the operator W will generate excitations to the optical and acoustic branches, respectively.

Based on these symmetries, this mechanism predicts transitions to occur at energies of the acoustic and optical modes, in perfect agreement with the energies observed for both compounds. We emphasize that no static breaking of inversion symmetry is needed.

A finite external magnetic field **H** splits the triplet modes and each mode has its own intensity. If all the involved pseudo-vectors $\mathbf{T}_{ij}$ in the operator W are parallel to the magnetic field $\mathbf{H}\|z$, only the transition to the $S^z = 0$ component of the triplet occurs, but it is invisible in the present high-field ESR setup. Therefore only the components of $\mathbf{T}_{ij}$ that are perpendicular to **H** generate observable transitions. Taking into account the symmetry arguments given above, we infer the results given in Table 4.5.

Table 4.5: *Theoretically* predicted excitations to the $S^z = \pm 1$ triplet components according to the dynamical mechanism in the *monoclinic* notations. The acoustic mode and optical mode are noted here as '0' and 'π', respectively, for short. The responsible matrix elements are given in the brackets following the corresponding modes. e^ω denotes the ac electric field and H denotes the applied magnetic field.

$e^\omega \backslash H$	a	b	c
a	$0(A_{ab}) + \pi(A_{ac})$	$\pi(A_{aa}, A_{ac})$	$0(A_{ab}) + \pi(A_{aa})$
b	$0(A_{bc}) + \pi(A_{bb})$	$0(A_{ba}, A_{bc})$	$0(A_{ba}) + \pi(A_{bb})$
c	$0(A_{cb}) + \pi(A_{cc})$	$\pi(A_{ca}, A_{cc})$	$0(A_{cb}) + \pi(A_{ca})$

The selection rules given in Table 4.5 cannot be strictly tested experimentally, because in the low-temperature phase the samples have three monoclinic twins rotated about the c_h axis by an angle of 60° with each other.[76] As a consequence, a field applied along the hexagonal axis, a_h or b_h, has components along a and b, thus mixing the selection rules. Furthermore, the hexagonal c_h-axis is tilted from the c-axis by 12°, so that a field applied along c_h has a main component along c but also a small component along a. The mixing of the different components implies that both modes are predicted to have finite intensities in all the experimental configurations studied here, if the corresponding couplings $A_{\alpha\beta}$ (given in Table 4.5) are non-zero. However, the optical mode is not detected in the configuration $e^\omega \| c_h$, $H \| c_h$, see Table 4.4, with e^ω, the electric field of the polarized electromagnetic wave, and H, the applied magnetic field.. If we ignore the difference between the c_h and c axes (which is small), the extinction of the optical mode for the configuration $e^\omega \| c_h$, $H \| c_h$ can be interpreted by postulating a vanishing (or weak) coupling constant $A_{ca} = 0$, see Table 4.5. Given that all the coupling elements are allowed by symmetry in the low temperature phase, it is difficult to prove that A_{ca} vanishes.

We now discuss this extinction as the result of a possible approximate symmetry,

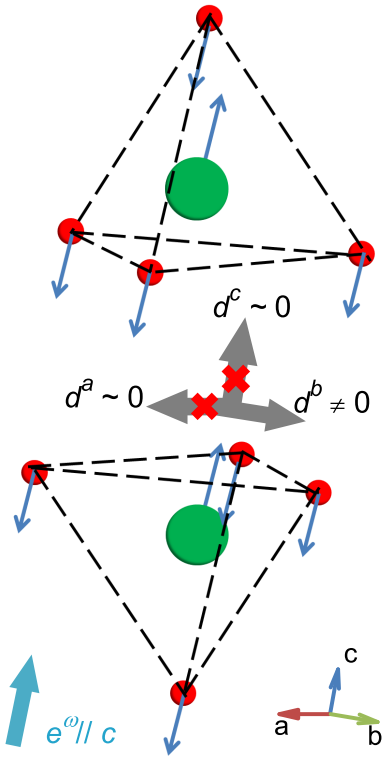

Figure 4.12: Illustration of the coupling constants $A_{ca} \sim 0$, $A_{cb} \neq 0$, and $A_{cc} \sim 0$. The spin dimer Cr_2O_8 distorts in the ac electric field $e^{\omega} \| c$ with associated instantaneous Dzyaloshinskii-Moriya vectors d^a, d^b, and d^c.[94]

originating from the higher symmetry of the high-temperature phase. In the high-temperature phase, there are three mirror planes at 120° bisecting the basal O-O bonds and containing the two Cr ions of the dimer. Since e^{ω} along c_h does not break these symmetries, the instantaneous Dzyaloshinskii-Moriya vector should be perpendicular to all, and hence would vanish. None of these mirror planes are exact symmetries in the low-temperature phase, but one of them coincides with the ac plane and contains the two Cr ions.[1, 23] If we assume that this plane remains an approximate mirror plane, the instantaneous Dzyaloshinskii-Moriya vector would be along the b axis, when $e^{\omega} \| a, c$ respects this symmetry, *i.e.*, $A_{ab} \neq 0, A_{cb} \neq 0$. Therefore we would expect zero couplings ($A_{aa} = 0, A_{ac} = 0, A_{ca} = 0, A_{cc} = 0$) if this symmetry were exactly preserved, or approximately zero if this symmetry were weakly broken. This gives a justification for the extinction of the optical mode in both compounds ($A_{ca} \approx 0$). It is also consistent with the weak intensity of the optical mode for the configuration $e^{\omega} \| c_h$, $H \| a_h$ which is observed in $Sr_3Cr_2O_8$ [Fig. 4.10(e)], provided

that $A_{cc} \approx 0$ is weak. However, in $Ba_3Cr_2O_8$ with the configuration $e^{\omega} \| c_h$, $H \| b_h$ [Fig. 4.11(c)] the optical mode is much stronger. Within the present mechanism, this can be interpreted only with a finite $A_{cc} \neq 0$ (since $A_{ca} \approx 0$). The vanishing couplings suggest that the corresponding symmetries are only weakly broken across the structural phase transition in the sense that the distortions are too small to give detectable absorptions.

4.3 Summary

Low-energy magnetic properties of the spin-1/2 dimerized antiferromagnets $CuTe_2O_5$, $Sr_3Cr_2O_8$, and $Ba_3Cr_2O_8$ have been studied by the high-field electron spin resonance spectroscopy. With the capability to tune frequency and polarization of the electromagnetic wave, this is a powerful tool to study the spin excitations, and thus to infer the exchange interactions, magnetic anisotropies, and symmetries of the system.

The spin dimer systems, $CuTe_2O_5$ based on Cu^{2+} ion, $Sr_3Cr_2O_8$ and $Ba_3Cr_2O_8$ based on Cr^{5+} ions, exhibit a nonmagnetic spin-singlet ground state and a magnetic spin-triplet excited state. Spin singlet-triplet excitations with total spin changed by one, i.e. $\Delta S = 1$, are observed in all the three systems. The observation of such magnetic excitations with $\Delta S = 1$ is a strong indication that the spin Hamiltonian should contain an antisymmetric exchange term and the inversion symmetry should be broken at the dimer center. Dzyaloshinskii-Moriya interaction is an antisymmetric exchange interaction that is the leading term in the spin-orbit coupling. Thus it is adopted to explain the observations. The Dzyaloshinskii-Moriya interaction should comply with the constraints imposed by symmetry. The inversion symmetry could be broken either statically due to the lattice distortion, as used to describe $CuTe_2O_5$, or dynamically due to the phonon-induced instantaneous lattice displacement, as used to describe the experimental observations in $Sr_3Cr_2O_8$ and $Ba_3Cr_2O_8$. The dynamical mechanism is possible because the spin excitations occur on a time scale shorter than the phonon excitations.

5 Orbital Ordering and Orbital Fluctuations

The orbital degrees of freedom and their coupling to other degrees of freedom play an important role in understanding the physics in many transition-metal compounds including colossal magnetoresistive manganites, vanadates, and the new class of iron-based superconductors.[91, 53, 60] Orbital ordering mechanisms,[61] collective orbital excitations,[80] and frustration effects in the orbital sector have attracted considerable attention and formed the research field of *orbital physics*. Exotic ground states such as orbital and spin-orbital liquids have been explored both experimentally and theoretically.[54] Orbital fluctuations play an important role in the formation of these states and may even induce a dimerization of spins via magnetoelastic coupling.[48]

This chapter will be devoted to the temperature dependent properties of the orbital and lattice degrees of freedom in the spin-dimer systems $Sr_3Cr_2O_8$ and $Ba_3Cr_2O_8$. By measuring the phononic excitation spectrum and specific heat, the persistence of strong orbital fluctuations is found in $Sr_3Cr_2O_8$ far below the Jahn-Teller structural transition temperature, while in $Ba_3Cr_2O_8$ complete orbital ordering is established just below the structural phase transition.

5.1 Orbital ordering in $Ba_3Cr_2O_8$

5.1.1 Infrared spectra

Figure 5.1 shows reflectivity spectra of $Ba_3Cr_2O_8$ measured for the ac electric field e^ω parallel to the crystalline hexagonal a_hb_h-plane ($e^\omega \parallel a_hb_h$-plane) at 295 K and 4 K, which are above and below the Jahn-Teller transition temperature $T_{JT} = 70$ K, respectively. The seven modes observed above T_{JT} are tentatively assigned as $E_u(j)$ (j=1,...,7). This is in accord with the normal mode analysis of IR active modes, which gives the irreducible representations

$$\Gamma_h = 6A_{2u}(e^\omega \parallel z) + 7E_u[e^\omega \parallel (x, y)] \tag{5.1}$$

for the high-temperature hexagonal $R\bar{3}m$ (No. 166) structure.[57, 59] The small feature between modes $E_u(6)$ and $E_u(7)$ could be due to the defects or imperfection at the sample surface.

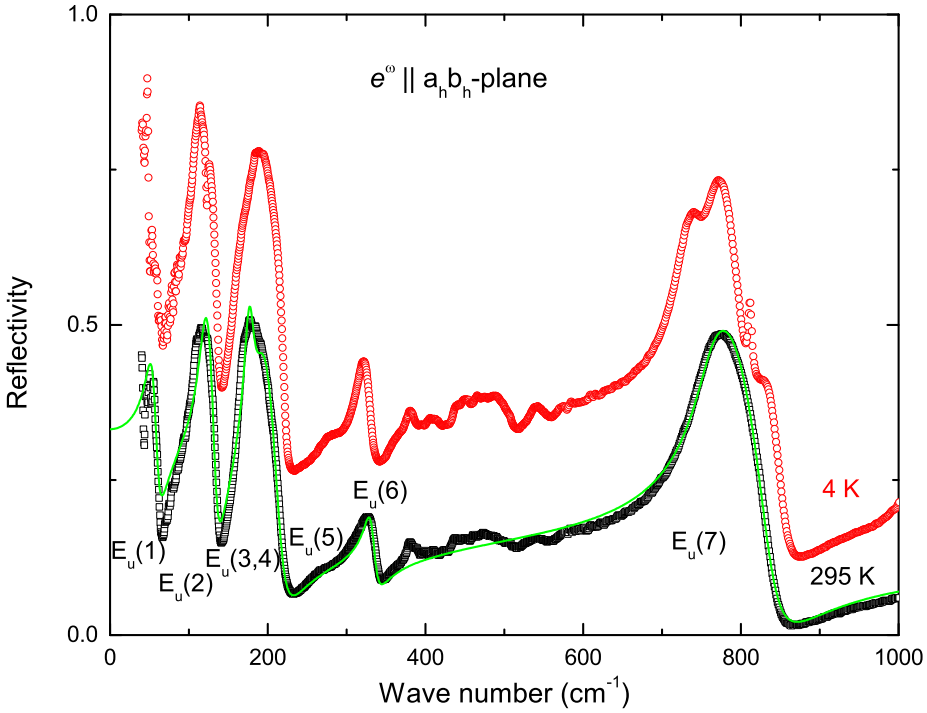

Figure 5.1: Reflectivity spectra of $Ba_3Cr_2O_8$ measured with $e^{\omega} \parallel a_h b_h$-plane at 295 K and 4 K. The spectrum of 4 K is shifted with respect to that of 295 K by a constant of 0.1. Infrared-active phonon modes $E_u(j)(j = 1, ..., 7)$ are marked at the 295 K spectrum for the hexagonal structure. Solid line is a fit of Drude-Lorentz model to the data of 295 K as described in the text.

The quantitative analysis on the phonon modes is performed by fitting the reflectivity spectrum using the Lorentz model (Sec. 3.1.1). The reflectivity spectrum measured at room temperature and fitted with the $7E_u$ phonon modes is illustrated by the solid line in Fig. 5.1. The fit agrees well with the experimental data. Note that the lowest lying mode $E_u(1)$ could not be completely resolved and only the high frequency flank has been fitted. Thus, there are large uncertainties in the fitting parameters of $E_u(1)$. The obtained parameters are summarized in Table 5.1.

Temperature dependence

In the monoclinic phase below the Jahn-Teller transition, the number of expected normal infrared modes increases to $19A_u$ for the radiation electric field parallel to the monoclinic b_m axis and to $20B_u$ for the electric field parallel to the monoclinic

Table 5.1: Eigenfrequency ω_0, effective ionic plasma frequency Ω and damping coefficient γ of all $7E_u$ phonon modes in $Ba_3Cr_2O_8$ at 295 K. $\epsilon_\infty = 4.31$.

E_u	Phonons		
Mode	ω_0 (cm^{-1})	Ω (cm^{-1})	γ (cm^{-1})
1	52.6	101.2	13.5
2	119.7	187.9	14.0
3	174.7	182.8	10.6
4	188.4	174.1	26.2
5	274.7	166.0	172.1
6	330.5	120.4	14.9
7	759.2	718.2	45.5

$a_m c_m$-plane[57, 59]

$$\Gamma_m = 19A_u(e^\omega \parallel y) + 20B_u[e^\omega \parallel (x, z)]. \tag{5.2}$$

Since the hexagonal axes a_h and b_h have the monoclinic a_m and b_m components (Table 4.3), the IR spectra measured with $e^\omega \parallel a_h b_h$-plane below $T_{JT} = 70$ K should display all the $19A_u$ and $20B_u$ modes.

Careful inspection on the temperature-dependent reflection spectra reveals that the hexagonal modes $E_u(2)$ and $E_u(7)$ split below T_{JT}, while the other modes, which are hardening with decreasing temperature, do not split below T_{JT}. Therefore, we focus on the temperature-dependent features of modes $E_u(2)$ and $E_u(7)$, and try to describe the low-temperature modes with the Lorentzian functions. As indicated by the arrows in Fig. 5.2, we try to model the low-temperature spectra with two modes corresponding to $E_u(2)$ and $E_u(7)$, respectively.

For the monoclinic structure, the dielectric matrix

$$\begin{pmatrix} \epsilon_{aa} & & \epsilon_{ca} \\ & \epsilon_{bb} & \\ \epsilon_{ac} & & \epsilon_{cc} \end{pmatrix} \tag{5.3}$$

has three independent elements ϵ_{aa}, ϵ_{cc} and ϵ_{ca} for $e^\omega \parallel a_m c_m$-plane. Therefore one has to measure the reflection spectra with three different polarizations of the electric fields in order to determine unambiguously the eigenfrequencies, damping coefficients and plasma frequencies of the B_u phonon modes.[62]

Due to the existence of three monoclinic twins, it is difficult to distinguish the B_u modes for $e^\omega \parallel a_m$ from the A_u modes for $e^\omega \parallel b_m$. Thus, in this case, the modeling here with Lorentzian functions is a way to parameterize the reflectivity

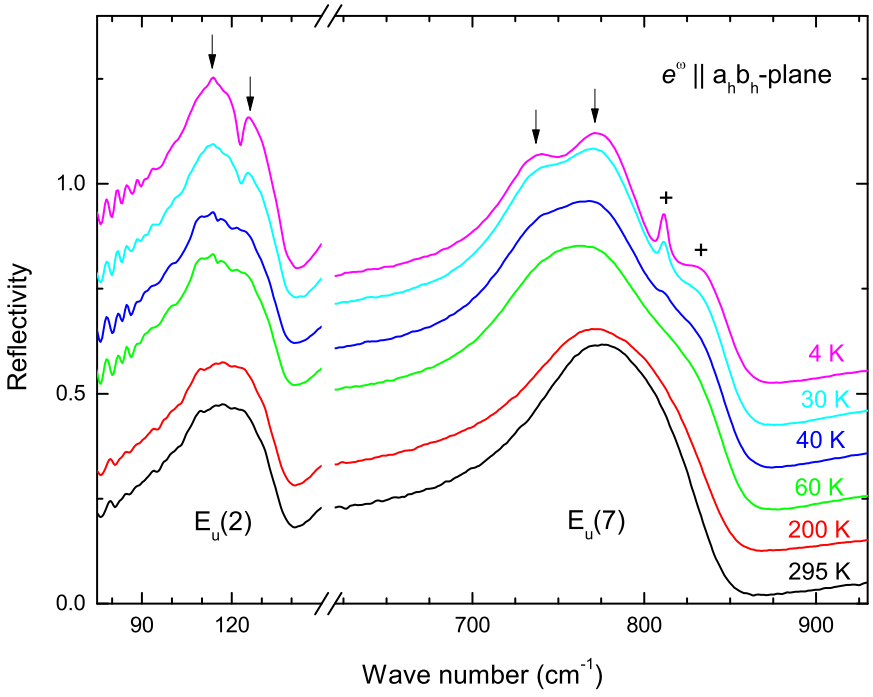

Figure 5.2: Reflectivity spectra of $Ba_3Cr_2O_8$ corresponding to IR phonon modes $E_u(2)$ and $E_u(7)$ measured with $e^{\omega} \parallel a_h b_h$-plane at various temperatures. The spectra are shifted with respect to that at 295 K by a constant in order to clearly illustrate the evolution of phonon modes with decreasing temperature.

spectra and reveal changes occurring at T_{JT}. The fitting results of eigenfrequency, damping coefficient and plasma frequency are summarized as a function of temperature in Fig. 5.3, which clearly shows the splitting of phonons just below T_{JT}, consistent with the phase transition to the monoclinic structure.

The modes marked by "+" in Fig. 5.2 at 812 cm^{-1} and 834 cm^{-1} are visible for $T \leq 40$ K. These modes probably are phonon modes of the monoclinic structure, which have small spectral weight and large damping effect that can not be distinguished from the strong modes corresponding to $E_u(7)$ at higher temperatures.

5.1.2 Specific heat

Figure 5.4(a) shows the specific heat of $Ba_3Cr_2O_8$ measured as a function of temperature. Two anomalies can be observed in the specific-heat data. A sharp anomaly indicated by a dashed vertical line can be easily recognized at 70 K. Another feature

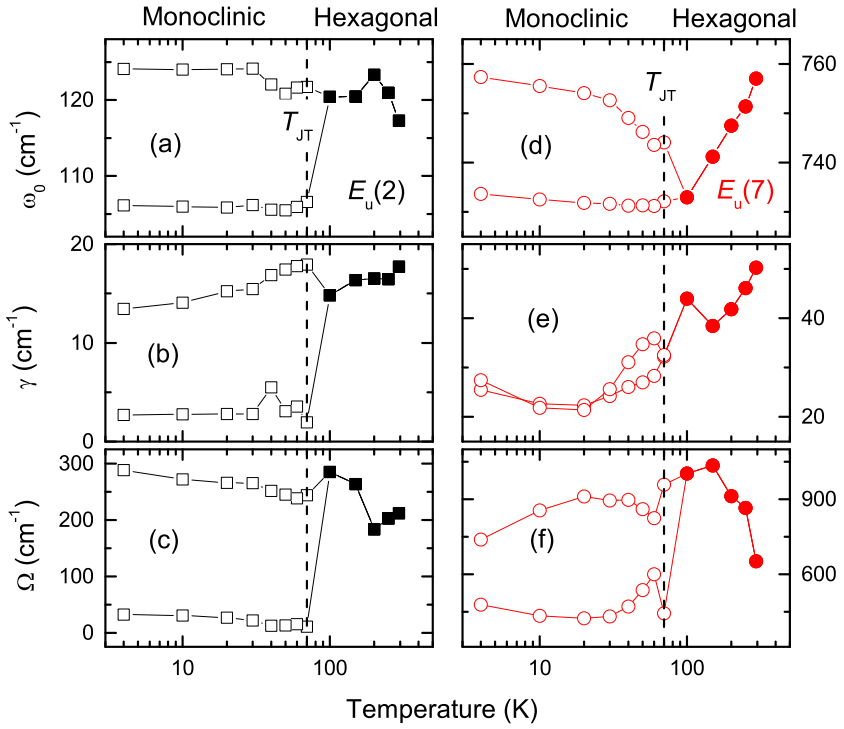

Figure 5.3: Temperature dependence of eigenfrequency (a, d), damping coefficient (b, e) and plasma frequency (c, f) for modes $E_u(2)$ and $E_u(7)$ in $Ba_3Cr_2O_8$ on a semi-logarithmic scale. Jahn-Teller temperature T_{JT} is indicated by vertical dashed lines.

observed below 20 K is marked by an arrow. The inset of Fig. 5.4(a) shows the specific heat over temperature C/T vs. T measured in various external magnetic fields. The anomaly at $T_{JT} = 70$ K is independent of the external magnetic fields, and marks the structural phase transition from hexagonal $R\bar{3}m$ to monoclinic $C2/c$, in agreement with the results obtained from neutron diffraction measurements.[57] The anomaly below 20 K, sensitive to changes of the magnetic field, is attributed to the magnetic degrees of freedom.

The lattice contribution to the specific heat C_{latt} can be described according to the phonon spectra that have been determined in the last section. We model the lattice contribution by a sum of one isotropic Debye and four isotropic Einstein terms with the fixed ratio $D : E_1 : E_2 : E_3 : E_4 = 1 : 3 : 4 : 3 : 2$ between these terms accounting

for the 39 degrees of freedom per formula unit:

$$C_{latt}(T) = D(\theta_D, T) + 3E(\theta_{E1}, T) + 4E(\theta_{E2}, T) + 3E(\theta_{E3}, T) + 2E(\theta_{E4}, T), \tag{5.4}$$

where D denotes the isotropic Debye contribution

$$D(\theta_D, T) = 9R\left(\frac{T}{\theta_D}\right)^3 \int_0^{\theta_D/T} \frac{\xi^4 e^\xi}{(e^\xi - 1)^2} d\xi \tag{5.5}$$

and E denotes the Einstein contribution

$$E(\theta_E, T) = 3R\frac{(\theta_E/T)^2 e^{\theta_E/T}}{(e^{\theta_E/T} - 1)^2} \tag{5.6}$$

with the molar gas constant $R = 8.314$ JK^{-1}mol^{-1} and the corresponding Debye and Einstein temperatures θ_D, θ_{E1}, θ_{E2}, θ_{E3}, and θ_{E4}. The lattice contribution to the specific heat can be described with the Debye and Einstein temperatures $\theta_D = 123$ K, $\theta_{E1} = 137$ K, $\theta_{E2} = 265$ K, $\theta_{E3} = 658$ K, and $\theta_{E4} = 1270$ K, in agreement with the frequency ranges where IR active phonons of the hexagonal structure occur. The fitting curve is shown as a solid line in Fig. 5.4(a), which agrees well with the specific-heat data above T_{JT}. It will be shown in the next section that this model with the same ratios can also describe the specific-heat data of the isostructural $Sr_3Cr_2O_8$.

Below T_{JT}, the fits deviate slightly from the experimental data indicating that the magnetic and orbital contribution to the specific heat has to be taken into accounts below the Jahn-Teller transition. The residual specific heat divided by temperature $(C - C_{latt})/T$ is shown in Fig. 5.4(b). One can clearly recognize a λ-shaped anomaly at the Jahn-Teller transition around 70 K and the magnetic anomaly below 20 K, which are well separated in the temperature scale. The corresponding entropy

$$S(T) = \int_0^T d\vartheta (C - C_{latt})/\vartheta \tag{5.7}$$

reaches a value slightly lower than the expected $S = 4R\ln 2$ for the sum of magnetic and orbital contribution as shown in Fig. 5.4(c). For a spin-1/2 dimer, the entropy increases by $2\ln 2$ from the ordered to the disordered spin state. Because there is essentially one spin dimer per formula unit of $Ba_3Cr_2O_8$, the magnetic contribution to the entropy should be $2R\ln 2$. This value is reached at 20 K indicated in Fig. 5.4(c). Below this temperature, the specific heat shows a significant dependence on the external magnetic field. Above the Jahn-Teller transition, each Cr ion has a doubly-degenerated e orbital occupied by a single electron. Orbital degrees of freedom will contribute to the entropy by another $2R\ln 2$, where the two Cr ions per formula unit have been taken into account.

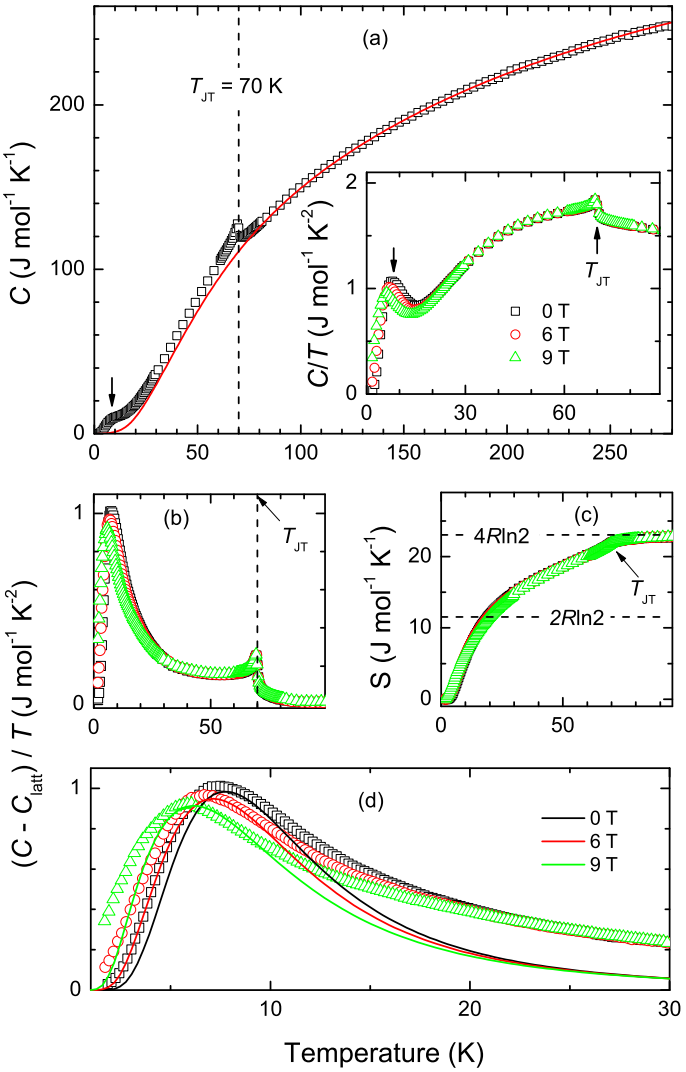

Figure 5.4: (a) Specific heat of $Ba_3Cr_2O_8$ without applied magnetic field. Solid line is a fit of the lattice contribution to the specific heat according to Debye and Einstein models in Eqs. (5.4)-(5.6). Inset shows the specific heat divided by temperature C/T measured at various magnetic fields. (b) Residual specific heat $(C - C_{latt})/T$ and (c) the corresponding entropy obtained at different fields. (d) Fits to the magnetic contribution of the specific heat (solid lines) taking into account the Zeeman splitting of isolated spin dimers, as described in the text. The specific heat was measured by A. Günther.[98]

In order to describe the magnetic contribution to the specific heat, we consider a model with the intra-dimer exchange interaction and the Zeeman interaction but ignore the inter-dimer exchange interactions which are much smaller than the intra-dimer interaction.[57] Thus, we can model the magnetic contribution to specific heat by the Schottky-type specific heat (Sec. 2.1.2) with the partition function

$$Z = \sum_{i=0}^{3} e^{-\beta\epsilon_i} \tag{5.8}$$

and the energies $\epsilon_{0,1,2,3} = 0, J_0 - g\mu_B H, J_0, J_0 + g\mu_B H$, where μ_B is the Bohr magneton, H is the magnetic field, and $\beta \equiv 1/k_B T$ with the Boltzmann constant k_B. The solid lines in Fig. 5.4(d) indicate the calculated specific heat according to this model, where the intra-dimer exchange interaction $J_0 = 2.38$ meV was determined by inelastic neutron experiments,[57] and the g-factor $g = 1.94$ was measured by electron spin resonance experiments.[58, 51] This simple model captures the most important features of the experimental data: The maximum of the modeled specific heat is in good agreement with the experimental data. The maximum shifts to lower temperatures and decreases with increasing magnetic fields. This comes from the fact that the gap between the lower-lying triplet state and the singlet state is reduced due to the Zeeman effect. Discrepancies between model and experiment probably arise due to the fact that the inter-dimer interactions, as well as the changes of the phonon spectra below the phase transition, are not considered.

5.2 Orbital fluctuations in $Sr_3Cr_2O_8$

5.2.1 Infrared spectra

Figure 5.5 shows reflectivity spectra of $Sr_3Cr_2O_8$ measured with the ac electric field e^ω parallel to the hexagonal a_h-axis at 295 K above the Jahn-Teller transition temperature. Since $Sr_3Cr_2O_8$ and $Ba_3Cr_2O_8$ are isostructural compounds, $Sr_3Cr_2O_8$ has the same representations of the infrared-active phonons as $Ba_3Cr_2O_8$ given in Eq. (5.1) and Eq. (5.2).

The profile of $Sr_3Cr_2O_8$ phonon spectra is very similar to that of the isostructural compound $Ba_3Cr_2O_8$. The room temperature spectrum for $e^\omega \parallel a_h$ is quantitatively analyzed using the Lorentz model with seven oscillators. The solid line in Fig. 5.5 represents a fit to the experimental result according to this model. The obtained eigenfrequencies, ionic plasma frequencies, and damping coefficients of the seven phonon modes are given in Table 5.2. The high-energy phonons in $Sr_3Cr_2O_8$ have higher eigenfrequencies than those in $Ba_3Cr_2O_8$, since the Sr ions have smaller mass than Ba ions. It will be shown that the Debye and Einstein temperatures in $Sr_3Cr_2O_8$ obtained from fitting the specific heat are also higher than those in $Ba_3Cr_2O_8$.

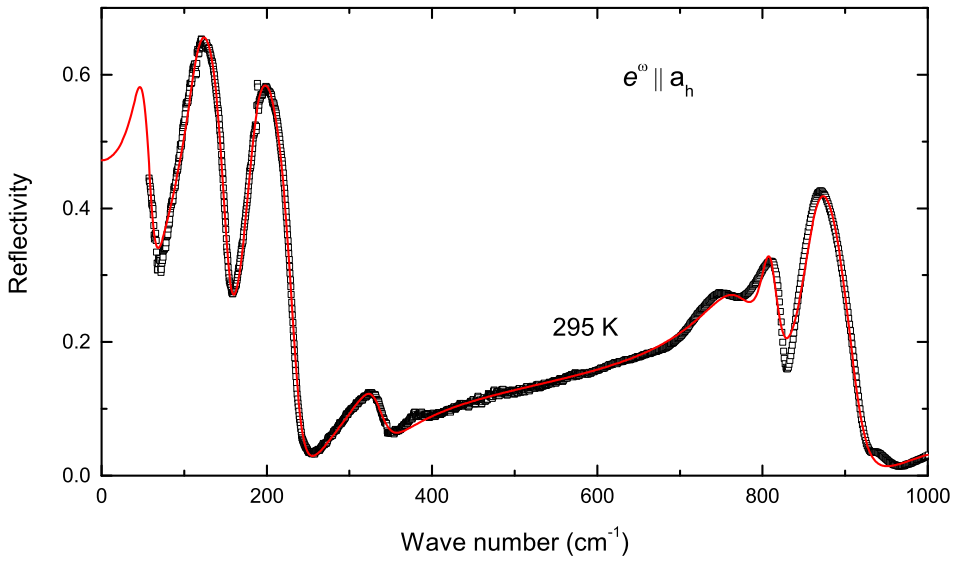

Figure 5.5: Reflectivity spectra of $Sr_3Cr_2O_8$ with $e^{\omega} \parallel a_h$ at 295 K. The solid line is a fit with the Lorentz model using seven oscillators.

Temperature dependence

Figure 5.6(a) shows the infrared reflectivity spectra for $e^{\omega} \parallel c_h$ above and below the Jahn-Teller transition temperature $T_{JT} = 285$ K. For this polarization, $6A_{2u}$ normal infrared phonon modes are expected above T_{JT}, and $20B_u$ modes are expected below T_{JT} since c_h is lying in the monoclinic $a_m c_m$ plane (Table 4.3). Thus, one would expect a drastic increase in the number of infrared active modes when comparing spectra below and above the Jahn-Teller transition, e.g., at 250 K and 295 K. However, the observed spectra do not change dramatically across T_{JT}. Only one additional mode $B_u(16)$ becomes visible at 250 K, while the expected 20 B_u modes of the low-temperature structure appear only gradually upon further cooling. This behavior is illustrated in Fig. 5.6(b) where spectra at 150 K, 100 K, and 20 K are compared. The modes present at 20 K can be observed at 100 K, while in the phonon spectrum at 150 K several modes are not resolved anymore and appear to be strongly broadened.

The similar temperature dependent behavior can also be observed for the phonon spectra measured for $e^{\omega} \parallel a_h$, shown in Fig. 5.6(c)(d). Due to the existence of twins, all the $19A_u$ and $20B_u$ phonon modes can be excited by the electric field along the a_h axis in the low temperature phase, while only the $7E_u$ modes are expected above the Jahn-Teller transition. From Fig. 5.6(c) only one additional mode appears right below T_{JT}. All modes can be resolved only when the temperature is below 150 K.

These temperature dependent features can be interpreted as a signature of strong

Table 5.2: Eigenfrequency ω_0, effective ionic plasma frequency Ω and damping coefficient γ of all $7E_u$ phonon modes in $Sr_3Cr_2O_8$ at 295 K. $\epsilon_\infty = 3.95$.

E_u	Phonons		
Mode	ω_0 (cm^{-1})	Ω (cm^{-1})	γ(cm^{-1})
1	47.0	176.2	19.5
2	113.3	324.3	25.2
3	181.9	236.7	25.1
4	329.3	156.9	41.7
5	767.7	546.0	77.6
6	805.8	289.0	21.6
7	858.0	458.0	34.8

fluctuations which dominate the lattice dynamics and lead to a strong damping and broadening of phonons in the temperature range $T^* < T < T_{JT}$ with 100 K $< T^* <$ 150 K.

The strong fluctuations are also manifested in the temperature evolution of Raman phonons. Figure 5.7(a) shows low-frequency Raman spectra from 295 K above T_{JT} down to 3 K, reported by D. Wulferding et al.[102] Similar to the temperature dependence of the infrared spectra, the Raman spectra do not exhibit all the low-symmetry phonons immediately across the structural phase transition, but only when the temperature is down to 100 K and below. This can be clearly seen in the temperature dependence of the phonon frequencies shown in Fig. 5.7(b). The fluctuation regime has been suggested to be above $T^* = 120$ K according to detailed studies by the conventional X-band ($\nu = 9.48$ GHz) electron spin resonance. Based on these investigations, the orbital gap between $d_{3z^2-r^2}$ and $d_{x^2-y^2}$ (Fig. 4.6) was estimated as $\delta = 33.4$ meV.[99]

5.2.2 Specific heat

Figure 5.8(a) shows the specific heat over temperature C/T as a function of temperature in $Sr_3Cr_2O_8$. A peak without any thermal hysteresis is clearly visible at $T_{JT} = 285$ K, indicating an order-disorder phase transition at this temperature. This anomaly can be associated with the orbital-ordering transition reported to occur at about 275 K as determined by neutron-diffraction results.[23] Moreover, an additional broad shoulder is discernible at about $T = 20$ K, indicated by an arrow in Fig. 5.8(a).

The specific heat data is analyzed by assuming that the total heat capacity originates from three different contributions, a magnetic contribution C_{mag} corresponding to the thermal population of the excited dimer states, a lattice contribution C_{latt} due to

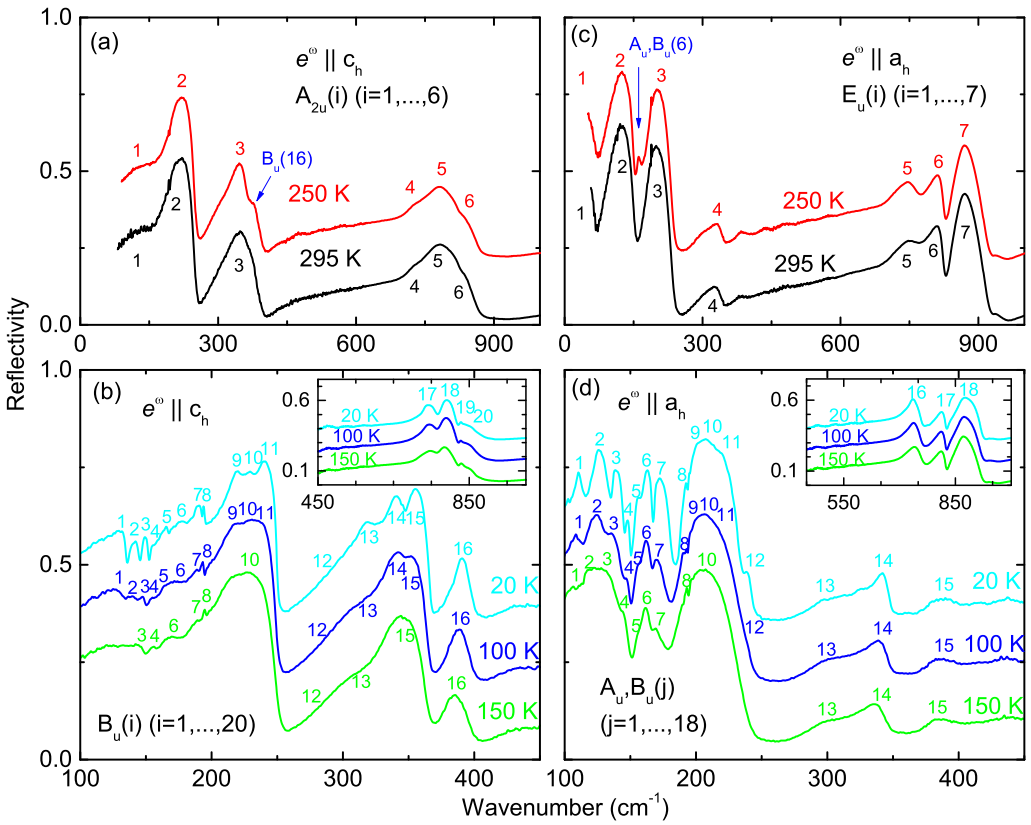

Figure 5.6: Reflectivity spectra of $Sr_3Cr_2O_8$ for $e^\omega \| c_h$ and $e^\omega \| a_h$ at various temperatures. The spectra are shifted with respect to the ones at 150 K and 295 K in order to illustrate the evolution of phonon modes with temperature. Insets in (b) and (d): High frequency modes as function of temperature.

acoustic and optical phonons, and an electronic contribution reflecting the orbital degrees of freedom.

The magnetic contribution is approximated by a Schottky-type specific heat with the partition function $Z = \sum_{i=0}^{2} g_i e^{-\beta\epsilon_i}$, the excitation energies $\epsilon_{0,1,2} = 0, h\nu_0^{opt}, h\nu_0^{aco}$ and their degeneracies $g_{0,1,2} = 1, 2, 1$. The energies of the optical mode $h\nu_0^{opt} = 5.13$ meV and the acoustic mode $h\nu_0^{aco} = 6.08$ meV determined by the THz ESR transmission experiments have been used. The resulting magnetic specific heat from this simple approach, neglecting dispersion effects of the excited states, is shown in Fig. 5.8(a) as a dashed line and accounts well for the observed shoulder at 20 K.

The Debye and Einstein models in Eqs. (5.4)-(5.6) are used to describe the lattice contribution to the specific heat, as done for $Ba_3Cr_2O_8$. The dash-dotted line in

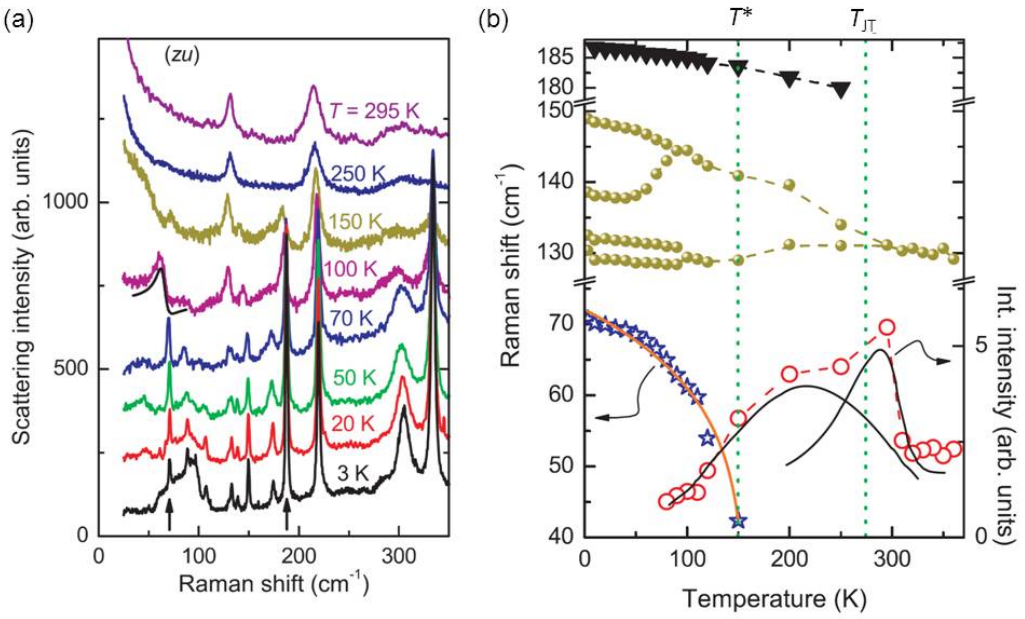

Figure 5.7: (a) Temperature evolution of low-frequency Raman spectra from 3 to 295 K measured with the incoming light parallel to the c_h-axis and unpolarized outgoing light. (b) Temperature dependence of the lower-lying Raman-phonon frequencies at 71, 129, 132, 138, 148, and 188 cm^{-1}. The red circles display the integrated intensity of the quasi-elastic scattering, which is deconvoluted into two contributions (black lines),[102] a sharp onset at T_{JT} due to structural phase transition and a broad maximum at lower temperatures reflecting the orbital fluctuations. The figures are adapted from Ref. [102].

Fig. 5.8 shows the lattice contribution with the Debye and Einstein temperatures θ_D = 135.5 K, θ_{E1} = 153.4 K, θ_{E2} = 306.2 K, θ_{E3} = 541.6 K, and θ_{E4} = 1360 K in agreement with the frequency ranges where IR active phonons of the hexagonal structure occur. Since $Sr_3Cr_2O_8$ has smaller molecular mass than $Ba_3Cr_2O_8$, the obtained Debye and Einstein temperatures of $Sr_3Cr_2O_8$ should be higher than those of $Ba_3Cr_2O_8$.[99] The fitted Debye-temperature ratio between $Ba_3Cr_2O_8$ and $Sr_3Cr_2O_8$ is 0.91, which is close to the ratio $\sqrt{m_{Sr_3Cr_2O_8}} : \sqrt{m_{Ba_3Cr_2O_8}} = 0.88$, where $m_{Sr_3Cr_2O_8}$ and $m_{Ba_3Cr_2O_8}$ are the molecular masses of $Sr_3Cr_2O_8$ and $Ba_3Cr_2O_8$, respectively.

Using the orbital gap Δ = 33.4 meV between $d_{3z^2-r^2}$ and $d_{x^2-y^2}$, we can additionally fix the orbital contribution C_{oo} below T^* = 120 T in the completely orbitally ordered phase by a two-level system, as shown in Fig. 5.8(b). Within these constraints the lattice contribution was modeled in such a way that no discontinuity occurs between

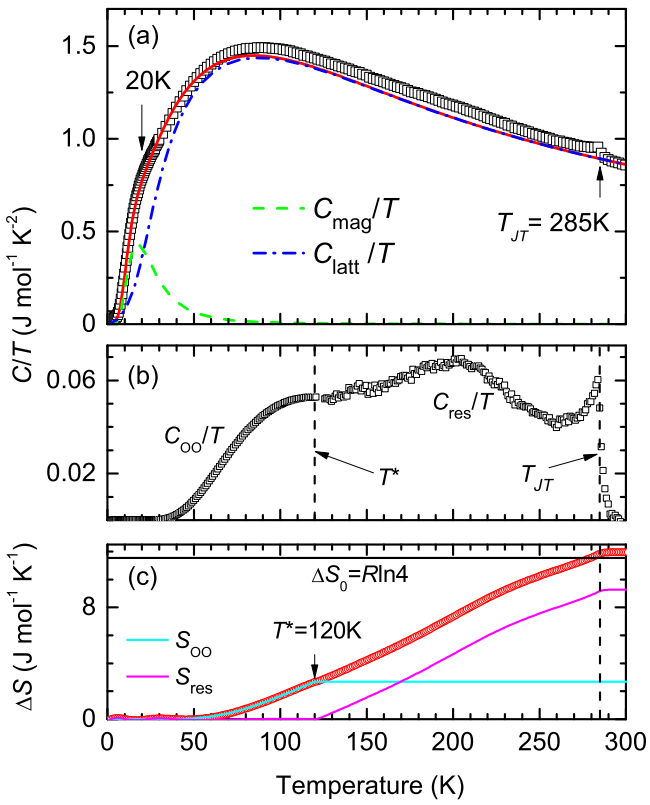

Figure 5.8: (a) Specific heat divided by temperature C/T vs T of $Sr_3Cr_2O_8$. The solid line is a superposition of the modeled magnetic (dashed line) and phonon contribution (dash-dotted line) as described in the text. Temperature dependence of orbital-related (b) specific heat and (c) entropy. The specific heat was measured by A. Günther.[99]

the Schottky-like term for $T < T^*$ and the residual specific heat $C_{res} = C - C_{mag} - C_{latt} - C_{oo}$ in the temperature regime $T^* < T < T_{JT}$. C_{oo} and C_{res} are shown together in Fig. 5.8(b). One can clearly recognize a λ-shaped anomaly at the Jahn-Teller transition at 285 K and a broad hump-like contribution below the transition followed by the Schottky-like contribution for $T < T^*$. This was also confirmed by the temperature dependence of integrated intensity of the quasielatic scattering revealed by the Raman experiment, as shown on the right coordinate in Fig. 5.7(b).

The entropy associated with the orbital degrees of freedom can be evaluated

$$\Delta S(T) = S_{oo}(T) + S_{res}(T) = \int_0^T d\vartheta (C_{oo} + C_{res})/\vartheta. \tag{5.9}$$

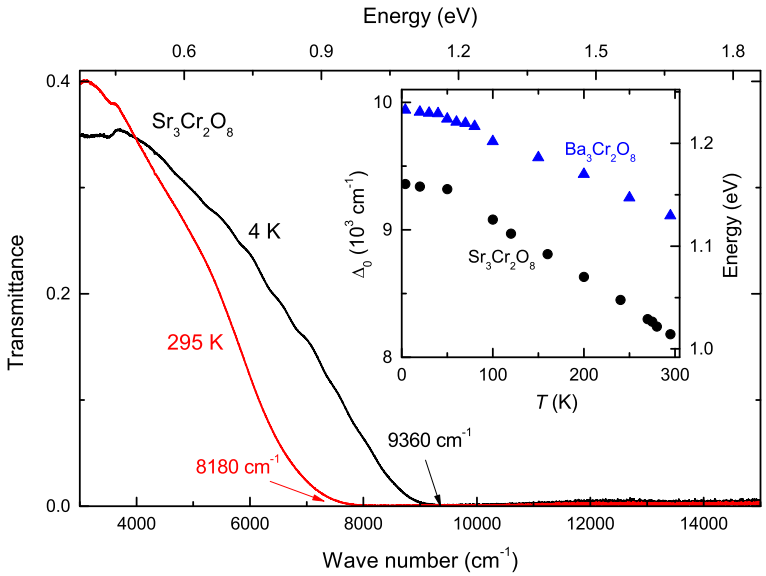

Figure 5.9: Near-infrared transmission spectra of $Sr_3Cr_2O_8$ at 295 K and 4 K. Inset: the observed absorption edge Δ_0 as a function of temperature in $Sr_3Cr_2O_8$ and in $Ba_3Cr_2O_8$ in the unit of cm^{-1} on the left coordinate and of eV on the right coordinate.

It reaches a value slightly higher than the expected $\Delta S_0 = R \ln 4$ [Fig. 5.8(c)]. We interpret this observation as due to persistent fluctuations of the orbital and lattice degrees of freedom in the temperature range $T^* < T < T_{JT}$ in agreement with the anomalous temperature dependence of the infrared and Raman phonons.

5.2.3 Electronic excitations in $Sr_3Cr_2O_8$

Near-infrared crystal field excitations

Figure 5.9 shows near-infrared transmission spectra of $Sr_3Cr_2O_8$ at 4 and 295 K. Absorption edge can be observed at 8180 cm^{-1} at 4 K and at 9360 cm^{-1} at 295 K. Its temperature dependence is summarized in the inset of Fig. 5.9. The energy increases slightly with decreasing temperature and saturates at low temperatures. We associate this absorption with a crystal-field excitation from the lower-lying e to the t_2 orbitals, see Fig. 4.6. $Ba_3Cr_2O_8$ exhibits larger excitation gap with a similar temperature dependence, which is also shown in the inset of Fig. 5.9 for comparison.

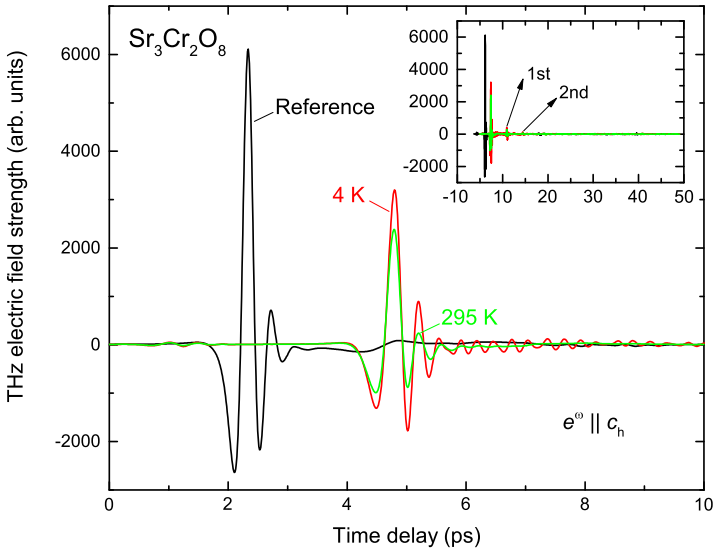

Figure 5.10: Time-domain electric field strength of the transmitted THz electromagnetic wave through a reference and a $Sr_3Cr_2O_8$ sample at 4 and 295 K with $e^{\omega} \parallel c_h$. Inset: The same time-domain signals are shown in the time-delay range of 50 ps. The peaks due to the first and second multiple interferences within the sample are indicated.

THz phonon-orbiton and vibronic excitations

Figure 5.10 shows the electric field strength of transmitted THz electromagnetic wave measured through a reference and a $Sr_3Cr_2O_8$ sample with $e^{\omega} \parallel c_h$ as a function of time delay at 4 and 295 K. High resolution can be achieved by measuring larger time delay range, as shown in the inset of Fig. 5.10. One can also see two peaks following the main one in the sample spectra due to multiple interference within the sample.

By Fourier transformation on the time-domain signal, the transmission spectra are obtained in the frequency domain. Figure 5.11 shows evolution of the transmission spectra with temperature from 295 K to 4 K. At 295 K, one can see a weak and a broad absorption band at 55 cm^{-1} which corresponds to the lower-lying phonon observed in Fig. 5.5. At 275 K right below T_{JT}, a strong absorption band at 67 cm^{-1} and a weak one at 90 cm^{-1} emerge, indicating that these phonon bands are associated with the structural phase transition.

The 55 cm^{-1} band is almost temperature independent above 150 K, but hardens with further cooling, and evolves into a well-defined mode at 57.0 cm^{-1} at 4 K, marked as mode 1. The 90 cm^{-1} band exhibits very similar temperature dependence: Below

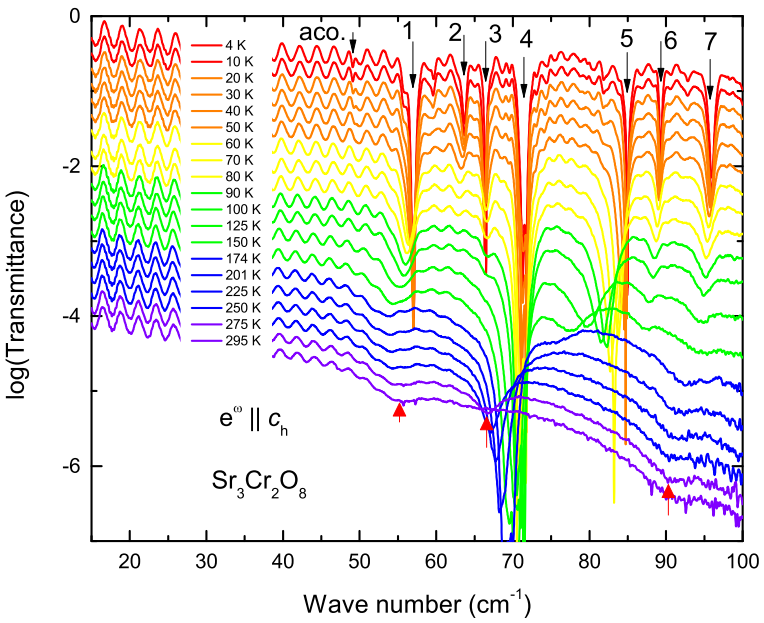

Figure 5.11: Evolution of transmission spectra in $Sr_3Cr_2O_8$ with temperature from 295 K to 4 K measured with $e^{\omega} \parallel c_h$. The spectra are shifted for clarity. 'aco.' marks the acoustic spin singlet-triplet excitations (see Sec. 4.2).

150 K it splits into two modes. These modes become narrow and are located at 89.3 cm^{-1} (mode 6) and at 96.0 cm^{-1} (mode 7) at 4 K. The 66 cm^{-1} band gradually hardens for $T < 275$ K, and evolves into modes 2 – 5 at 63.6, 66.4, 71.4, and 84.9 cm^{-1}, respectively, at 4 K. The mode 5 can be observed from 174 K, while the modes 2 and 3 appear below 150 K. In addition, one can notice a small mode at 49.2 cm^{-1} below 70 K, which is the acoustic spin singlet-triplet excitations (see Sec. 4.2).

The overall temperature dependence of the THz spectra is consistent with that of the phonon spectra, which indicates the existence of strong fluctuations in the temperature range $120 < T < 285$ K. There are several interesting features characterizing the modes 1 – 7: (i) These modes are not magnetic excitations related to the spin dimers. All the modes appear already at or above 100 K, much higher than the spin-dimerization temperature of 70 K. (ii) They are very unlikely pure phonon modes at low temperatures. These modes are broad at high temperatures, but extremely narrow below 100 K. Their linewidths (full width at half maximum) are less than 1 cm^{-1} at 4 K. One could infer that these modes are electronic or orbital excitations, or mixed phonon-orbital or vibronic excitations, since they evolve from phonons at high temperatures.

Due to the nuclei-electron interaction, the Cr 3*d* orbitals can be coupled to the

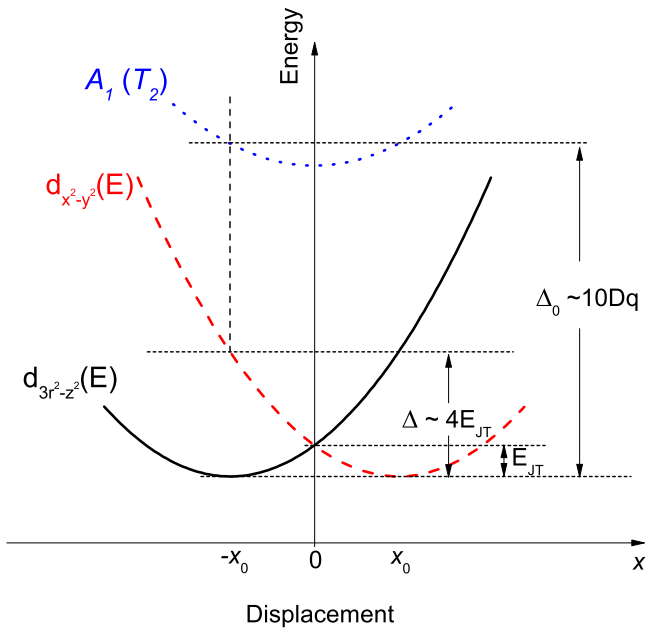

Figure 5.12: Illustration of the three lower-lying Cr orbitals modulated by the vibrational motion of the CrO_4 octahedra. The x-axis is a generalized coordinate of the CrO_4 octahedra. The Jahn-Teller energy E_{JT} and the orbital gap $\Delta \sim 4E_{JT}$ are given based on the Jahn-Teller model with linear vibronic coupling, see Sec. 2.1.10 for details. Δ_0 is the crystal field splitting, see also Fig. 4.6.

vibrations of Cr-O bonds. If we consider the simplest Jahn-Teller problem with only the linear vibronic coupling (see Sec. 2.1.10), modulation of the Cr orbitals by the vibrational motion of the CrO_4 octahedra is illustrated in Fig. 5.12. For the low-symmetry structure, the generalized coordinate $x = -x_0$ correspond to the equilibrium position of the CrO_4 octahedra, where the $d_{3z^2-r^2}$ is stabilized by the Jahn-Teller energy E_{JT} and the orbital gap Δ between the $d_{3z^2-r^2}$ and $d_{x^2-y^2}$ is exactly $4E_{JT}$ according to the model of linear vibronic coupling, see Sec. 2.1.10.[12]

Raman spectroscopy has also detected a mode at 71 cm^{-1} (see Fig. 5.7). This mode was suggested to be a mixed phonon-orbital excitation.[102] This mode probably becomes infrared active in the low-temperature phase, and is observed in the transmission spectra shown in Fig. 5.11. If we associate this mode with the Jahn-Teller energy, i.e. $E_{JT} = 71$ cm^{-1} then the orbital gap is about $4E_{JT} = 284$ $cm^{-1} \cong 409$ K, very close to the values of 430 K and 388 K, estimated by Raman [102] and ESR studies [99], respectively. The other modes 1 – 3 and 5 – 7 can be tentatively assigned to vibronic

modes.

5.3 Summary

Using infrared spectroscopy and specific heat measurement, the phononic and magnetic excitations as a function of temperature have been successfully determined and consistently analyzed for the isostructural chromium oxides $Sr_3Cr_2O_8$ and $Ba_3Cr_2O_8$ with the magnetic chromium ion Cr^{5+} ($3d^1, s = 1/2$). Although the two compounds crystallize in the same crystalline structure with the same symmetry group, they exhibit very different temperature dependent properties. $Ba_3Cr_2O_8$ is rather a conventional Jahn-Teller system: The single $3d$ electron of the chromium ion has a two-fold orbital degeneracy in an oxygen tetrahedron, which makes the system Jahn-Teller active. Below the Jahn-Teller transition temperature, $Ba_3Cr_2O_8$ undergoes a structural phase transition from the hexagonal phase to the monoclinic phase. The lattice symmetry is clearly broken at the transition temperature, and the orbital degeneracy is lifted with complete orbital ordering just below the transition. $Sr_3Cr_2O_8$ is a quite unusual Jahn-Teller system: On the one hand, the chromium ion plays the same role of an active Jahn-Teller center as in $Ba_3Cr_2O_8$. The lattice symmetry starts to be broken at the transition temperature of 285 K, manifested by a small anomaly in the specific heat and by the temperature evolution of the phonon spectrum. On the other hand, only below 100 K the long-range orbital order is fully established. Strong orbital fluctuations persist in the temperature range $100 < T < 285$ K. The nature of the strong fluctuation regime is not completely known. Further experimental and theoretical works are required to clarify this issue.

6 Magnetic Excitations in Spin Chain Systems

6.1 Single-ion anisotropy in $SrNi_2V_2O_8$

6.1.1 Introduction

The one-dimensional spin-1 system with nearest-neighbor Heisenberg antiferromagnetic exchange J exhibits a magnetic excitation gap, *i.e.* the Haldane gap, $\Delta = 0.41J$ between a nonmagnetic spin-singlet ground state and a magnetic spin-triplet excited state.[40, 41, 100] An ideal one-dimensional spin-1 system does not exhibit long-range order even at $T = 0$ K due to strong spin fluctuations, but in real systems long-range order can be established at finite temperature when sufficiently large inter-chain interactions exist. The effects of inter-chain exchange interactions $J_\perp$ and single-ion anisotropy D on the ground state and excitation gap have been extensively studied in various theoretical approaches. The magnetic excitation gap can be reduced or completely suppressed in the presence of inter-chain exchange interaction and single-ion anisotropy.[17, 75, 72, 82, 34]

The isotructural spin-chain compounds $ANi_2V_2O_8$ (A = Pb and Sr) based on Ni^{2+} ions with $S = 1$ have attracted considerable attention[92, 104, 89, 74, 88, 45, 11] because the excitation gap ($0.23J$ with $J = 8.2$ meV for A = Pb,[92] and $0.25J$ with $J = 9.2$ meV for A = Sr[11]) is significantly smaller than the expected $\Delta = 0.41J$. This indicates that these compounds are close to a phase boundary in the D–$J_\perp$ phase diagram.[82] $ANi_2V_2O_8$ crystallizes in tetragonal symmetry with space group $I4_1cd$, where the edge-shared NiO_6 octahedra surrounding the fourfold screw axis form screw chains along the c-axis [Figs. 6.1(a) and (b)].[11] By slightly doping the Ni-site or the A-site with nonmagnetic ions, the ground state changes from a disordered spin-liquid state to a Néel ordered state.[92, 89, 45] Nonmagnetic substitutions at the Ni-sites introduce free spins at the ends of spin chains. The coupling of these free spins due to inter-chain interaction can lead to the long-range magnetic order.[92] For the A-site doping the disorder-to-order transition has been ascribed to the modification on the inter-chain exchange interactions by substitutions.[45]

According to reports on powder samples,[92, 104] the ground state of $SrNi_2V_2O_8$ exhibits a three-dimensional ordered state below 7 K due to Dzyaloshinskii-Moriya interaction, which is different from the spin-liquid state of $PbNi_2V_2O_8$. Recently, nu-

clear magnetic resonance measurements performed on powder samples indicate that $SrNi_2V_2O_8$ is disordered down to 3.75 K.[74] The absence of an anomaly in the specific heat also rules out long-range order in $SrNi_2V_2O_8$ above 2 K.[45] The magnetic susceptibility of $ANi_2V_2O_8$ increases with decreasing temperature and exhibits a broad maximum around 130 K [see Fig. 6.1(c) for $SrNi_2V_2O_8$]. At low temperatures below 10 K, an upturn of the susceptibility has been observed due to a Curie-Weiss contribution of magnetic impurities in the sample.[92, 74, 45, 11] The susceptibility does not exhibit sharp anomalies down to 2 K, indicating the absence of long-range magnetic order.[74, 45, 11]

Based on a perturbative approach to describe inelastic neutron scattering results,[34] the single-ion anisotropy in $PbNi_2V_2O_8$ and $SrNi_2V_2O_8$ has been estimated as -0.45 and -0.56 meV, respectively.[104] An ESR study reported a smaller value of about -0.31 meV for $PbNi_2V_2O_8$,[88] in agreement with an estimate from magnetization measurements.

6.1.2 Spin excitation spectra

Electron paramagnetic resonance

Figures 6.2(a) and (b) show the transmission of $SrNi_2V_2O_8$ as a function of magnetic field measured at 155 GHz for various temperatures above 50 K for the applied magnetic field $\mathbf{H} \parallel c$ and $\mathbf{H} \parallel a$, respectively. At 207 K, a resonance mode is observed at 4.73 T for $\mathbf{H} \parallel c$ corresponding to an ESR signal of Ni^{2+}, as marked by the arrow in Fig. 6.2(a). The resonance field increases with decreasing temperature and reaches 5.27 T at 69 K. Below 50 K this mode cannot be resolved. As shown in Fig. 6.2(b), the resonance mode can be also observed above 50 K for $\mathbf{H} \parallel a$. The temperature dependence is consistent with results observed in the isostructural compound $PbNi_2V_2O_8$.[88] The transmission spectra as a function of magnetic field have been measured for $\mathbf{H} \parallel c$ and for $\mathbf{H} \parallel a$. Figure 6.2(c) shows the transmission spectra at 100 K at various frequencies with $\mathbf{H} \parallel a$, which reveal resonance modes as marked by the arrows. The observed resonance frequencies versus resonance magnetic fields at 100 K are shown in Fig. 6.2(d). The field dependence of the resonance frequencies exhibits a linear relation. The experimental data can be fitted by a linear function through the origin resulting in a g-factor of 2.24(3) for both field orientations. The line in Fig. 6.2(d) shows the fit result which is in good agreement with the experimental data. The obtained g-factor is consistent with $g = 2.23$ determined in $PbNi_2V_2O_8$,[88, 89] which is a typical value for Ni^{2+} in octahedral crystal fields.[2]

The intensity of the ESR modes shown in Figs. 6.2(a) and (b) increases slightly with decreasing temperature and then decreases significantly below 100 K. This is consistent with the temperature dependence of the magnetic susceptibility, which exhibits a broad maximum around 130 K [see Fig. 6.1(c)]. At low temperatures, the ESR modes are

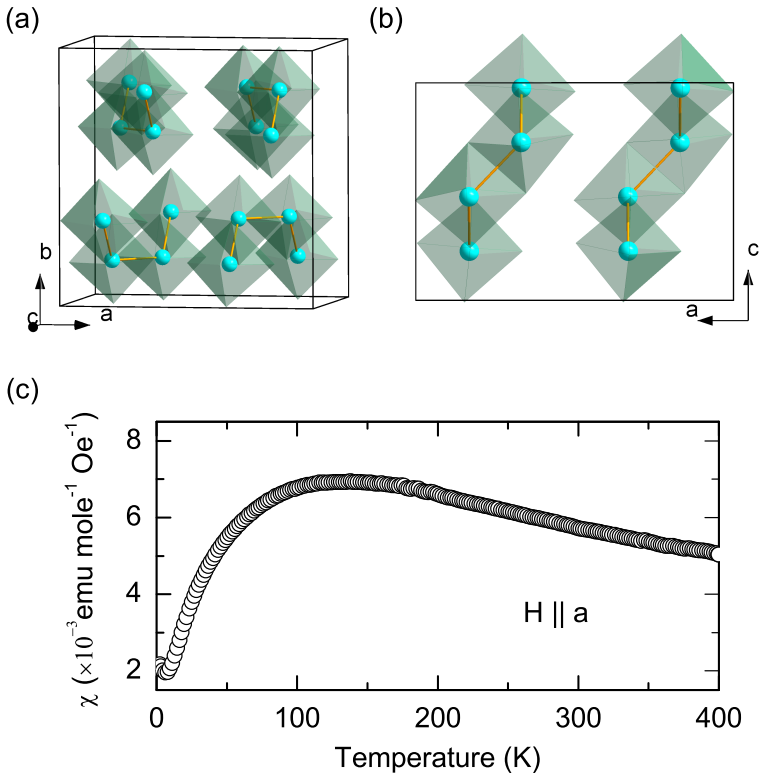

Figure 6.1: (a) Edge-sharing NiO_6 octahedra surrounding the fourfold screw axis forming spin chains along the c-axis in a unit cell of $SrNi_2V_2O_8$. Ni ions are shown by spheres. (b) Two spin chains along the c-axis. (c) Temperature dependence of the magnetic susceptibility measured at 1 T with the magnetic field parallel to the a-axis $\mathbf{H} \parallel a$.[95]

quite broad, have low intensity, and cannot be tracked below 50 K.

Intra-triplet spin excitation spectra

Figure 6.3(a) shows the transmission spectra of $SrNi_2V_2O_8$ at 250 GHz measured below 30 K for $\mathbf{H} \parallel a$. A new absorption mode around 5.5 T can be seen at 25 K. The resonance field of this mode decreases slightly with decreasing temperature. This mode cannot be resolved below 12 K and is assigned to a intra-triplet resonance mode of Ni^{2+} [see Fig. 6.3(b)]. At very low temperatures (below 12 K), the lower-lying triplet branch becomes much less populated due to the magnetic gap, therefore the intra-triplet excitations cannot be observed. Below 30 K, the splitting of the spin-triplet state has also been observed in inelastic neutron scattering experiments.[8]

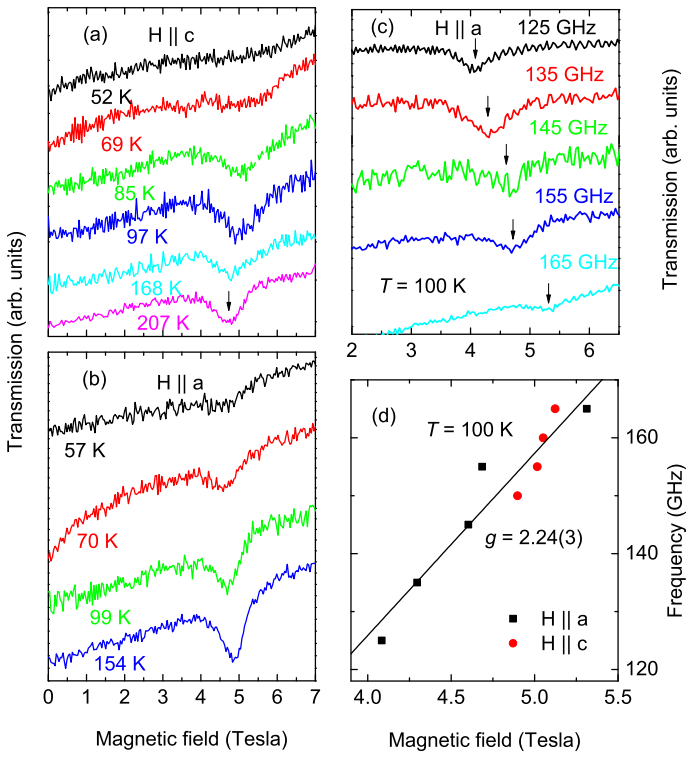

Figure 6.2: Transmission spectra of $SrNi_2V_2O_8$ at 155 GHz measured for various temperature with the magnetic field (a) parallel to the c-axis and (b) parallel to the a-axis. (c) Transmission spectra at various frequencies measured for 100 K with $\mathbf{H} \parallel a$. (d) Resonance frequency as a function of resonance field at 100 K. Linear fit gives a g-factor of 2.24(3).[95]

The transmission spectra at 250 GHz measured in the same temperature range for $\mathbf{H} \parallel c$ do not exhibit any mode, indicating significant single-ion anisotropy in this compound.[34, 88]

6.1.3 Discussion

The single-ion anisotropy contributes to the Hamiltonian in the form $D(S_i^z)^2$ with the anisotropy constant D, which gives rise to zero-field splitting of the spin-triplet state. Theoretically, an effective anisotropy $D_{eff} \equiv -1.98D$, corresponding to the intra-triplet splitting in spin-1 systems has been studied[34] and applied to explain the results of $PbNi_2V_2O_8$.[88] With the presence of single-ion anisotropy, the dependence of triplet states on the external magnetic field is quite different for $\mathbf{H} \parallel c$ and for $\mathbf{H} \parallel a$

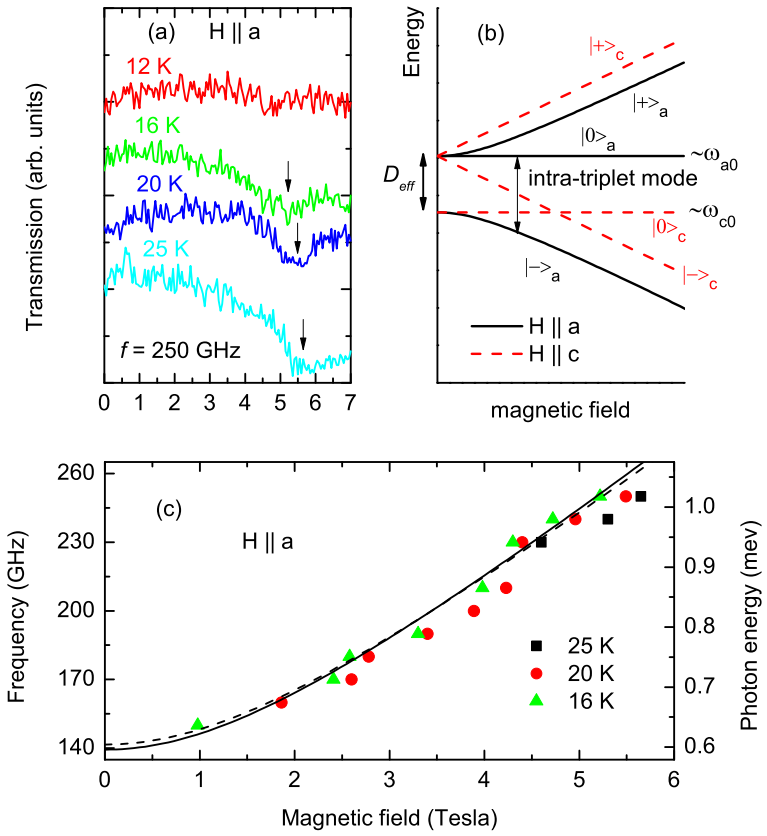

Figure 6.3: (a) Transmission spectra of $SrNi_2V_2O_8$ at 250 GHz measured at various temperatures with $\mathbf{H} \parallel a$. (b) Zeeman splitting of spin-triplet states with single-ion anisotropy $D < 0$ for $\mathbf{H} \parallel a$ (solid lines) and $\mathbf{H} \parallel c$ (dashed lines) according to a macroscopic field theory.[32, 88] (c) Resonance frequencies versus resonance magnetic fields determined from various spectra measured at various temperatures with $\mathbf{H} \parallel a$. The solid and dashed lines are fits to the experimental data at 16 K using the macroscopic field theory [Eq. (6.1)] and the perturbation approach [Eq. (6.2)], respectively. [95]

[see Fig. 6.3(b) for $D < 0$ (easy-axis type)].[34, 88] For $D_{eff} > 0$, we use $|-\rangle_a$ to denote the lower-lying state for $\mathbf{H} \parallel a$, the energy of which decreases with increasing magnetic field. The state, with energy independent on magnetic field for $\mathbf{H} \parallel c$, is denoted by $|0\rangle_c$, which has lowest energy when the magnetic field is smaller than 4.4 T (estimated from D_{eff}, see below). Consequently, the most probable intra-triplet excitations will be from $|-\rangle_a$ to $|0\rangle_a$ for $\mathbf{H} \parallel a$ and from $|0\rangle_c$ to $|\pm\rangle_c$ for $\mathbf{H} \parallel c$. With increasing magnetic field, the absorption mode corresponding to $|-\rangle_a \rightarrow |0\rangle_a$ for $\mathbf{H} \parallel a$ will gain intensity and shift to higher frequencies due to decreasing energy of the $|-\rangle_a$ state by the Zeeman contribution. However, the intensity corresponding to $|0\rangle_c \rightarrow |\pm\rangle_c$ is rather constant for $\mathbf{H} \parallel c$ since the population of the $|0\rangle_c$ state will not be influenced by the magnetic field.

The ESR results indicate that the single-ion anisotropy is of the single-axis type *i.e.*, $D < 0$, otherwise the excitations would be observed for $\mathbf{H} \parallel c$. Resonance frequencies versus resonance fields of the observed modes for $\mathbf{H} \parallel a$ are plotted in Fig. 6.3(c). Below 1 T, we cannot resolve any modes due to the low population of the $|-\rangle_a$ state. This is consistent with the fact that no modes corresponding to $|0\rangle_c \rightarrow |\pm\rangle_c$ can be resolved from the spectra for $\mathbf{H} \parallel c$, which should have lower intensity compared to $|-\rangle_a \rightarrow |0\rangle_a$ for $\mathbf{H} \parallel a$ in a finite magnetic field [see Fig. 6.3(b)]. According to the macroscopic field theory,[32, 88] the field dependence of the frequency difference between the states $|0\rangle_a$ and $|-\rangle_a$ for $\mathbf{H} \parallel a$ can be described by

$$\omega(H) = \sqrt{A + B} - \sqrt{(\gamma H)^2 + A - \sqrt{B^2 + 4A(\gamma H)^2}}, \tag{6.1}$$

where $\gamma = g\mu_B$ with μ_B the Bohr magneton, $A \equiv (\omega_{a0}^2 + \omega_{c0}^2)/2$ and $B \equiv (\omega_{a0}^2 - \omega_{c0}^2)/2$ with ω_{a0} the eigenfrequency of the $|0\rangle_a$ state for $\mathbf{H} \parallel a$ and ω_{c0} the eigenfrequency of the $|0\rangle_c$ state for $\mathbf{H} \parallel c$ [see Fig. 6.3(b)]. Using perturbation theory,[34] the field dependence has been shown to follow the expression

$$\omega(H) = \frac{1}{2}\left[\omega_{a0} - \omega_{c0} + \sqrt{(\omega_{a0} - \omega_{c0})^2 + 4(\gamma H)^2}\right]. \tag{6.2}$$

As shown by the solid line and dashed line in Fig. 6.3(c), respectively, both fits with Eq. (6.1) and Eq. (6.2) to the experimental data at 16 K provide a good description of the experimental results, where we use the experimental g-factor of 2.24. The fits according to the macroscopic field theory [Eq. (6.1)] and perturbative theory [Eq. (6.2)] determine the intra-triplet splitting $\omega_{a0} - \omega_{c0}$ of 139 GHz and 141 GHz at zero magnetic field, respectively, which agree well with each other within experimental uncertainty. The intra-triplet splitting corresponds to $D_{eff} = 0.57$ meV. The single-ion anisotropy D can be consequently estimated as -0.29 meV, which is smaller than -0.4 meV determined at 16 K by inelastic neutron scattering experiments.[8]

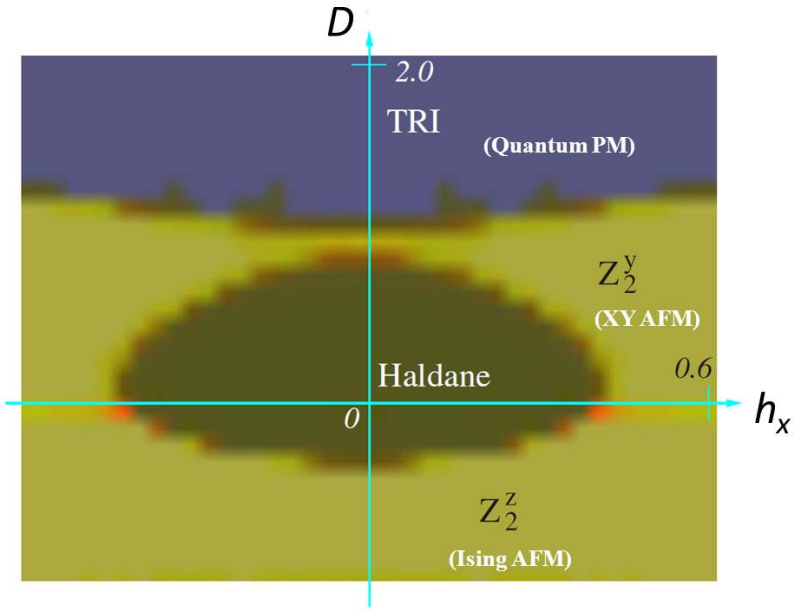

Figure 6.4: $D - h_x$ phase diagram of the spin-1 antiferromagnetic chain model in Eq. (6.3) for the inter-chain coupling $J = 0$. Ising and XY antiferromagnetic orders can be stabilized by the inter-chain coupling (see Fig. 2.8). Paramagnetic and antiferromagnetic phases are denoted by PM and AFM, respectively. Adapted from Ref. [38].

6.2 Field induced disorder-order transition in $SrNi_2V_2O_8$

6.2.1 Introduction

Quantum phase transitions in the spin-1 Heisenberg antiferromagnetic chain systems can be induced by applying magnetic field. In a transverse magnetic field, the Zeeman interaction should be considered in addition to the Hamiltonian in Eq. (2.41),

$$\hat{H} = \sum_{<i,j>_{\parallel}} \mathbf{S}_i \mathbf{S}_j + J \sum_{<i,j>_{\perp}} \mathbf{S}_i \mathbf{S}_j + D \sum_i (S_i^z)^2 + h_x \sum_{i=1}^{N} S_i^x, \tag{6.3}$$

where h_x is the reduced Zeeman energy for the transverse magnetic field. Gu and Wen have investigated the $D - h_x$ phase diagram of this model without the inter-chain coupling J in Ref. [38]. The phase diagram is shown in Fig. 6.4. At zero field, this model exhibits the Haldane, Ising antiferromagnetic, XY antiferromagnetic, or quantum paramagnetic phases depending on the single-ion anisotropy, consistent with the

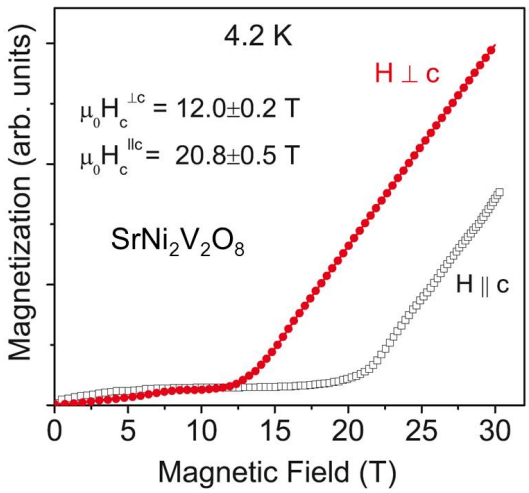

Figure 6.5: High field magnetization of $SrNi_2V_2O_8$ at 4.2 K for transverse ($\mathbf{H} \perp c$) and longitudinal ($\mathbf{H} \parallel c$) magnetic field. Adapted from Ref. [8].

phase diagram shown in Fig 2.8. The transverse magnetic field could induce quantum phase transition from the Haldane phase to the Ising or XY antiferromagnetic phase and also from the quantum paramagnetic phase to the XY antiferromagnetic phase. The quantum phase transition from the Haldane phase and Ising antiferromagnetic phase is expected for $SrNi_2V_2O_8$, since $SrNi_2V_2O_8$ lies close to the phase boundary. Figure 6.5 shows the magnetization as a function of magnetic field at 4.2 K reported by A. Bera et al.[8] Finite magnetization is induced at 12.0 T and 20.8 T for transverse ($\mathbf{H} \perp c$) and longitudinal ($\mathbf{H} \parallel c$) magnetic field, respectively. This indicates that phase transitions are induced at the critical fields.

6.2.2 High field magnetic excitations

Figure 6.6 shows the transmission spectra measured in transverse magnetic fields up to 30 T at 1.5 K in the High Field Magnetic Laboratory in Nijmegen. One can find four absorption modes that are dependent on the magnetic field, as marked by the arrows. The two-lower lying modes can be observed only above the critical field of 12 T, while the other two modes appear even at zero field with eigenfrequencies of 36 cm^{-1} ($\cong$ 4.5 meV) and 50 cm^{-1} ($\cong$ 6.2 meV), respectively.

Field dependence of eigenfrequencies of the four magnetic excitations is shown in Fig. 6.7. In the Haldane phase below 12 T, the 36 cm^{-1} mode hardens slightly with increasing magnetic field, while the 50 cm^{-1} mode is almost field-independent. The energies of these two modes increase strongly with field above 12 T in the Ising antiferromagnetic phase. There are two modes emergent at the phase transition. The

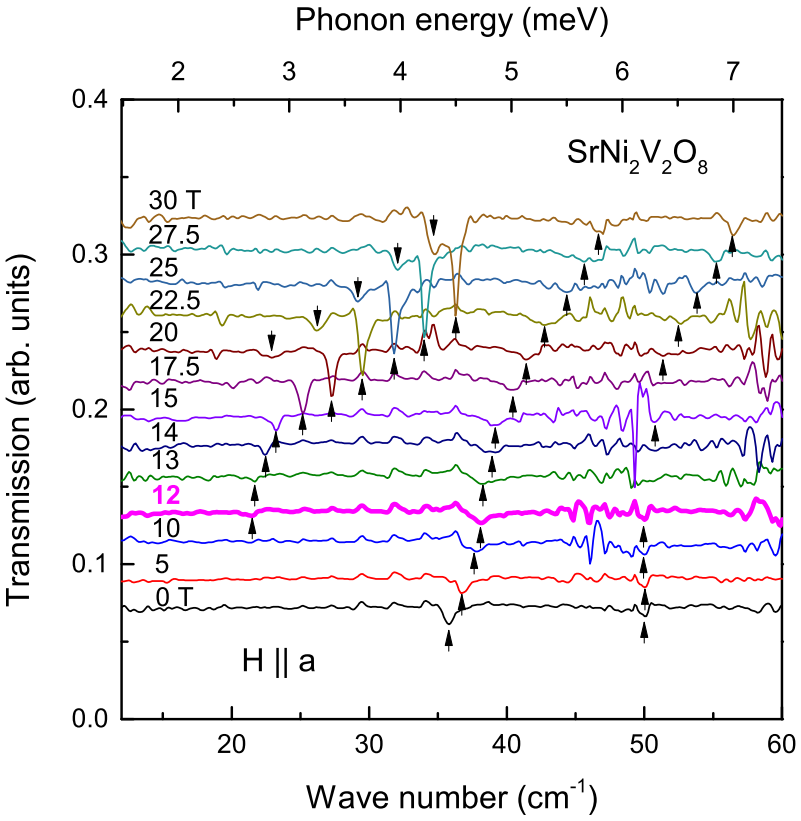

Figure 6.6: High field transmission spectra of $SrNi_2V_2O_8$ measured in various transverse magnetic fields up to 30 T at 1.5 K. The measurements were performed in the High Field Magnetic Laboratory in Nijmegen. Evolvement of four absorption modes is indicated by the arrows.

energies of both modes increases with increasing magnetic field. The lower-lying one exhibits clear linear dependence on the magnetic field. Extrapolation of the linear field dependence of its eigenfrequency goes to the origin, indicating that this mode is gapless at zero field. The solid line in Fig. 6.7 is a fit to this linear dependence. Assuming a magnetic-dipole excitation with $\Delta S = 1$, a g-factor of 2.49 is obtained. This value is slightly larger than that at 100 K. The other mode emergent with eigenfrequency of 20 cm^{-1} ($\cong$ 2.5 meV) is a gapped mode. This energy is consistent with the observed excitation energy of the $S_z = 0$ spin-triplet state by neutron inelastic scattering measurements. Thus, this mode can be associated to the excitation from the ground state to the $S_z = 0$ spin-triplet state in the Ising antiferromagnetic phase.

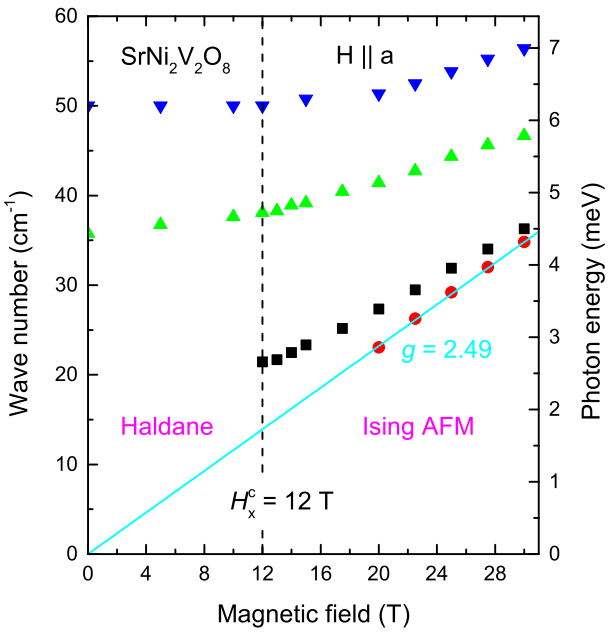

Figure 6.7: Energies of the magnetic excitations in $SrNi_2V_2O_8$ as a function of transverse magnetic field below and above the phase transition at 12 T.

6.3 Confined spinon excitations in $SrCo_2V_2O_8$

6.3.1 Introduction

The concept of creating new particles by confinement of sub-particles has been popularized since long in particle physics.[71] In the theory of strong interactions, baryons and mesons are produced by quark confinement. Two quarks in a meson are hold together by the Yang-Mills gauge field, of which the quanta are called gluons. Gluon-gluon interactions play a role as 'string' between quarks. Quarks are 'asymptotically free' at shorter distance and they cannot appear as individual particles, because an effective potential generated by the finite string tension increases progressively with increasing distance. A condensed-matter analogue of quasiparticle confinement can be realized in quantum magnets.[63] In a spin-1/2 ladder system with each ladder constituted by two weakly coupled antiferromagnetic chains, magnetic excitations on each chain are spinons, each carrying spin $S = 1/2$. Asymptotically free spinons are observed at high energy transfers, while bound states of spinons with spin $S = 1$ are observed at lower energies in the inelastic neutron experiments.[63] A simpler illustration of the spinon-confinement picture can be given in the weakly-coupled Ising-like spin-1/2 chain system $SrCo_2V_2O_8$.

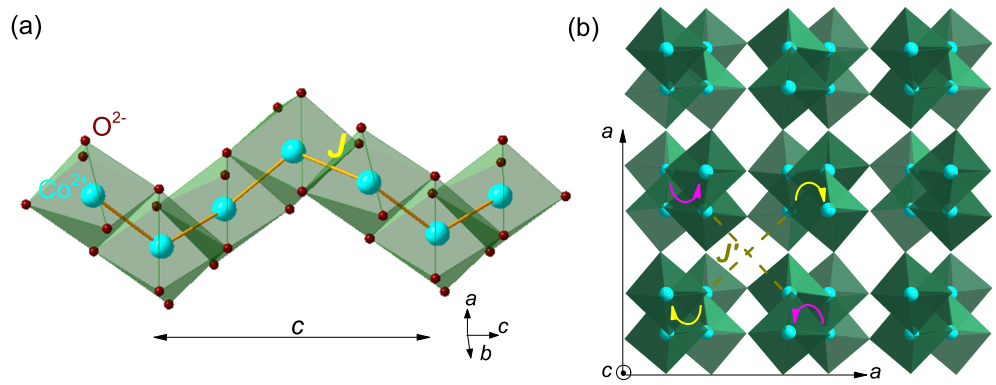

Figure 6.8: (a) Screw chain consisting of CoO_6 octahedra running along the crystalline c axis in $SrCo_2V_2O_8$. (b) Projection of left- and right-handed screw chains in the tetragonal ab plane. inter-chain exchange interaction is dominated by the antiferromagnetic interaction J' between the nearest neighboring Co ions in the ab plane with a Co-Co distance of 5.91 Å. These Co ions are from the neighboring chains with the same chirality.

The screw spin chains in $SrCo_2V_2O_8$ consist of edge-sharing CoO_6 octahedra, with Co^{2+} the only magnetic ions. The chains are either left-handed or right-handed and propagate along the crystalline c axis, as shown in the Fig. 6.8(a) and Fig. 6.8(b).[9, 44] The intra-chain exchange interaction J is the dominant magnetic interaction, while inter-chain couplings are much weaker. There are several inter-chain couplings mediated by different exchange paths. The dominant inter-chain couplings are the antiferromagnetic exchange interactions J' between nearest-neighbor Co ions in the ab plane, which belong to the neighboring chains with the same chirality.[52, 9, 36] Long-range collinear antiferromagnetic order is stabilized below $T_N = 5$ K by the weak inter-chain couplings, as shown in Fig. 6.10.[9]

Significant Ising-like anisotropy is usually achieved by cooperative effects of crystal field splitting and spin-orbit coupling. The spin-orbit coupling entangles orbital with the spin degrees of freedom and makes the total angular momentum a conserved quantity to describe the exchange interactions. According to Hund's rules, a free Co^{2+} ion with seven electrons in the atomic $3d$ orbital has a ground state with total orbital angular momentum $l = 3$ and spin $S = 3/2$. The seven-fold degenerate orbital levels ^4F are split into one orbital singlet $^4A_2$ and two orbital triplets $^4T_1$ and $^4T_2$ in the octahedral crystal field, as sketched in Fig.6.9.[66, 3] The orbital triplet $^4T_1$ is the lowest in energy with an effective orbital momentum $l = 1$. Considering in addition the four-fold spin multiplicity, the twelvefold entangled spin-orbit levels are further split into a lowest-lying Kramers doublet, a quartet, and a sextet due to spin-orbit

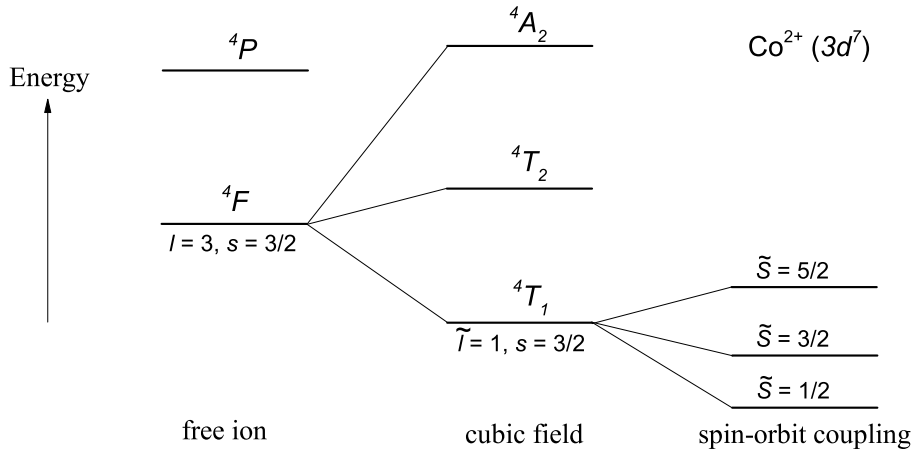

Figure 6.9: Schematic splitting of the energy levels of the Co^{2+} ($3d^7$) ion in $SrCo_2V_2O_8$. According to Hund's rules, ^4F is the lowest level for the ions with seven $3d$ electrons. It splits into a lower-lying orbital triplet $^4T_1$, an intermediate triplet $^4T_2$, and a higher-lying singlet $^4A_2$. Due to spin-orbit coupling, the lower-lying triplet $^4T_1$ splits further into a lower-lying spin-orbit doublet with $\tilde{S} = 1/2$, a quartet with $\tilde{S} = 3/2$, and a sextet with $\tilde{S} = 5/2$.[3, 66]

coupling.[2] The Kramers doublet protected by time-reversal symmetry is the ground state with total angular momentum, noted as *pseudospin*, $\tilde{S} = 1/2$.

The exchange interactions between the pseudospins in the chains of $SrCo_2V_2O_8$ can be modeled by the Ising-Heisenberg Hamiltonian[16]

$$\hat{H} = J \sum_i [\tilde{S}_i^z \tilde{S}_{i+1}^z + \epsilon(\tilde{S}_i^x \tilde{S}_{i+1}^x + \tilde{S}_i^y \tilde{S}_{i+1}^y)], \tag{6.4}$$

where $J > 0$ is the nearest neighbor antiferromagnetic exchange interaction, and $0 < \epsilon < 1$ takes into account the Ising-like anisotropy arising from the distortion of the CoO_6 octahedron.

6.3.2 THz time domain spectra

In Fig. 6.11(a) shows the electric-field amplitude of the transmitted electromagnetic wave through a reference and a $SrCo_2V_2O_8$ sample as a function of time delay in the magnetically ordered phase at 3.4 K. The incident light propagating along the crystalline a axis ($k \parallel a$) is polarized with the ac electric field parallel to the c axis ($e^\omega \parallel c$) and the ac magnetic field parallel to the a axis ($h^\omega \parallel a$). The transmission

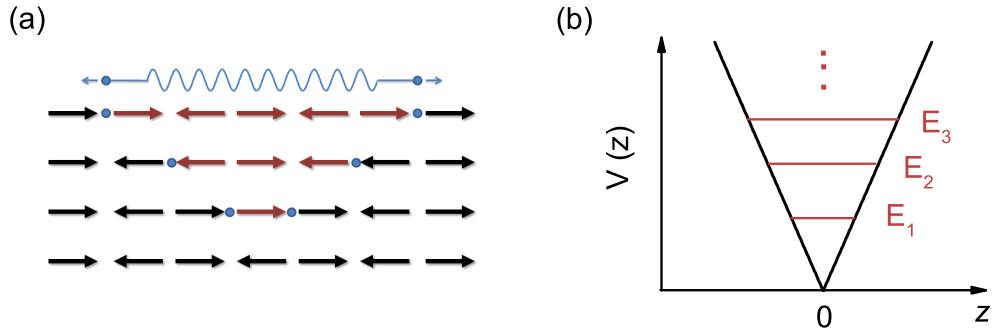

Figure 6.10: (a) Collinear antiferromagnetic order along the c axis stabilized below $T_N = 5$ K in $SrCo_2V_2O_8$.[9] Magnetic excitations of spinon-pairs with total pseudospin $\tilde{S} = 1$ corresponding to 1, 3, and 5 (odd number) of pseudospin-1/2 flips. In the antiferromagnetic phase, the two spinons are bound by inter-chain couplings. (b) Quantized spinon-pair excitation levels due to linear confinement imposed by inter-chain exchange interaction.

spectrum in the frequency domain [Fig. 6.11(b)] is obtained by Fourier transformation of the time-domain signal. From the power spectrum measured below T_N, one can notice an absorption line at about 0.35 THz marked as E_1. This absorption line is not observed above T_N. Figure 6.11(c) shows the power spectrum at 6.5 K right above T_N divided by the one measured at 3.4 K. One can readily observe the sharp line E_1 followed by a series of absorption lines E_2,E_3,...,E_9 with increasing energies. These absorption lines are not observed when the ac magnetic field is parallel to the spin direction ($h^\omega \parallel c$). This points to the magnetic nature of the absorption modes. These modes can be assigned to magnetic excitations also based on their dependence on external magnetic field as discussed in the following.

6.3.3 Multifrequency electron spin resonance spectra

The transmission spectrum of monochromatic THz light is measured at 2 K as a function of applied magnetic field along the chain direction, which is also the direction of the Ising-like spins in the magnetically ordered phase.[9] Typical spectra are shown in Fig. 6.12(a). Several absorption modes can be observed at the resonance fields in the spectrum of each frequency. The resonance magnetic fields shift with frequencies of the electromagnetic waves. The absorption frequencies versus corresponding resonance magnetic fields are plotted in Figure 6.12(c). One can clearly recognize a series of absorption modes, which are split in magnetic field, with energies increasing or decreasing with increasing magnetic field. All the lines follow a linear field dependence that can be described by a Zeeman interaction term $\pm g_{\parallel}\mu_B H\tilde{S}$ with a unique g-factor

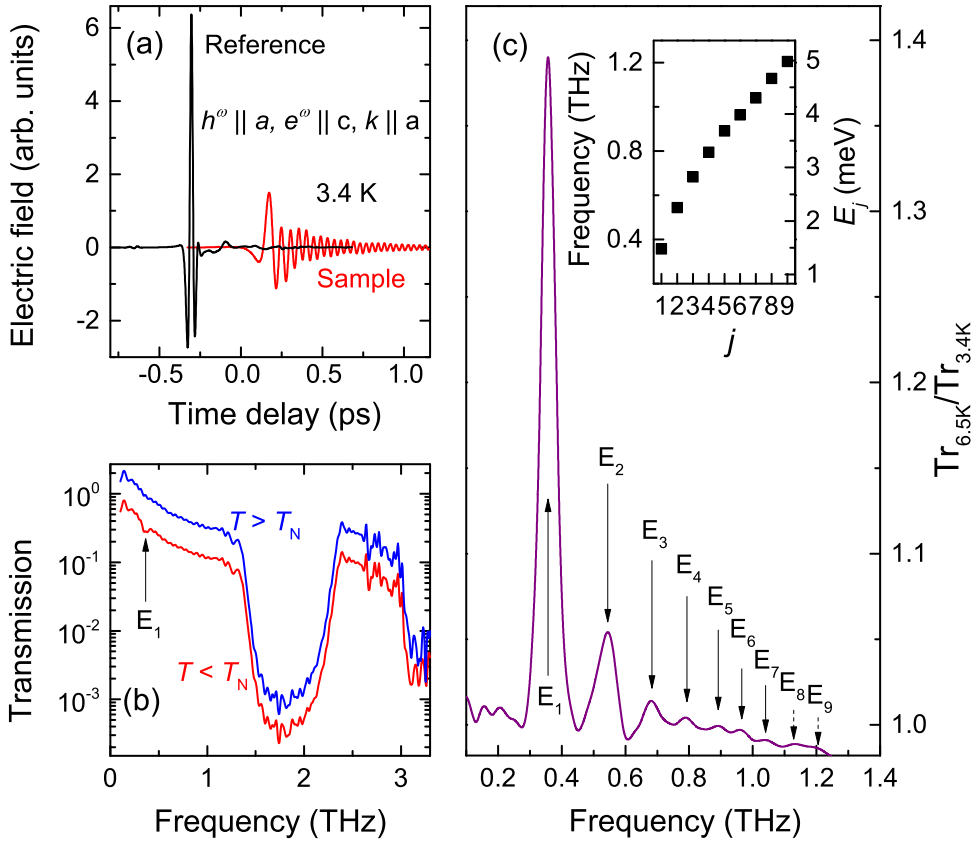

Figure 6.11: (a) THz time domain signals of a reference and a $SrCo_2V_2O_8$ sample measured at 3.4 K with the *ac* magnetic field $h^\omega \parallel a$, the electric field $e^\omega \parallel c$, and the wavevector $k \parallel a$. (b) Transmission spectrum below and above T_N in the THz spectral range obtained from Fourier transformation of the time domain signal. The spectrum measure above T_N is shifted upward for clarity. A dip corresponding to E_1 is marked in the spectrum measured below T_N. The spectral range from 1.3 to 2.3 THz and above 3 THz is dominated by broad phonon bands. (c) Ratio of transmission as obtained at 6.5 K and 3.4 K as a function of frequency below the phonon band. Nine peaks can be observed and are indexed from E_1 to E_9. Excitation energy E_j versus energy level index $j = 1, 2, 3, ...$ are shown in the inset.[96]

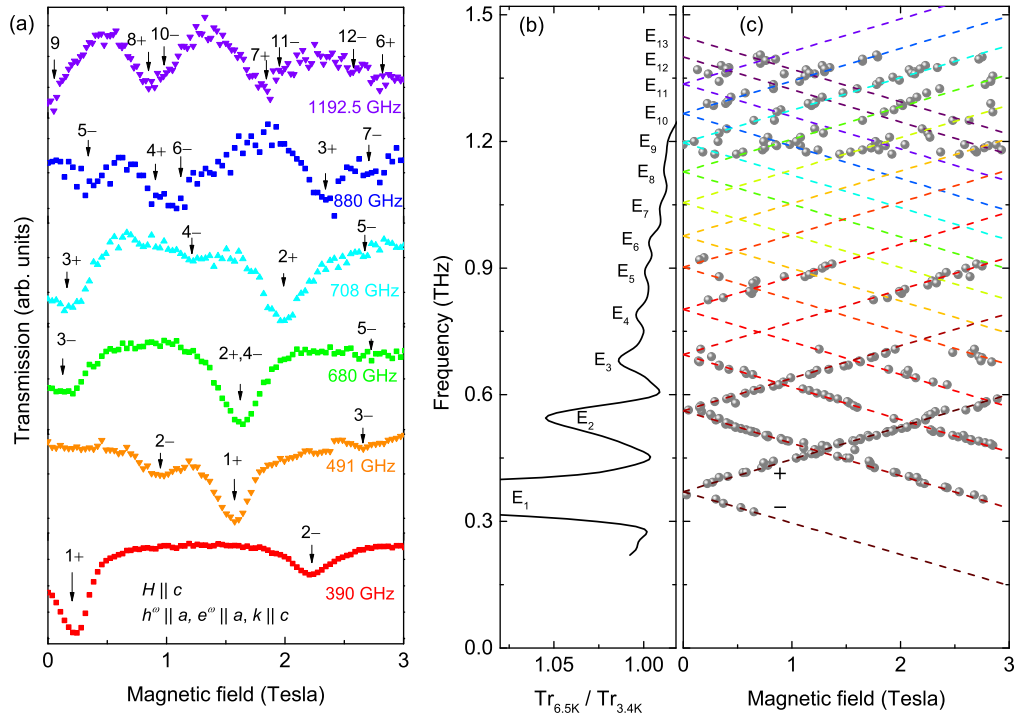

Figure 6.12: (a) Transmission spectra of $SrCo_2V_2O_8$ at various frequencies as a function of a longitudinal magnetic field at 2 K. Absorption modes are marked by the corresponding number of energy level in Fig.(b). (b) Normalized transmission spectrum at zero field adapted from Fig. 6.11(c). (c) Energies of absorption modes as a function of applied longitudinal magnetic field. Their field dependence can be described by linear Zeeman term with a single g-factor $g_{\parallel} = 5.5$ (see text).[96]

$g_{\parallel} = 5.5$, μ_B being the Bohr magneton, H the applied longitudinal magnetic field, and the total pseudospin $\tilde{S} = 1$. Plus or minus signs correspond to split modes in magnetic field, and are also used to label the modes in Fig. 6.12(a) and Fig. 6.12(c). The zero-field energies obtained by extrapolating the linear field dependence to zero field are shown in Fig. 6.13. The zero-field spectrum of Fig. 6.11(c) is shown in Fig. 6.12(b) for comparison. The agreement in the energies for all observed excitations is clearly documented.

The observed magnetic excitations below T_N exhibit clear hierarchical features: the intensity of the lines decreases with increasing energy; the energy difference between neighboring excitations decreases with increasing energy [see Fig. 6.11(c) and its inset].

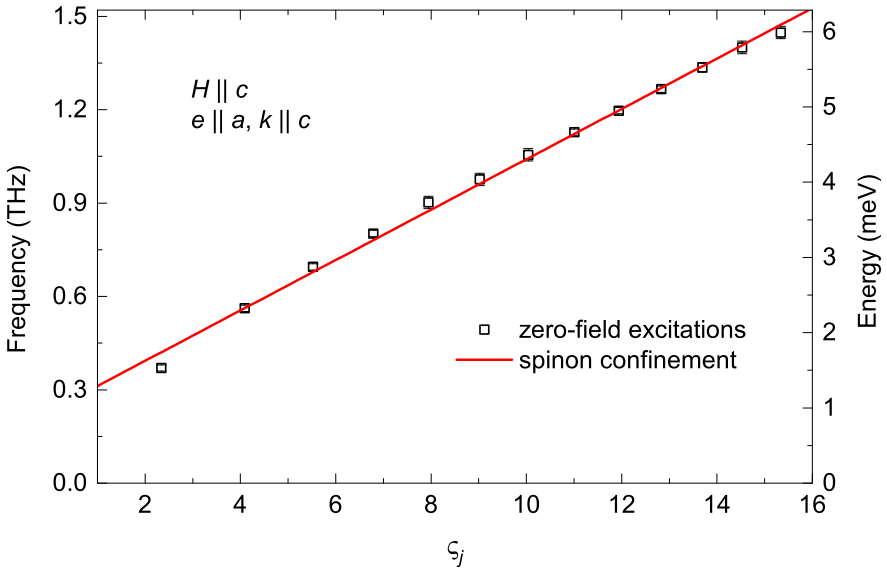

Figure 6.13: Hierarchy of the excitation energies at zero field can be modeled by the one dimensional Schrödinger equation with linear confinement [Eq. (6.3.4)]. $\zeta_j = 2.338, 4.088, 5.520, ...$ $(j = 1, 2, 3, ...)$ are the negative zeros of the Airy function [Eq. (2.54)].[96]

These are exactly the features predicted by the theory for spinon bound states due to confinement.[86] The excitations are indeed the spinon-pair excitations with total pseudospin $\tilde{S} = 1$, as confirmed by their field dependence. Every spinon-pair excitation is doubly degenerate in zero field, and the degeneracy is lifted in a finite longitudinal external magnetic field [Fig. 6.12(b)(c)]. Energies of the non-degenerate spinon-pair excitations increase or decrease depending on whether the total pseudospin is parallel or antiparallel to the external field, respectively.

6.3.4 Discussion

The $\tilde{S} = 1$ spinon-pair bound-states correspond to an odd number of pseudospin flips between the spinons as illustrated in Fig. 6.10(a). The other series of spinon-pair excitations with $\tilde{S} = 0$ observed by neutron scattering experiments [36, 10] are not observed in the THz measurements [see Fig. 6.12(c)]. This confirms the magnetic dipole active nature of the $\tilde{S} = 1$ spinon-pair excitations. For a spinon pair, the relative motion of one spinon with respect to the other along the chain can be described by

the one-dimensional Schrödinger equation

$$-\frac{\hbar^2}{\mu}\frac{d^2\varphi}{dz^2} + \lambda|z|\varphi = (E - 2E_0)\varphi \tag{2.52}$$

with a linear potential $\lambda|z|$ taking into account the confinement imposed by the inter-chain antiferromagnetic exchange interaction J' [Fig. 6.8(b), Fig. 6.10(b)], i.e., $\lambda = 2J'\langle\tilde{S}_z\rangle^2/c$ with c being the lattice constant along the chain direction [Fig. 6.8(a)]. Since the Γ point is probed by THz spectroscopy, a quadratic dispersion relation at the Γ point has been assumed, following the calculations of the two-spinon dynamic structure factor, as given by Eq. (2.51) and shown in Fig. 2.10.[18] This is also confirmed by inelastic neutron scattering experiments performed by Bera et al.[10]

The solution of Eq. (2.52) predicts a linear dependence of spinon-pair eigenenergies E_j on the negative zeros of the Airy function ζ_j, as given in Eq. (2.54). As shown in Fig. 6.13, the energies of the spinon-pair bound-states in $SrCo_2V_2O_8$ at zero field exhibit a linear dependence on ζ_j . The solid line in Fig. 6.13 is obtained by fitting the experimental results by Eq. (2.54). One can see that the energy hierarchy of the spinon-pair bound-states is nicely modeled using $2E_0 = 0.96$ meV and $\lambda^{2/3}(\frac{\hbar^2}{\mu})^{1/3} = 0.33$ meV.

The energy threshold $2E_0$ is significantly smaller than the pure Ising-limit $J = 60$ K $\simeq 5.17$ meV, which can be obtained by fitting the magnetic susceptibility using the Ising model.[9, 16] The fact that $2E_0 \ll J$ is a consequence of the finite ϵ term in Eq. (6.4).[46, 18] The deviation of ϵ from 1 is a measure of the anisotropy arising from distortions of the CoO_6 octahedra, which is also reflected by the $g_\parallel$ factor. If we assume a trigonal distortion with strength δ,[3, 66] then the induced anisotropy depends on the renormalized parameter δ/Λ with $\Lambda < 0$ being the spin-orbit coupling. The obtained value of $g_\parallel = 5.5$ corresponds to $\delta/\Lambda = -0.80$ and $\epsilon = 0.73$.[66] A smaller value of $\epsilon = 0.41$ in $BaCo_2V_2O_8$ indicates a larger distortion of the CoO_6 octahedra.[66, 36] This is also indicated by a larger value of $g_\parallel = 6.2$ and a larger excitation gap of 1.7 meV in $BaCo_2V_2O_8$ with a similar intra-chain exchange interaction.[56, 66, 46, 44, 9]

Spinon bound states in the quasi-one-dimensional antiferromagnets $SrCo_2V_2O_8$ and $BaCo_2V_2O_8$ can be classified by their pseudospins which are either $\tilde{S} = 1$ or $\tilde{S} = 0$, analogous to the classification of mesons (quark-antiquark bound states) by their isospins (either 1 or 0). This is in clear distinction to the quasi-one-dimensional ferromagnet $CoNb_2O_6$ where the pseudospin is not a conserved quantity, since more spins are flipped at higher energies. Even at a certain energy level, spin blocks (domains) with different lengths in $CoNb_2O_6$ tend to flip with comparable probablities.[70]

In the strong interaction scenario, the strings between quarks can snap and heavy hadron particles are expected to decay into lighter ones, when creating heavier particles is energetically less favorable. Analogous to this scenario, spinon bound states can be expected only up to an energy of $E_1 + E_1$, above which an energy continuum would appear, as reported in $CoNb_2O_6$.[70] This continuum is surprisingly not observed in $SrCo_2V_2O_8$ or in $BaCo_2V_2O_8$ up to the energy much higher than $E_1 + E_1$. This

difference is possibly due to the different strengths of spinon-spinon interactions in the two systems. The corresponding parameter $\lambda/\sqrt{\mu}$ in $SrCo_2V_2O_8$ is larger by one order of magnitude than in $CoNb_2O_6$. The $E_1 + E_1$ states with pseudospin $\tilde{S} = 2$ and any other bound states created by higher-order confinement processes with larger pseudospins, such as bound states of E_1 states in neighboring chains,[70] can be excluded in $SrCo_2V_2O_8$ as documented in Fig. 6.12(c), because a stronger field dependence expected for these states is absent.

6.4 Field induced order-disorder transition in $SrCo_2V_2O_8$

6.4.1 Phase diagram of XXZ antiferromagnetic chain

The ground state of the weakly coupled XXZ antiferromagnetic chain system can be tuned by applying an external magnetic field. In a longitudinal magnetic field, the ground state can be either a Néel ordering phase, a spin-liquid phase, or a field induced ferromagnetic phase.[39, 15, 55] Figure 6.14 shows the h–ϵ phase diagram of the ground state of the quasi-one-dimensional XXZ antiferromagnetic chain system. $h = g\mu_B H/J$ is the longitudinal magnetic field H reduced by the intra-chain exchange interaction J. In the Ising-like case ($\epsilon < 1$), the long-range Néel order can be completely suppressed by the longitudinal magnetic field. Thus, a quantum phase transition to a Tomonaga-Luttinger spin-liquid phase is induced.[39, 15, 55] In the spin liquid phase, transverse and longitudinal spin components have different correlations. Asymptotic forms of the transverse and longitudinal correlation functions are given by

$$\langle S_0^x S_r^x \rangle \simeq (-1)^r r^{-\eta_x}, \tag{6.5}$$

$$\langle S_0^z S_r^z \rangle - m^2 \simeq \cos(2k_F r) r^{-\eta_z}, \tag{6.6}$$

where m is the magnetization per spin, η_x and η_z are the Tomonaga-Luttinger exponents for the x and z spin component, respectively, which satisfy a relation $\eta_x \eta_z = 1$ and $k_F = \pi(1/2 - m)$. $2k_F = \pi(1 - 2m)$ is the incommensurate wave vector, where gapless excitations are induced by external longitudinal magnetic field.[56]

6.4.2 High field magnetization

Figure 6.15 shows the magnetization as a function of the longitudinal magnetic field in $SrCo_2V_2O_8$ measured at 1.7 K. Field induced phase transitions are clearly manifested by the anomalies in the derivatives of the magnetization with respect to magnetic field. The finite magnetization appears above $H_c = 4$ T corresponding to the phase transition from the collinear phase to the spin-liquid phase. The magnetization increases monotonically with increasing magnetic field. An abrupt increase of magnetization occurs at $H^* = 25.2$ T with half of the saturation value that is reached at $H_s = 28.7$ T. The

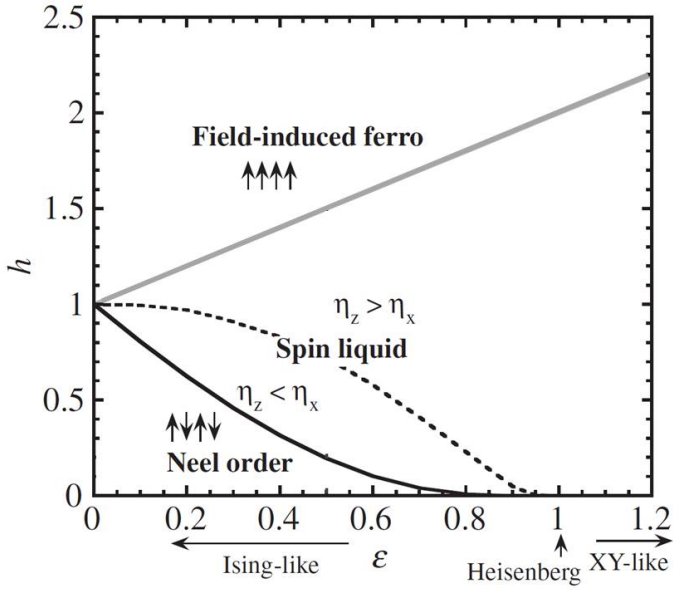

Figure 6.14: h–ϵ diagram of the ground state of the quasi-one-dimensional XXZ antiferromagnetic chain. $h = g\mu_B H/J$ is the longitudinal magnetic field H reduced by the intra-chain exchange interaction J. This figure is adapted from Ref. [55].

field dependence of the magnetization is very similar to that in $BaCo_2V_2O_8$.[56, 55] In $BaCo_2V_2O_8$, $H_c = 3.9$ T is very close to the value in $SrCo_2V_2O_8$. The other two critical fields in $BaCo_2V_2O_8$ are $H^* = 19.5$ T and $H_s = 22.7$ T, which are much smaller than those in $SrCo_2V_2O_8$. According to the phase diagram in Fig. 6.14, the saturation field is proportional to the value of ϵ,[15] so this indicates that the value of ϵ in $BaCo_2V_2O_8$ is smaller, while the intra-chain nearest-neighbor exchange interactions are comparable for both systems.[16, 44, 9] Using density matrix renormalization group calculation, Kimura *et al* simulated the field dependence of the magnetization in $BaCo_2V_2O_8$ and determined $\epsilon = 0.46$.[56] This value is consistent with $\epsilon = 0.41$ determined from neutron scattering experiments.[36] It is indeed smaller than $\epsilon = 0.73$ in $SrCo_2V_2O_8$ from our estimation given in the previous sections.

6.4.3 Magnetic excitations in spin-liquid phase

Figure 6.16(a) shows the transmission spectra of monochromatic radiation for various low frequencies as a function of the longitudinal magnetic field up to 7 T at 2 K. Besides the spinon-pair excitations, three other modes named by $\boldsymbol{B}$, $\boldsymbol{P}$, and $\boldsymbol{Q}$ are observed at higher magnetic fields. Field dependencies of the observed modes up to 7 T are shown

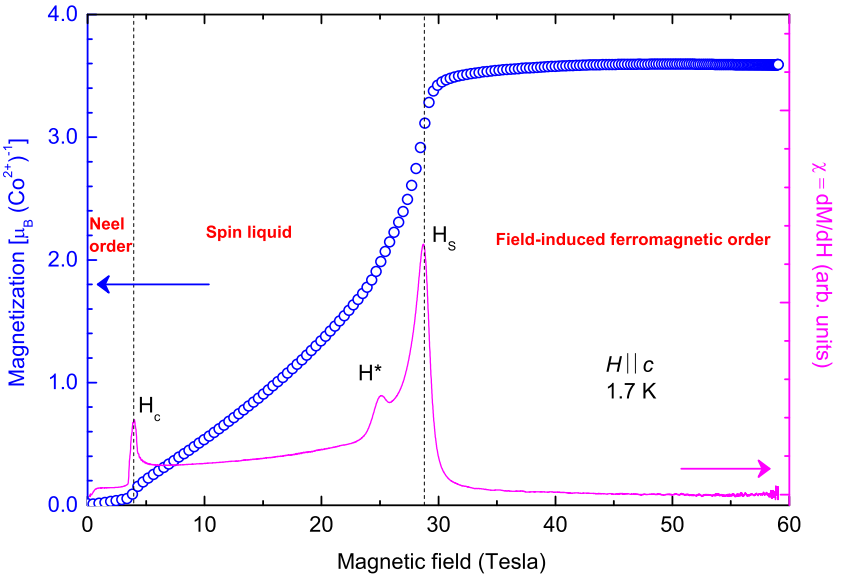

Figure 6.15: Magnetization (left coordinate) and its field derivative (right coordinate) of $SrCo_2V_2O_8$ as function of applied longitudinal magnetic field, i.e. $H \parallel c$, up to 60 T at 1.7 K. At low temperature $SrCo_2V_2O_8$ has a long-range antiferromagnetic order (Néel order) below $H_c = 4$ T. Transition to quantum-disordered spin-liquid phase is induced at $H_c = 4$ T with onset of finite magnetization. Ferromagnetic order is induced by the magnetic field at $H_s = 28.7$ T with the saturation of the magnetization. The small anomaly in the dM/dH curve at $H^* = 25.2$ T corresponds to the abrupt increase of magnetization, where half of the saturated magnetization is reached. The magnetization measurements were performed by A. K. Bera and J. M. Law in the Dresden High Magnetic Field Laboratory.

in Fig. 6.16(b). The linear field dependence of the spinon-pair excitations is plotted by the dashed lines following Fig. 6.12(c). The observed field dependence deviates clearly from a linear dependence when the magnetic field is close to the critical field $H_c = 4$ T. This reflects the strong quantum fluctuations at H_c, where the Zeeman interaction suppresses the inter-chain coupling and induces an order-disorder transition.

The magnetic excitations are further investigated in an extended frequency range and higher magnetic fields in the High Field Magnetic Laboratory in Nijmegen. Figure 6.17 shows transmission spectra of $SrCo_2V_2O_8$ measured up to 30 T at 1.5 K. Below H_c the confined spinon pair excitations can be seen below 1.3 THz (40 cm^{-1}), consistent with the results in Fig. 6.16. At higher frequency, a very strong mode appears at 2.2 THz (65 $cm^{-1} \cong 8$ meV). This mode is also observed by neutron scattering

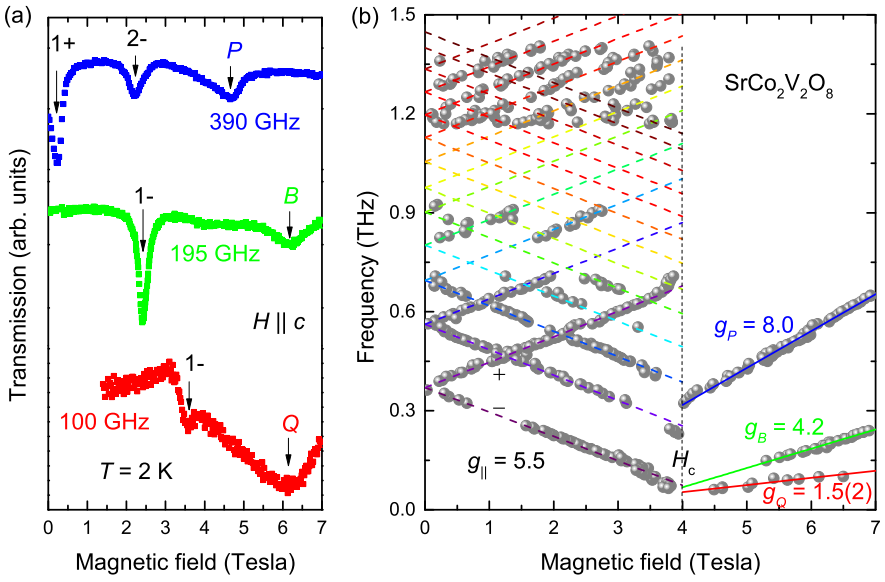

Figure 6.16: (a) Transmission spectra of various frequencies as a function of the longitudinal magnetic field i.e. $H \parallel c$, up to 7 T at 2 K. (b) Frequencies of magnetic excitations versus the magnetic field. Field dependence of spinon-pair excitation energies becomes nonlinear close to the critical field $H_c = 4$ T from below. The dashed lines are taken from Fig. 6.12(c) and extended to H_c. Three excitation modes $\boldsymbol{B}$, $\boldsymbol{P}$, and $\boldsymbol{Q}$ are observed above H_c. Their energies increase linearly with the magnetic field, which can be fitted by Zeeman terms with g factors 1.5(2), 4.2, and 8.0, respectively.

experiments. The nature of this mode is not clear. Since it disappears above H_c, it can be tentatively assigned to a kinetic bound states of spinons, which have been observed in other Ising-like spin chain systems, such as ferromagnetic $CoNb_2O_6$ [24] and antiferromagnetic $BaCo_2V_2O_8$ [36]. At 2.5, 3, 3.5, and 4.5 THz, there are several strong absorption lines, almost independent on magnetic field, that correspond to phonons.

Above H_c, the lower-lying modes $\boldsymbol{B}$, $\boldsymbol{P}$, and $\boldsymbol{Q}$ (in Fig. 6.16) are observed in higher magnetic fields in Fig. 6.17. The frequencies of modes $\boldsymbol{B}$ and $\boldsymbol{P}$ increase linearly with increasing magnetic field below H^*. Approaching H^* from below, the slopes of the curves increase and a stronger field dependence appears above H^*. Similar field dependence for modes $\boldsymbol{B}$ and $\boldsymbol{P}$ was reported in $BaCo_2V_2O_8$.[56] However, the mode $\boldsymbol{B}$ was not observed in the field range between H^* and H_s for $BaCo_2V_2O_8$ in Ref. [56]. The abrupt change of slope at H^* can be associated to the change of magnetization

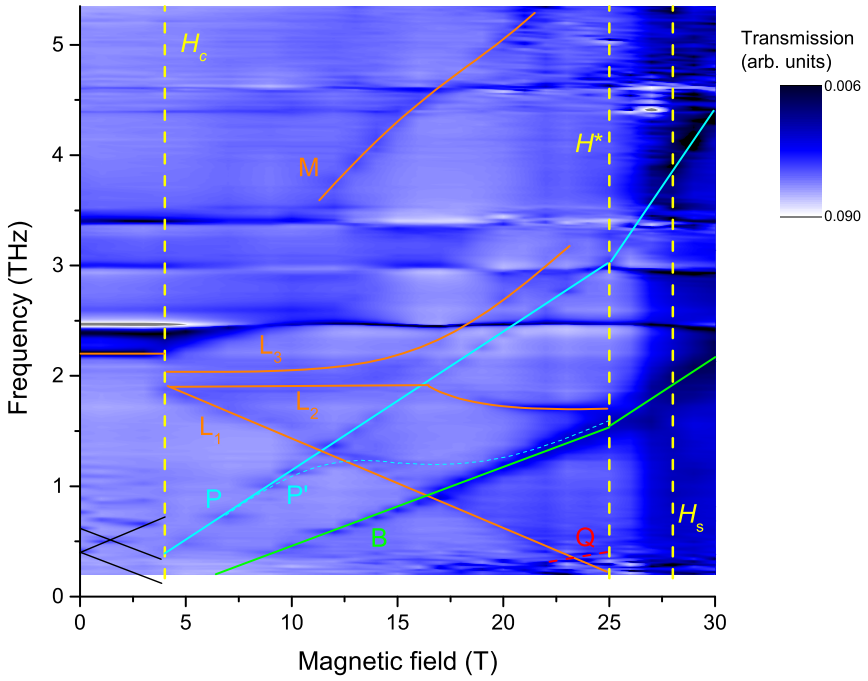

Figure 6.17: High field transmission spectra of $SrCo_2V_2O_8$ measured up to 30 T at 1.5 K. The lines are guide for eyes. The measurements were performed in the High Field Magnetic Laboratory in Nijmegen.

at H^*. This may stem from the fact that, for the Tomonaga-Luttinger spin liquid, gapless excitations are induced by a longitudinal magnetic field at an incommensurate wave vector $2k_F = \pi(1-2m)$ that is linear to the magnetization m.[56] Following this relation, one could expect a gapless mode at the Γ point when half of the saturated magnetization ($m = 1/2$) is reached. This mode is observed and named $\boldsymbol{L}_1$ in Fig. 6.17, which is gapless at H^*.

Additional modes $\boldsymbol{L}_2$, $\boldsymbol{L}_3$, $\boldsymbol{M}$, and $\boldsymbol{P'}$ are tentatively marked in Fig. 6.17. The frequency of mode $\boldsymbol{M}$ increases strongly with increasing magnetic field. It can be followed only above the phonon bands. The mode $\boldsymbol{L}_2$ shows a weak field dependence, while mode $\boldsymbol{L}_3$ is very weak due to the strong phonon absorption. The mode $\boldsymbol{P'}$ is a weak mode that evolves from the mode $\boldsymbol{P}$. These modes exhibit nonlinear field dependencies, which has not been reported in related systems. Theoretical investigations are required to fully understand these complex excitation features.

6.5 Summary

Investigations on antiferromagnetic spin chain systems $SrNi_2V_2O_8$ with $S = 1$ and $SrCo_2V_2O_8$ with $\tilde{S} = 1$ are presented in this chapter. (i) Multi-frequency electron spin resonance transmission spectra have been measured as a function of temperature in the Haldane phase of $SrNi_2V_2O_8$ with the external magnetic field parallel and perpendicular to the spin-chain direction. Above 50 K, the exchange-narrowed Ni^{2+} paramagnetic resonance lines have been observed. Between 10 and 30 K, intra-triplet resonance lines are observed for $\mathbf{H} \parallel a$ but not for $\mathbf{H} \parallel c$ in the same frequency range, indicating the existence of single-ion anisotropy. The single-ion anisotropy is estimated as -0.29 meV from the resonance modes observed for $\mathbf{H} \parallel a$. This suggests that $SrNi_2V_2O_8$ is in the disordered Haldane phase and very close to the phase boundary between the Haldane and the Ising antiferromagnetic phase. (ii) Low-energy magnetic excitations in a quasi-one-dimensional XXZ antiferromagnet $SrCo_2V_2O_8$ have been investigated with magnetic fields below and above the quantum phase transition. Below H_c, spinon-pair excitations on the antiferromagnetic ground state have been observed. Spinon-pair bound states with entangled spin-orbit moment $\tilde{S} = 1$ are determined unambiguously. The hierarchy of the spinon-pair bound-states can be described by a one-dimensional Schrödinger equation with a linear confinement potential imposed by the inter-chain interaction. Energy continuum of the elementary spinon-pair excitations is surprisingly not observed in $SrCo_2V_2O_8$. Close to H_c, the lower-lying spinon-pair excitation softens and a quantum phase transition is induced by magnetic field. Several magnetic excitations appear above H_c. Some of the excitations show clear linear dependence on the magnetization, manifesting the Tomonaga-Luttinger quantum criticality, while the nature of the nonlinear dependence of other excitations needs further theoretical investigations.

7 Conclusions and Perspectives

Quantum spin-dimer systems $CuTe_2O_5$, $Sr_3Cr_2O_8$, and $Ba_3Cr_2O_8$, and spin-chain systems $SrNi_2V_2O_8$ and $SrCo_2V_2O_8$ have been investigated by means of sub-millimeter, time-domain terahertz, and Fourier-transform infrared spectroscopy covering the spectral range from 0.2 meV to 2 eV without and with magnetic fields up to 30 T. Exotic properties from the spin, orbital, as well as lattice degrees of freedom have been found in these low-dimensional quantum magnetic systems. The main findings and conclusions are summarized as follows:

- Spin singlet-triplet excitations in the Cu-based spin-dimer system $CuTe_2O_5$ and in the Cr-based $Sr_3Cr_2O_8$ and $Ba_3Cr_2O_8$ have been observed and systematically investigated at base temperature. Since the excitations break the total spin conservation, i.e. $\Delta S \neq 1$, magnetic anisotropy plays an important role in these systems. Dzyaloshinskii-Moriya interaction as the leading antisymmetric exchange interaction can be responsible for these observations. Since the conventional Dzyaloshinskii-Moriya mechanism cannot be applied due to the constraint of inversion symmetry in the Cr dimers, a *dynamical* version with spin-phonon coupling involved has been adopted to deduce the selection rules and describe the experimental results on a phenomenological basis.

- Phononic excitations in $Sr_3Cr_2O_8$ and $Ba_3Cr_2O_8$ have been studied as a function of temperature across the Jahn-Teller structural phase transitions at T_{JT}. All phononic excitations associated to the low-symmetry phase emerge in $Ba_3Cr_2O_8$ right below the phase transition, but only when the temperature is much lower than T_{JT} in $Sr_3Cr_2O_8$. By taking into account the magnetic, phononic, and orbital excitations, the temperature-dependent specific heat has been simulated consistently. The simulations indicate that the orbital ordering is accomplished right below T_{JT} in $Ba_3Cr_2O_8$, while strong fluctuations persist in a broad temperature range below T_{JT} in $Sr_3Cr_2O_8$ which can be attributed to the orbital degrees of freedom.

- Various exotic magnetic excitations and field-induced quantum phase transitions have been found in the quantum spin-chain systems $SrNi_2V_2O_8$ and $SrCo_2V_2O_8$. At zero field, intra-triplet excitations in spin-1 antiferromagnetic chain system $SrNi_2V_2O_8$ reveal an easy-axis single-ion anisotropy and confirm its Haldane-type ground state. A quantum phase transition to an Ising antiferromagnetic

phase is induced by a transverse magnetic field. Both gapped and gapless modes emerge at the quantum phase transition. Confined spinon-pair excitations in the pseudospin-1/2 antiferromagnetic chain system $SrCo_2V_2O_8$ have been observed at zero field, where the inter-chain couplings stabilize long-range Néel order and play the role of a confinement potential. A quantum phase transition to a spin-liquid phase is induced by closing the spinon-pair excitation gap with external magnetic fields. The spin-liquid phase is characterized by various exotic magnetic excitations.

Despite the ample interesting observations and findings, more challenging questions await further investigations. For the spin-dimer systems: Since the spin-lattice coupling is crucial in the spin-dimer systems, it seems possible to enhance or manipulate spin excitations via phonons. What makes the difference of the observed orbital properties between $Ba_3Cr_2O_8$ and $Sr_3Cr_2O_8$, given that vibronic, spin-orbit, and spin-lattice couplings are present in both systems? For the spin-chain systems: Are there other one-dimensional systems to realize the spinon confinement? Is it possible to distinguish or classify the confined spinon excitations? Although the magnetic excitations can be well described at low fields in $SrNi_2V_2O_8$ and $SrCo_2V_2O_8$, it is unclear if these models can also be applied to explain the emergent excitations for fields beyond the quantum phase transitions. Both experimental and theoretical efforts are needed to answer these questions in the future.

Bibliography

[1] *International tables for crystallography: Volumn A space group symmetry, edited by Theo Hahn*, Kluwer Academic Publishers, Dordrecht (1989)

[2] A. Abragam and B. Bleaney, *Electron Paramagnetic Resonance of Transition Ions*, Clarendon, Oxford (1970)

[3] A. Abragam and M. H. L. Pryce, *Proc. Roy. Soc. (London)* **A206** 173 (1951)

[4] A. A. Aczel, H. A. Dabkowska, P. R. Provencher, and G. M. Luke, *J. Cryst. Growth* **310** 870 (2008)

[5] A. A. Aczel, Y. Kohama, M. Jaime, K. Ninios, H. B. Chan, *et al.*, *Phys. Rev. B* **79** 100409 (2009)

[6] A. A. Aczel, Y. Kohama, C. Marcenat, F. Weickert, M. Jaime, *et al.*, *Phys. Rev. Lett.* **103** 207203 (2009)

[7] N. W. Ashcroft and N. D. Mermin, *Solid State Physics, International edition*, Saunders College, Philadelphia (1976)

[8] A. K. Bera, B. Lake, A. T. M. N. Islam, B. Klemke, E. Faulhaber, *et al.*, *Phys. Rev. B* **87** 224423 (2013)

[9] A. K. Bera, B. Lake, W.-D. Stein, and S. Zander, *Phys. Rev. B* **89** 094402 (2014)

[10] A. K. Bera, D. L. Quintero-Castro, B. Lake, and et al., *unpublished*

[11] A. K. Bera and S. M. Yusuf, *Phys. Rev. B* **86** 024408 (2012)

[12] I. B. Bersuker, *The Jahn-Teller Effect and Vibronic Interactions in Modern Chemistry*, Plenum Press, New York (1984)

[13] I. B. Bersuker, *The Jahn-Teller Effect*, Cambridge University Press, Cambridge (2006)

[14] B. Bleaney and K. D. Bowers, *Proc. Roy. Soc. A (London)* **214** 451 (1952)

[15] N. M. Bogoliubov, A. G. Izergin, and V. E. Korepin, *Nucl. Phys. B* **275** 687 (1986)

[16] J. C. Bonner and M. E. Fisher, *Phys. Rev.* **135** A640 (1964)

[17] R. Botet and R. Jullien, *Phys. Rev. B* **27** 613 (1983)

[18] A. H. Bougourzi, M. Karbach, and G. Müller, *Phys. Rev. B* **57** 11429 (1998)

[19] G. Bouzerar, O. Legeza, and T. Ziman, *Phys. Rev. B* **60** 15278 (1999)

[20] M. Braden, G. Wilkendorf, J. Lorenzana, M. Aïn, G. J. McIntyre, *et al.*, *Phys. Rev. B* **54** 1105 (1996)

[21] O. Cépas, K. Kakurai, L. P. Regnault, T. Ziman, J. P. Boucher, *et al.*, *Phys. Rev. Lett.* **87** 167205 (2001)

[22] O. Cépas and T. Ziman, *Phys. Rev. B* **70** 024404 (2004)

[23] L. C. Chapon, C. Stock, P. G. Radaelli, and C. Martin, *Orbital ordering promotes weakly-interacting S=1/2 dimers in the triangular lattice compound Sr3Cr2O8*, *arXiv:0807.0877v2* (2008)

[24] R. Coldea, D. A. Tennant, E. M. Wheeler, E.Wawrzynska, D. Prabhakaran, *et al.*, *Science* **327** 177 (2010)

[25] E. Cuno and H. Müller-Buschbaum, *Z. Anorg. Allg. Chem.* **572** 95 (1989)

[26] H. Das, T. Saha-Dasgupta, C. Gros, and R. Valentí, *Phys. Rev. B* **77** 224437 (2008)

[27] J. Deisenhofer, R. M. Eremina, A. Pimenov, T. Gavrilova, H. Berger, *et al.*, *Phys. Rev. B* **74** 174421 (2006)

[28] T. Dodds, B.-J. Yang, and Y. B. Kim, *Phys. Rev. B* **81** 054412 (2010)

[29] I. Dzyaloshinskii, *J. Phys. Chem. Solids* **4** 241 (1958)

[30] R. J. Elliott and R. Loudon, *Phys. Lett.* **3** 189 (1963)

[31] R. J. Elliott and M. F. Thorpe, *J. Phys. C* **2** 1630 (1969)

[32] A. M. Farutin and V. I. Marchenko, *Journal of Experimental and Theoretical Physics* **104** 751 (2007)

[33] T. Giamarchi, C. Rüegg, and O. Tchernyshyov, *Nature Physics* **4** 198 (2008)

[34] O. Golinelli, T. Jolicœur, and R. Lacaze, *J. Phys.: Condens. Matter* **5** 7847 (1993)

[35] M. Greiter, *Nature Physics* **6** 5 (2010)

[36] B. Grenier, S. Petit, V. Simonet, L.-P. Regnault, E. Canévet, *et al.*, *arXiv:1407.0213v1* (2014)

[37] M. Grüninger, J. Münzel, A. Gaymann, A. Zibold, H. P. Geserich, *et al.*, *Europhys. Lett.* **35** 55 (1996)

[38] Z.-C. Gu and X.-G. Wen, *Phys. Rev. B* **80** 155131 (2009)

[39] F. D. M. Haldane, *Phys. Rev. Lett.* **45** 1358 (1980)

[40] F. D. M. Haldane, *Phys. Lett.* **93A** 464 (1983)

[41] F. D. M. Haldane, *Phys. Rev. Lett.* **50** 1153 (1983)

[42] S. B. Haley and P. Erdös, *Phys. Rev. B* **5** 1106 (1972)

[43] K. Hanke, V. Kupcik, and O. Lindqvist, *Acta Crystallogr., Sect. B* **29** 963 (1973)

[44] Z. He, T. Taniyama, T. Kyômen, and M. Itoh, *Phys. Rev. B* **72** 172403 (2005)

[45] Z. He and Y. Ueda, *J. Phys. Soc. Jpn.* **77** 013703 (2008)

[46] N. Ishimura and H. Shiba, *Prog. Theor. Phys.* **63** 743 (1980)

[47] A. T. M. N. Islam, D. Quintero-Castro, B. Lake, K. Siemensmeyer, K. Kiefer, *et al.*, *Crystal Growth & Design* **10** 465 (2010)

[48] G. Jackeli and D. A. Ivanov, *Phys. Rev. B* **76** 132407 (2007)

[49] J. D. Jackson, *Classical electrodynamics, 3ed.*, JOHN WILEY & SONS. INC., United States of America (1999)

[50] D. C. Johnston, *Handbook of Magnetic Materials, Vol. 10, edited by K. H. J. Buschow*, Elsevier Science, Netherlands (1997)

[51] D. Kamenskyi, J. Wosnitza, J. Krzystek, A. A. Aczel, H. A. Dabkowska, *et al.*, *J Low Temp. Phys.* **170** 231 (2013)

[52] Y. Kawasaki, J. L. Gavilano, L. Keller, J. Schefer, N. B. Christensen, *et al.*, *Phys. Rev. B* **83** 064421 (2011)

[53] G. Khaliullin, *Prog. Theor. Phys. Suppl.* **160** 155 (2005)

[54] G. Khaliullin and S. Maekawa, *Phys. Rev. Lett.* **85** 3950 (2000)

[55] S. Kimura, T. Takeuchi, K. Okunishi, M. Hagiwara, Z. He, *et al.*, *Phys. Rev. Lett.* **100** 057202 (2008)

[56] S. Kimura, H. Yashiro, K. Okunishi, M. Hagiwara, Z. He, *et al.*, *Phys. Rev. Lett.* **99** 087602 (2007)

[57] M. Kofu, J.-H. Kim, S. Ji, S.-H. Lee, H. Ueda, *et al.*, *Phys. Rev. Lett.* **102** 037206 (2009)

[58] M. Kofu, H. Ueda, H. Nojiri, Y. Oshima, T. Zenmoto, *et al.*, *Phys. Rev. Lett.* **102** 177204 (2009)

[59] E. Kroumova, M. I. Aroyo, J. M. Perez-Mato, A. Kirov, C. Capillas, *et al.*, *Phase Transitions* **76** 155 (2003)

[60] F. Krüger, S. Kumar, J. Zaanen, and J. van den Brink, *Phys. Rev. B* **79** 054504 (2009)

[61] K. I. Kugel and D. I. Khomskii, *Sov. Phys. Usp.* **25** 231 (1982)

[62] A. B. Kuz'menko, E. A. Tishchenko, and V. G. Orlov, *J. Phys.: Condens. Matter* **8** 6199 (1996)

[63] B. Lake, A. M. Tsvelik, S. Notbohm, D. A. Tennant, T. G. Perring, *et al.*, *Nature Physics* **6** 50 (2010)

[64] P. Lemmens, G. Guntherodt, and C. Gros, *Phys. Rep.* **375** 1 (2003)

[65] B. Leuenberger, A. Stebler, H. U. Güdel, A. Furrer, R. Feile, *et al.*, *Phys. Rev. B* **30** 6300 (1984)

[66] M. E. Lines, *Phys. Rev.* **131** 546 (1963)

[67] M. Matsumoto, T. Shoji, and M. Koga, *J. Phys. Soc. Jpn.* **77** 074712 (2008)

[68] B. M. McCoy and T. T. Wu, *Phys. Rev. D* **18** 1259 (1978)

[69] T. Moriya, *Phys. Rev.* **120** 91 (1960)

[70] C. M. Morris, R. V. Aguilar, A. Ghosh, S. M. Koohpayeh, J. Krizan, *et al.*, *Phys. Rev. Lett.* **112** 137403 (2014)

[71] T. Muta, *Foundations of Quantum Chromodynamics*, World Scientific Publishing, Singapore (1987)

[72] M. P. Nightingale and H. W. J. Blöte, *Phys. Rev. B* **33** 659 (1986)

[73] T. Nikuni, M. Oshikawa, A. Oosawa, and H. Tanaka, *Phys. Rev. Lett.* **84** 5868 (2000)

[74] B. Pahari, K. Ghoshray, R. Sarkar, B. Bandyopadhyay, and A. Ghoshray, *Phys. Rev. B* **73** 012407 (2006)

[75] J. B. Parkinson and J. C. Bonner, *Phys. Rev. B* **32** 4703 (1985)

[76] D. L. Quintero-Castro, B. Lake, E. M. Wheeler, A. T. M. N. Islam, T. Guidi, *et al.*, *Phys. Rev. B* **81** 014415 (2010)

[77] Y. Rahnavard and W. Brenig, *arXiv:1412.0208v2* (2014)

[78] T. Room, D. Hüvonen, U. Nagel, Y.-J. Wang, T. Timusk, *et al.*, *Phys. Rev. B* **70** 144417 (2004)

[79] S. Sachdev, *Quantum Phase Transitions*, Cambridge University Press (1999)

[80] E. Saitoh, S. Okamoto, K. T. Takahashi, K. Tobe, K. Yamamoto, *et al.*, *Nature* **410** 180 (2001)

[81] T. Sakai, O. Cépas, and T. Ziman, *J. Phys. Soc. Jpn.* **11** 3521 (2000)

[82] T. Sakai and M. Takahashi, *Phys. Rev. B* **42** 4537 (1990)

[83] Y. Sasago, K. Uchinokura, A. Zheludev, and G. Shirane, *Phys. Rev. B* **55** 8357 (1997)

[84] D. J. Scalapino, Y. Imry, and P. Pincus, *Phys. Rev. B* **11** 2042 (1975)

[85] Y. R. Shen and N. Bloembergen, *Phys. Rev.* **143** 372 (1966)

[86] H. Shiba, *Prog. Theor. Phys.* **64** 466 (1980)

[87] Y. Singh and D. C. Johnston, *Phys. Rev. B* **76** 012407 (2007)

[88] A. I. Smirnov, V. N. Glazkov, T. Kashiwagi, S. Kimura, M. Hagiwara, *et al.*, *Phys. Rev. B* **77** 100401(R) (2008)

[89] A. I. Smirnov, V. N. Glazkov, H.-A. K. von Nidda, A. Loidl, L. N. Demianets, *et al.*, *Phys. Rev. B* **65** 174422 (2002)

[90] S. Suh, K. A. Al-Hassanieh, E. C. Samulon, I. R. Fisher, S. E. Brown, *et al.*, *Phys. Rev. B* **84** 054413 (2013)

[91] Y. Tokura and N. Nagaosa, *Science* **288** 462 (2000)

[92] Y. Uchiyama, Y. Sasago, I. Tsukada, K. Uchinokura, A. Zheludev, *et al.*, *Phys. Rev. Lett.* **83** 632 (1999)

[93] A. Ushakov and S. Streltsov, *J. Phys.: Condens. Matter* **21** 305501 (2009)

[94] Z. Wang, D. Kamenskyi, O. Cépas, M. Schmidt, D. L. Quintero-Castro, *et al.*, *Phys. Rev. B* **89** 174406 (2014)

[95] Z. Wang, M. Schmidt, A. K. Bera, A. T. M. N. Islam, B. Lake, *et al.*, *Phys. Rev. B* **87** 104405 (2013)

[96] Z. Wang, M. Schmidt, A. K. Bera, B. Lake, A. Loidl, *et al.*, *submitted* (2015)

[97] Z. Wang, M. Schmidt, Y. Goncharov, Y. Skourski, J. Wosnitza, *et al.*, *J. Phys. Soc. Jpn.* **80** 124707 (2011)

[98] Z. Wang, M. Schmidt, A. Günther, F. Mayr, Y. Wan, *et al.*, *Phys. Rev. B* **85** 224304 (2012)

[99] Z. Wang, M. Schmidt, A. Günther, S. Schaile, N. Pascher, *et al.*, *Phys. Rev. B* **83** 201102 (2011)

[100] S. R. White and I. Affleck, *Phys. Rev. B* **77** 134437 (2008)

[101] K. Wierschem and P. Sengupta, *Phys. Rev. Lett.* **112** 247203 (2014)

[102] D. Wulferding, P. Lemmens, K.-Y. Choi, V. Gnezdilov, Y. G. Pashkevich, *et al.*, *Phys. Rev. B* **84** 064419 (2011)

[103] V. Zapf, M. Jaime, and C. D. Batista, *Review of Modern Physics* **86** 563 (2014)

[104] A. Zheludev, T. Masuda, I. Tsukada, Y. Uchiyama, K. Uchinokura, *et al.*, *Phys. Rev. B* **62** 8921 (2000)

Publications during doctoral study

- *Spinon confinement in the one-dimensional Ising-like antiferromagnet $SrCo_2V_2O_8$*

  Zhe Wang, M. Schmidt, A. K. Bera, B. Lake, A. Loidl, and J. Deisenhofer,
  Phys. Rev. B (Rapid Communications) **91**, 140404 (2015).

- *Spin-orbiton and quantum criticality in $FeSc_2S_4$*

  L. Mittelstädt, M. Schmidt, Zhe Wang, F. Mayr, V. Tsurkan, P. Lunkenheimer, D. Ish, L. Balents, J. Deisenhofer, and A. Loidl,
  Phys. Rev. B **91**, 125112 (2015).

- *High-field electron spin resonance spectroscopy of singlet-triplet transitions in the spin-dimer systems $Sr_3Cr_2O_8$ and $Ba_3Cr_2O_8$*

  Zhe Wang, D. Kamenskyi, O. Cépas, M. Schmidt, D. L. Quintero-Castro, A. T. M. N. Islam, B. Lake, A. A. Aczel, H. A. Dabkowska, A. B. Dabkowski, G. M. Luke, Yuan Wan, A. Loidl, M. Ozerov, J. Wosnitza, S. A. Zvyagin, and J. Deisenhofer,
  Phys. Rev. B **89**, 174406 (2014).

- *Orbital-selective metalinsulator transition and gap formation above TC in superconducting $Rb_{1-x}Fe_{2-y}Se_2$*

  Zhe Wang, M. Schmidt, J. Fischer, V. Tsurkan, M. Greger, D. Vollhardt, A. Loidl, and J. Deisenhofer,
  Nature Communications **5**, 3202 (2014).

- *Exciton-magnon transitions in the frustrated chromium antiferromagnets $CuCrO_2$, α-$CaCr_2O_4$, $CdCr_2O_4$, and $ZnCr_2O_4$*

  M. Schmidt, Zhe Wang, Ch. Kant, F. Mayr, S. Tóth, A. T. M. N. Islam, B. Lake, V. Tsurkan, A. Loidl, and J. Deisenhofer,
  Phys. Rev. B **87**, 224424 (2013).

- *Low-energy magnetic excitations in the quasi-one-dimensional spin-1 chain compound $SrNi_2V_2O_8$*

  Zhe Wang, M. Schmidt, A. K. Bera, A. T. M. N. Islam, B. Lake, A. Loidl, and J. Deisenhofer,
  Phys. Rev. B **87**, 104405 (2013).

- *Electron spin resonance and exchange paths in the orthorhombic dimer system Sr_2VO_4*

  J. Deisenhofer, S. Schaile, J. Teyssier, Zhe Wang, M. Hemmida, H.-A. Krug von Nidda, R. M. Eremina, M. V. Eremin, R. Viennois, E. Giannini, D. van der Marel, and A. Loidl,
  Phys Rev. B **86**, 214417 (2012).

- *Terahertz spectroscopy in the pseudo-Kagome system $Cu_3Bi(SeO_3)_2O_2Br$*

  Zhe Wang, M. Schmidt, Y. Goncharov, H.-A. Krug von Nidda, V. Tsurkan, A. Loidl, and J. Deisenhofer,
  Phys. Rev. B **86**, 174411 (2012).

- *Weak localization in few-layer graphene grown on copper foils by chemical vapor deposition*

  Wenrong Wang, Liang Chen, Zhe Wang, Yuchen Wang, Tie Li, and Yuelin Wang, Carbon **50**, 5242 (2012).

- *Infrared phonons and specific heat in the gapped quantum magnet $Ba_3Cr_2O_8$*

  Zhe Wang, M. Schmidt, A. Günther, F. Mayr, Yuan Wan, S.-H. Lee, H. Ueda, Y. Ueda, A. Loidl, and J. Deisenhofer,
  Phys. Rev. B **85**, 224304 (2012).

- *Universal exchange-driven phonon splitting in antiferromagnets*

  Ch. Kant, M. Schmidt, Zhe Wang, F. Mayr, V. Tsurkan, J. Deisenhofer, and A. Loid,
  Phys. Rev. Lett. **108**, 177203 (2012).

- *Optical conductivity of superconducting $Rb_2Fe_4Se_5$ single crystals*

  A. Charnukha, J. Deisenhofer, D. Pröpper, M. Schmidt, Zhe Wang, Y. Goncharov, A. N. Yaresko, V. Tsurkan, B. Keimer, A. Loidl, A. V. Boris,
  Phys. Rev. B (Rapid Communications) **85**, 100504 (2012).

- *Magnetization and specific heat of the dimer system $CuTe_2O_5$*

  R. M. Eremina, T. P. Gavrilova, A. Günther, Zhe Wang, M. Johnsson, H. Berger, H.-A. Krug von Nidda, J. Deisenhofer, and A. Loidl,
  Eur. Phys. J. B **84**, 391 (2011).

- *Singlet-triplet excitations and high-field magnetization in $CuTe_2O_5$*

  Zhe Wang, M. Schmidt, Y. Goncharov, Y. Skourski, J. Wosnitza, H. Berger, H.-A. Krug von Nidda, A. Loidl, J. Deisenhofer,
  J. Phys. Soc. Jpn. **80**, 124707 (2011).

- *Lattice vibrations in $KCuF_3$*

  J. Deisenhofer, M. Schmidt, Zhe Wang, Ch. Kant, F. Mayr, F. Schrettle, H.-A. Krug von Nidda, P. Ghigna, V. Tsurkan, and A. Loidl,
  Annalen der Physik **523**, 645 (2011).

- *Orbital fluctuations and orbital order below the Jahn-Teller transition in $Sr_3Cr_2O_8$*

  Zhe Wang, M. Schmidt, A. Günther, S. Schaile, N. Pascher, F. Mayr, Y. Goncharov, D. L. Quintero-Castro, A. T. M. N. Islam, B. Lake, H.-A. Krug von Nidda, A. Loidl, and J. Deisenhofer,
  Phys. Rev. B (Rapid Communications) **83**, 201102 (2011).

Acknowledgements

This thesis cannot be accomplished without the helps from many people. I would like to thank Professor Alois Loidl for providing me the precious opportunity to perform my doctoral study in EP5. He created and maintained an ideal environment for performing research. I appreciate Joachim Deisenhofer very much for his guidance to research. He taught me a lot and always with great patience. We were very often sitting together to discuss a problem or a manuscript or to rehearse my talk. Those moments were beautiful and unforgettable.

Michael Schmidt never hesitated to help me whenever I interrupted him. As both doctoral students in the optics group, we performed most of the experiments together and shared both those easy and hard time in lab. As senior scientists on optical spectroscopy, Franz Mayr and Yurri Goncharov shared with me many helpful and important lab experiences. I am indebted to their helps.

I benefit a lot from my collaborators. Most of the single crystals that I investigated and presented in this thesis came from Bella Lake and her group members Anup Kumar Bera, Diana Lucía Quintero-Castro, and Nazmul Islam. I also received high quality samples from Adam Aczel, Helmuth Berger, Antoni Dabkowski, Hanna Dabkowska, Seunghun Lee, Graeme Luke, Yutaka Ueda, Hiroaki Ueda. I am very grateful for their generosity.

I would like to thank Hans Engelkamp, Papori Gogoi, Dmytro Kamenski, István Kézsmárki, Dávid Szaller, Joachim Wosnitza, Shadi Yasin, Sergei Zvyagin, and Sergei Zherlitsyn for their host, collaborations and helps on doing high field measurements.

I am also indebted to the theoreticians Olivier Cépas and Yuan Wan. Discussion with them always brought me a clear physical picture.

I would also thank my internal collaborators Jonas Fischer, Axel Günther, Christian Kant, Hans-Albrecht Krug von Nidda, Lisa Mittelstädt, Sebastian Schaile, Vladimir Tsurkan, and all the other EP5 members. The comfortable and friendly atmosphere makes EP5 a wonderful place for doctoral study.

Finally, I would like to thank Si for her understanding and constant supports.